Planar Antennas and Lenses for Terahertz Source Integration

by

Mingxiang Li

B Eng (Electrical and Electronic Engineering, 1st class Honours),
The University of Adelaide, Australia, 2019

Thesis submitted for the degree of

Doctor of Philosophy

in

School of Electrical and Mechanical Engineering
Faculty of Sciences, Engineering and Technology
The University of Adelaide

2024

Supervisors:

Prof. Withawat Withayachumnankul,

School of Electrical and Mechanical Engineering, The University of Adelaide

Prof. Christophe Fumeaux,

School of Electrical Engineering and Computer Science, The University of Queensland

© 2024
Mingxiang Li
All Rights Reserved

Contents

Contents iii

Abstract vii

Originality Declaration ix

Acknowledgments xi

Publications xiii

List of Figures xv

List of Tables xix

Chapter 1. Introduction 1

1.1 Terahertz technology and applications 3

1.1.1 Terahertz communications 3

1.1.2 Terahertz imaging 5

1.2 Advanced terahertz sources 6

1.2.1 Electronic terahertz generation 7

1.2.2 Photonic terahertz generation 11

1.3 Planar terahertz antennas and lenses 14

1.3.1 Antennas 16

1.3.2 Lens 20

1.4 Thesis outline and original contributions 24

Chapter 2. Terahertz resonant-tunneling diode with series-fed patch array antenna 29

2.1 Introduction 31

2.2 Design and analysis 32

2.2.1 RTD characteristics . . . 32
2.2.2 Series-fed patch array design . . . 36
2.3 Bullet lens validation . . . 39
2.4 Fabrication and measurement . . . 43
2.5 Conclusion . . . 48

Chapter 3. Terahertz resonant-tunneling diode with log-spiral antenna 51
3.1 Introduction . . . 53
3.2 Design and analysis . . . 54
3.3 Simulation results . . . 55
3.4 Conclusion . . . 59

Chapter 4. Terahertz metasurface for near-field beam conversion 61
4.1 Introduction . . . 63
4.2 Design and analysis . . . 64
4.2.1 Unit cell . . . 64
4.2.2 Metasurface lens . . . 66
4.3 Fabrication and measurement . . . 69
4.4 Conclusion . . . 71

Chapter 5. Planar high-gain antenna for terahertz communications 73
5.1 Introduction . . . 75
5.2 Antenna Design and analysis . . . 77
5.2.1 Effective medium for GRIN . . . 77
5.2.2 Cavity antenna design based on effective medium . . . 78
5.3 Fabrication and measurement . . . 84
5.4 Wireless communications demonstrations . . . 90
5.5 Conclusion . . . 91

Chapter 6. Terahertz frequency-diverse antenna for direction of arrival estimation 95
6.1 Introduction . . . 97
6.2 Operation principle . . . 99

6.2.1 Antenna design 99
6.2.2 ML-based analysis 104
6.3 Antenna fabrication and measurement setup 108
6.4 DoA prediction with ML 112
6.5 Conclusion 115

Chapter 7. Summary and Outlook **117**
7.1 Thesis conclusion 119
7.2 Outlook 119

Bibliography **123**

Abstract

The terahertz frequency band shows promise in various applications, yet the limited output power from terahertz sources has hindered the development of practical terahertz applications. Therefore, to preserve the precious terahertz power, the design of efficient antennas and lenses becomes crucial. Traditional antennas and lenses are often bulky, lossy, and expensive. Hence, there is an urgent need to explore planar solutions for highly efficient antennas and lenses tailored specifically to the terahertz range. These solutions should be cost-effective, capable of significantly reducing the device profile, supporting various beam shapes, and minimizing additional losses. Furthermore, these solutions should have the ability to integrate with sources for system compactness. To this end, this thesis focuses on innovative approaches to design terahertz planar antennas and lenses with integrated sources.

In a first approach derived from microwave technologies, planar metallic antennas are integrated with a terahertz resonant-tunneling diode, with extended bias lines allowing the propagation of surface waves. Instead of eliminating these surface waves, which might lead to energy waste and compromised efficiency, planar metallic antennas are employed to effectively control the propagating surface wave, resulting in distinct radiation characteristics. Two types of planar metallic antennas are explored: one approach involves a series-fed patch array antenna designed to enhance radiation performance, while the other approach utilizes a log-spiral antenna for circularly-polarized radiation.

In a second approach derived from optical technologies, planar lenses can be realized through various phase control techniques, resulting in specific output phase distributions for different applications. For a metasurface, modifying the geometry of a unit cell allows control of the phase response. Metasurface lenses can achieve various types of beams based on the designed phase profiles. As an alternative, adjusting the density of air holes etched into a silicon substrate controls the effective refractive index, and therefore controls the phase response. Effective medium lens can achieve a uniform output phase distribution for high-gain performance. Likewise, adjusting the height of 3-D printed dielectric pillars controls the phase response. A 3-D printed lens with random pillar heights can achieve a random output phase distribution and uncorrelated

radiation patterns across the frequency range. As a non-planar design, this type of lens offers distinct radiation patterns that can be utilized for direction-of-arrival estimation.

The antennas and lenses proposed in this doctoral thesis offer cost-effective, highly efficient, low-profile, and source-integrable solutions, which are expected to support practical terahertz applications in sensing and communications.

Originality Declaration

I certify that this work contains no material which has been accepted for the award of any other degree or diploma in my name, in any university or other tertiary institution and, to the best of my knowledge and belief, contains no material previously published or written by another person, except where due reference has been made in the text. In addition, I certify that no part of this work will, in the future, be used in a submission in my name, for any other degree or diploma in any university or other tertiary institution without the prior approval of the University of Adelaide and where applicable, any partner institution responsible for the joint-award of this degree.

I also give permission for the digital version of my thesis to be made available on the web, via the University's digital research repository, the Library Search and also through web search engines, unless permission has been granted by the University to restrict access for a period of time.

Mingxiang Li

Signed

2024-03-26

Date

Acknowledgments

I gratefully acknowledge all the guidance and support received from my esteemed supervisors Prof. Withawat Withayachumnankul and Prof. Christophe Fumeaux, as well as my friends, colleagues, and beloved family. It is indeed a wonderful journey.

First and foremost, I would like to express my deepest gratitude to my principal supervisor Prof. Withawat Withayachumnankul, who is an outstanding scholar and a most reliable supervisor. Prof. Withayachumnankul welcomed me as a Ph.D. candidate right after I finished the honor bachelor project back in 2019. At that time, I had very limited and insufficient knowledge on electromagnetics and terahertz engineering. With patience and guidance, he led me through every step of my research career, covering fundamental concepts, design and simulation techniques, article writing, presentation skills, and fostering higher-level critical thinking and research engagement. It was his excellent guidance, encouragement, patience, kindness, and rigorous research attitude that inspired me and set me on the right path. From time to time he shared novel ideas, relevant literature and conference, and social connections, contributing significantly to my growth as an independent researcher. Throughout my candidature, Prof. Withayachumnankul provided countless assistance and support for which no words can adequately express my appreciation.

I would also like to gratefully acknowledge the support and guidance from my co-supervisor Prof. Christophe Fumeaux. Back to my undergraduate studies, a second-year course given by Prof. Fumeaux opened the door to the world of electromagnetics, and I was glad to find that Maxwell's equations were not as intimidating as they seemed. His professional guidance afforded me a comprehensive understanding of electromagnetic and antenna theory, which benefits my whole Ph.D. candidature. As an expert in all-spectrum theory and techniques, his profound knowledge consistently transformed difficulties into understandable and solvable pieces. His rigorous attitude towards all research-related aspects is a model for everyone to follow. It is a great honour to learn from and work with Prof. Fumeaux.

My gratefulness goes to my cooperation project researchers from Tokyo Institute of Technology, Japan, including Assoc. Prof. Safumi Suzuki, Prof. Masahiro Asada, Dr. Adrian Dobroiu, Dr. Van Ta Mai, Dr. Feifan Han for their guidance and assistance on the

resonant-tunneling diode samples fabrication and relevant experiments. Their constructive and insightful comments on my research design and articles are invaluable.

My special thanks also go to Prof. Sharath Sriram and Dr. Rajour Tanyi Ako from the Functional Materials and Microsystems Research Group and the Micro Nano Research Facility at RMIT University, Melbourne. The metasurface and silicon lens prototypes with excellent performance were fabricated by them. I am also thankful to Assoc. Prof. Ke (Desmond) Wang and Dr. Jiayuan (Estrid) He from RMIT University, Melbourne, for their fruitful discussions and suggestions.

Here, I sincerely thank the past and present members from both Terahertz Engineering Laboratory and our neighbouring Applied Electromagnetics Group at the University of Adelaide, Dr. Shengjian (Jammy) Chen, Dr. Nghia Nguyen Trong, Dr. Daniel Headland, Dr. Wendy S. L. Lee, Dr. Xiaolong You, Dr. Weijie Gao, Dr. Xiaojing (Alex) Lv, Dr. Mohamed Shehata, Dr. Panisa Dechwechprasit, Dr. Morteza Shahpari, Dr. Siti Nailah Mastura Zainarry, Dr. Quoc Hung Dang, Dr. Xiaoyang Yin, Dr. Purna B. Samal, Dr. Yuan (Grace) Yuan, Mr. Harrison Lees, Mr. Bryce Chung, Ms. Linxi Chen, Mr. Sakib Quader, Ms. Mariam Abdullah, Mr. Miantong Sun, Mr. Chung Yin Tam, Mr. Tianchang (Vincent) Ma, Mr. Junyi Chen, and Mr. Patrick Joseph Bartley. Great thanks to Dr. Weijie Gao, Dr. Xiaolong You, Mr. Harrison Lees and Mr. Bryce Chung for the fruitful discussions and invaluable assistance in conducting experiments. I would also like to thank Mr. Brandon Pullen, Mr. Hayden Westell, Mr. Danny Di Giacomo, Mr. Alban O'Brien from the school workshop for their technical support and for realizing high-quality customized device.

I acknowledge the financial supports from Adelaide Graduate Centre (AGC), and Australian Research Council (ARC) including the Adelaide Graduate Research Scholarship, scholarship stipend, travelling grants and other subsidies. I am also thankful to the School of Electrical and Mechanical Engineering (previously School of Electrical and Electronic Engineering), who supported me to attend international conferences to communicate and get connected with researchers worldwide.

Finally, my endless and heartfelt appreciation goes to my dearest family, who loves me and unconditionally supports me throughout my life. Thank you for everything that you have given me, without which I will not be where I am today.

Publications

Journals

Li-M. S., Abdullah-M., He-J., Wang-K., Fumeaux-C., and Withayachumnankul-W. (2024). Frequency-diverse antenna with convolutional neural networks for direction of arrival estimation in terahertz communications, *IEEE Transactions on Terahertz Science and Technology*, Early access, doi: 110.1109/TTHZ.2024.3358735.

Li-M. S., Ako-R. T., Sriram-S., Fumeaux-C., and Withayachumnankul-W. (2024). Terahertz planar cavity antenna based on effective medium for wireless communications, *IEEE Transactions on Terahertz Science and Technology*, **14**(2), pp. 248–257.

Li-M. S., Ako-R. T., Sriram-S., Fumeaux-C., and Withayachumnankul-W. (2023). Terahertz metasurface for near-field beam conversion, *Optics Letters*, **48**(8), pp. 2202–2205. (**Editor's pick**).

Li-M. S., Mai-T. V., Fumeaux-C., Suzuki-S., and Withayachumnankul-W. (2023). Terahertz resonant-tunneling diode with series-fed patch array antenna, *IEEE Transactions on Terahertz Science and Technology*, **13**(2), pp. 178–187.

Conferences

Li-M. S., Ako-R. T., Sriram-S., Fumeaux-C., and Withayachumnankul-W. (2023). High-gain, low-profile, integrable planar lens antenna at 275 GHz, *2023 IEEE 11th Asia-Pacific Conference on Antennas and Propagation (APCAP)*, Guangzhou, China. (**Invited**).

Li-M. S., Suzuki-S., Fumeaux-C., and Withayachumnankul-W. (2023). Resonant-tunneling diode with spiral bias connections for circularly polarized radiation, *2023 48th International Conference on Infrared, Millimeter, and Terahertz Waves (IRMMW-THz)*, Montreal, Canada, pp. 1–2.

Li-M. S., Fumeaux-C., and Withayachumnankul-W. (2022). 275-GHz planar high-gain resonant cavity antenna with effective medium, *2022 International Symposium on Antennas and Propagation (ISAP)*, Sydney, Australia, pp. 121–122.

Li-M. S., Fumeaux-C., and Withayachumnankul-W. (2022). Terahertz beam shaping: Gaussian to flat-top beam conversion through tri-layer metasurface, *2022 47th International Conference on Infrared, Millimeter, and Terahertz Waves (IRMMW-THz)*, Delft, Netherlands, pp. 1–2.

Li-M. S., Suzuki-S., Fumeaux-C., and Withayachumnankul-W. (2021). Improving the radiation performance of resonant-tunneling diode by using planar metallic arrays, *2021 46th International Conference on Infrared, Millimeter, and Terahertz Waves (IRMMW-THz)*, Chengdu, China, pp.1–2. (**Keynote**).

List of Figures

1.1 Wireless communications data rate evolution 4
1.2 Terahertz high-resolution imaging applications 5
1.3 Semiconductor terahertz sources 7
1.4 Terahertz resonant-tunneling diode (RTD) 9
1.5 Harmonic-based terahertz source 11
1.6 Different types of photodiodes 13
1.7 Atmospheric attenuation at terahertz frequency 15
1.8 VDI WR-3.4 diagonal horn antennas 16
1.9 Terahertz planar antennas with patterned metallic layers 17
1.10 Terahertz leaky-wave antennas 19
1.11 Terahertz 3-D printed lenses 22
1.12 Terahertz end-fire antennas based on the silicon waveguide platform . . 23

2.1 Simplified RTD structure without the MIM capacitor 33
2.2 Schematic of RTD structure under extended bias lines condition 34
2.3 Comparison of RTD structures 35
2.4 RTD with a series-fed patch array 37
2.5 Comparison of Y-parameters simulated from the original RTD and RTD with a series-fed patch array 38
2.6 Bullet lens geometry and simulated RTD performance 40
2.7 Comparison of simulated radiation patterns in the E-plane with the bullet lens: RTD with a series-fed patch array (red) and original RTD (blue) . . 41
2.8 Simulated radiation performance at 275 GHz 42
2.9 Employed RTD structure 44
2.10 Fabricated RTD samples 44
2.11 Measurement setup 46
2.12 Measurement and simulation results. The patterns are normalized to their maximum values of the E- and H-planes 47

3.1 CP RTD structure 54
3.2 Simulated current amplitude distributions along the log-spiral antenna surface 56
3.3 Comparison of Y-parameters simulated from the original dipole antenna and RTD with a log-spiral antenna 56
3.4 Simulated radiation efficiency 57
3.5 Simulation results between 400–600 GHz 58

4.1 Tri-layer metasurface unit cell 65
4.2 Simulated performance of unit cells 66
4.3 Metasurface lens phase profile 68
4.4 Measurement setup 69
4.5 Measurement results at 275 GHz. The intensity distributions are normalized to their own maximum values 70
4.6 Measurement results over the WR-3.4 frequency band 71

5.1 Effective medium principle 77
5.2 Tapered air hole structure 79
5.3 Silicon cavity antenna based on double-sided effective medium 80
5.4 Laser-etched air hole patterns 81
5.5 Electric-field distributions from CST simulation 83
5.6 Fabricated silicon cavity antenna sample 85
5.7 Radiation measurement setup 86
5.8 Radiation measurement and simulation results 87
5.9 Near-field scanning measurement 88
5.10 Communications measurement schematic 90
5.11 Communications measurement results 92

6.1 Frequency-diverse antenna structure 100
6.2 Simulated radiation patterns 101
6.3 Uniformity and correlation of radiation patterns 102
6.4 WR-3 diagonal horn antenna performance comparison 104
6.5 Parameter analysis showing model performance with varying model parameters 107
6.6 Model architecture for the proposed CNN model 108
6.7 Fabricated antenna 109
6.8 Measurement setup 110
6.9 Measurement results 111
6.10 Training results for the final k-fold validation 113
6.11 DoA predictions of various models 114

List of Tables

2.1 Comparison on radiation performance of RTD integrated with antenna . 48

5.1 Comparison on the state-or-art integrable lens antennas 89

Chapter 1

Introduction

THE terahertz frequency range is sandwiched between millimeter-wave and infrared frequencies. The unique properties of this frequency range, including sub-millimeter resolution, large absolute bandwidth and non-ionizing penetration, allow promising applications including high-speed wireless communications, high-resolution imaging and non-destructive evaluation. However, generating power in the terahertz range remains challenging for both electronic-based and photonic-based methods, resulting in typically low output power. Therefore, the design of efficient antennas and lenses is crucial to enable effective power extraction and beamforming. A cost-effective, efficient, low-profile, and source-integrable solution is essential for developing terahertz antennas and lenses. This introduction chapter provides background knowledge on terahertz technology, advanced terahertz sources, planar antennas and lenses, together with an outline of the thesis.

1.1 Terahertz technology and applications

The terahertz frequency band fills a gap in the electromagnetic spectrum between millimeter-wave (MMW) and infrared frequencies, classically defined as covering the frequency range from 0.1–10 THz. The unique properties of this spectral band are due to its transitional range between electronics and photonics. On the one hand, compared to lower microwave frequencies, terahertz radiation offers an exceptionally wide bandwidth and high operating frequencies, which have the potential to support the revolutionary progress of high-speed wireless communications systems (Nagatsuma *et al.*, 2016) and high-resolution imaging systems (Mittleman, 2018). On the other hand, terahertz radiation can penetrate dry non-metallic objects, while lacking the photon energy required for ionization makes it particularly suitable for non-destructive evaluation (NDE) applications, such as biomedical sensing (Pickwell and Wallace, 2006) and material characterization (Naftaly and Miles, 2007). This section will focus on various terahertz applications and technologies, including communications, high-resolution imaging, and NDE applications.

1.1.1 Terahertz communications

Wireless communications systems have become part of our daily lives and are indispensable in various industries, leading to a dramatic growth in data traffic. As moving toward the year 2030, communications networks are expected to be equipped for a large number of highly demanding applications that facilitate functions such as virtual, augmented, and mixed reality as well as remote control of sensitive operations (Ericsson, 2022). The requirement on high-quality, data-intensive connections becomes a heavy burden for the frequency bands below 3 GHz that are currently used for 4G LTE, resulting in high congestion. The limited spectral resources in the microwave frequencies and the escalating demand for high data capacity, therefore, have prompted the investigation of unexplored frequency resources in higher frequency bands. As outlined by Shannon's capacity theorem, the maximum data rate achievable over a communications channel depends on its allocated bandwidth and signal quality (Shannon, 1948). The large absolute bandwidth offered by the terahertz frequency range is vital for the development of future 6G and beyond 6G (B6G) communications networks, as it has the potential to support theoretical transmission speed up to Tb/s level (Akyildiz *et al.*, 2022). As demonstrated in Fig. 1.1, the data rates achieved with various

1.1.1 Terahertz communications

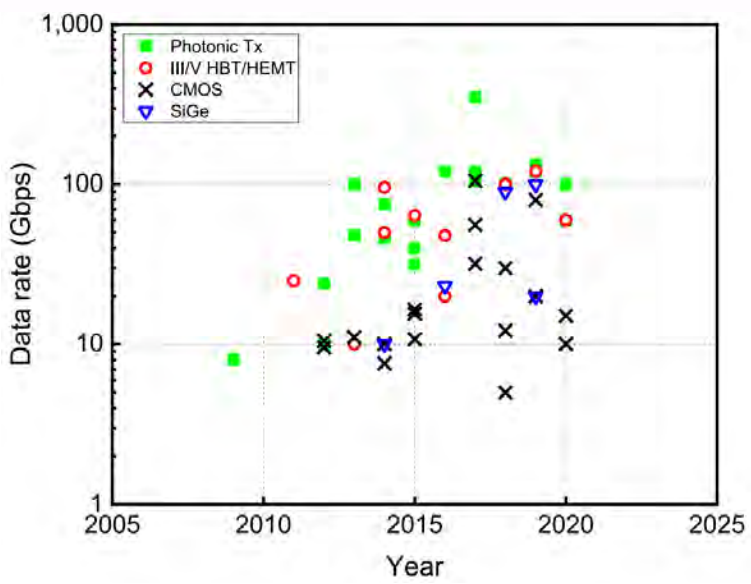

Figure 1.1. Wireless communications data rate evolution. Data rates achieved in the last two decades with different terahertz technologies. Adopted from Song and Lee (2022).

terahertz technologies are continuously increasing over the last two decades (Song and Lee, 2022). The graph showcases that data rates have surpassed 100 Gb/s, with the highest reported data rate of 352 Gb/s achieved through a single carrier frequency of 141 GHz and a 2×2 multi-input multi-output (MIMO) multiplexing (Puerta *et al.*, 2017). While considerable efforts have been paid to overcome challenges and to evolve our understanding of various aspects of terahertz communications, achieving the theoretical Tb/s level data rate remains highly challenging.

The primary challenges that hinder reaching the Tb/s level data rate include the lack of high-power solid-state terahertz sources (Makhlouf *et al.*, 2023) and the scarcity of energy-efficient transceivers (Withayachumnankul *et al.*, 2018). These challenges will be further discussed in Sections 1.2 and 1.3. Another challenge lies in modulation schemes at the terahertz range, where simple techniques such as on-off keying (OOK) and pulse amplitude modulation (PAM) typically achieve data rates below 50 Gb/s (Cimbri *et al.*, 2022b; Oshiro *et al.*, 2022). Achieving data rates exceeding 100 Gb/s requires advanced modulation schemes involving *I*-*Q* mixing for quadrature amplitude modulation (QAM) with higher-order constellations. However, terahertz QAM signals, whether photonic-based or electronic-based, often suffer from high phase noise and *I*-*Q* imbalance, which can significantly degrade the signal quality (Song and Lee, 2022; Dan *et al.*, 2020). Nevertheless, this underutilized spectrum range, together with its rapidly developing technology, has attracted the attention of the telecommunications

industry, particularly in the context of the next generation of wireless communications systems.

1.1.2 Terahertz imaging

Terahertz imaging technology has made significant strides in the past two decades, with notable progress in both fundamental research and practical applications (Jepsen *et al.*, 2011; Valušis *et al.*, 2021). Terahertz frequencies, with their shorter wavelengths and smaller diffraction limits, enable the resolution and detection of finer details. As illustrated in Fig. 1.2(a), a reflection-based terahertz beam scanning using a 3-D printed Risley prism (Chung *et al.*, 2022) was demonstrated to provide a target resolution less than 0.5 mm. Such a high resolution capacity extends to astronomy research with, for example, the submillimeter common-user bolometer array 2 (SCUBA-2) operating on the James Clerk Maxwell Telescope (JCMT), which is equipped with more than 10,000 pixel bolometer cameras operating at 450 µm and 850 µm (NIST, 2021). In Fig. 1.2(b),

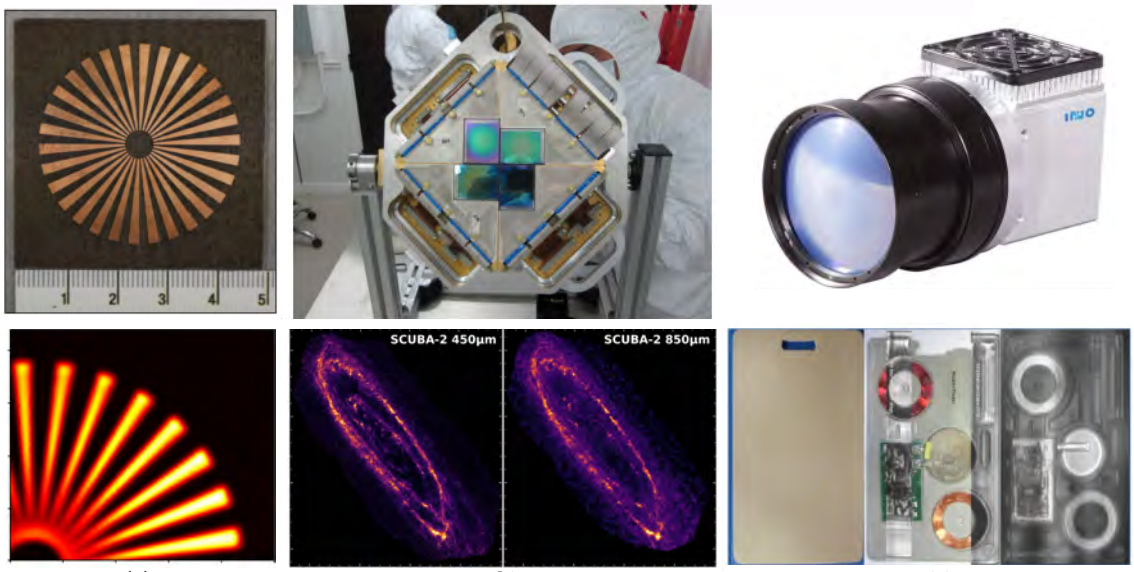

Figure 1.2. Terahertz high-resolution imaging applications. (a) Terahertz beam scanning on a resolution target through a Risley prism. Measured conducted in the Terahertz Engineering Laboratory. (b) SCUBA-2 sensor array used for high resolution terahertz Andromeda galaxy survey (HASHTAG) project. Two images of the Andromeda galaxy are taken at operating wavelengths of 450 µm (667 GHz) and 850 µm (353 GHz). Adopted from Smith *et al.* (2021). (c) INO terahertz camera. Terahertz image taken for a magnetic card, revealing the components inside the magnetic card. Adopted from INO (2022).

SCUBA-2's focal-plane units demonstrate the capabilities to image objects at the far end of the universe (Smith *et al.*, 2021). Furthermore, terahertz radiation exhibits superior penetration abilities in various packaging materials, including paper, cardboard, and plastics, making it invaluable for imaging applications. Figure 1.2(c) presents a commercial terahertz camera, the MICROXCAM-384I-THZ, featuring a 384×288 pixel uncooled micro-bolometric detector array manufactured by INO Inc., Canada (INO, 2022). The example also shown in Fig. 1.2(c) illustrates the camera's capacity to capture images of components within a magnetic card, a task impossible for regular visible light cameras.

The remarkable combination of high-resolution imaging capabilities and non-ionizing radiation properties makes terahertz radiation particularly suitable for NDE applications. One such application is in pharmaceutical quality control, where terahertz radiation aids in inspecting the quality of pharmaceutical tablets and capsules, detecting cracks and structural defects, as demonstrated in Moradikouchi *et al.* (2022). Terahertz radiation has a potential in medical-related imaging, especially in the study of biological tissues for early cancer detection and skin disease diagnosis (Yang *et al.*, 2016; Lee *et al.*, 2022). Furthermore, it proves valuable in the examination of composite materials to ensure structural integrity and identify any sub-surface defects or weaknesses. Notably, many materials exhibit unique characteristics in the terahertz frequency range, including permittivities and loss tangents distinct from their behavior in the microwave range (Balakrishnan *et al.*, 2009). The properties of such materials can be investigated through terahertz time-domain spectroscopy (THz-TDS), which measures a material's response to terahertz pulses across a broad frequency range. While the applications in biomedical research have not reached clinical trials yet, NDE applications are increasingly finding practical usage in various industries such as food production (Afsah-Hejri *et al.*, 2019), agriculture (Thigale *et al.*, 2023), and art conservation (Fukunaga *et al.*, 2007).

1.2 Advanced terahertz sources

Despite the promising applications outlined in Section 1.1, the terahertz frequency band faces the significant challenge that the power output from terahertz sources is relatively low. There are two main approaches for generating terahertz waves, namely either utilizing electronic and photonic technologies. This section provides a brief overview of terahertz sources from both electronic and photonic modalities.

Electronic generation methods draw from technology developed for microwaves and include devices like transistors oscillators (Samoska, 2011) and different types of diodes, including Gunn diodes (Khalid *et al.*, 2014), impact ionization avalanche transit-time (IMPATT) diodes (Acharyya and Banerjee, 2014), and resonant tunneling diodes (RTD) (Asada and Suzuki, 2021). Photonic generation methods, on the other hand, leverage optical technologies and use light waves, involving devices such as quantum cascade lasers (QCLs) (Jin *et al.*, 2020) and photodiodes (Seddon *et al.*, 2022). However, electronic sources tend to experience increasing parasitic effects, including ohmic loss and reactance, as frequency rises. Meanwhile, photonic sources often require temperature control and have a more complex setup. Both technologies experience a significant drop in output power when approaching the terahertz range, a phenomenon often referred to as the 'terahertz gap', as shown in Fig. 1.3.

1.2.1 Electronic terahertz generation

Electronic terahertz sources have the advantage of being compact, lightweight, and easily integrated into systems. Moreover, they can be mass-produced using scalable and cost-effective integrated circuit processes. However, there are fundamental limitations in generating terahertz frequencies electronically, primarily due to the low power levels and physical constraints related to feature sizes.

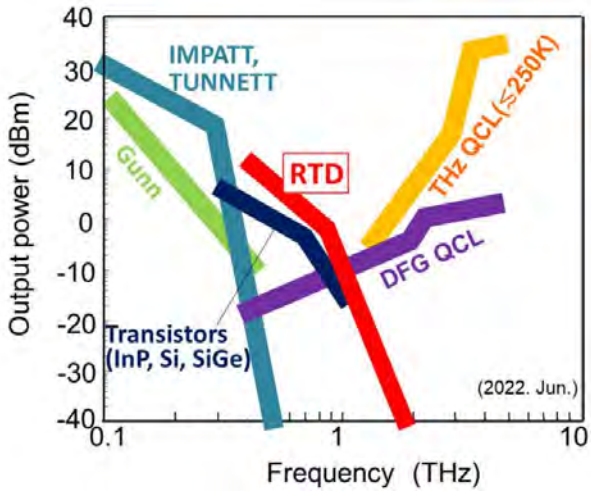

© 2022 IEEE

Figure 1.3. Semiconductor terahertz sources. Both electronic-based and photonic-based sources experience a significant power drop as they approach the terahertz range. Adopted from Suzuki (2022).

1.2.1 Electronic terahertz generation

Recently, there has been extensive research into terahertz transistors based on indium phosphide (InP), silicon, and silicon germanium (SiGe) substrates, benefiting from the mature semiconductor manufacturing and processing technologies. These transistors are predominantly field-effect transistors (FETs) that utilize a field voltage to control current flow in semiconductors. Common types of terahertz FETs include oscillator-based complementary metal-oxide-semiconductor (CMOS) FETs typically capable of operating below 700 GHz (Gao and Chan, 2023, 2024b), SiGe heterojunction bipolar transistors (HBTs) with operation frequencies exceeding 1.2 THz (Arabhavi *et al.*, 2022), and high electron mobility transistors (HEMTs) that have achieved operation frequencies around 1.5 THz (Mei *et al.*, 2015). It is worth mentioning that these transistors are oscillator-based, as multiplier-chain based types have a significantly reduced output power (Aghasi *et al.*, 2017). Achieving these terahertz operation frequencies has involved significant size reduction of these transistors. For even higher operation frequencies, these transistors often feature gate lengths smaller than 20 nm, while the substrate thickness is reduced to just 20 µm to mitigate signal attenuation and electromagnetic interference (Božanić and Sinha, 2019). While the theoretical circuit model suggests that a maximum operating frequency of 2 THz can be achieved based on the physical limits of transistor feature size, practical limitations including mechanical stability and challenges related to parasitic effects, have hindered the progress toward higher operation frequencies (Izumi *et al.*, 2017; Urteaga *et al.*, 2017; Makhlouf *et al.*, 2023).

Besides the transistor technology, electronic diodes are commonly used as terahertz sources, with examples including the Gunn diode, IMPATT diode, and RTD. These diodes share the common characteristic of a negative differential conductance (NDC) region in their current-voltage (*I-V*) curve. A typical RTD structure and its *I-V* curve is shown in Fig. 1.4(a, b). The oscillation principle can be generally explained by equivalent circuits. Material and radiation losses, represented as positive resistances, can damp the oscillation signal. The NDC therefore compensates for these positive resistances, and the remaining *LC* circuit contributes to continuous terahertz oscillation. However, these diodes have different semiconductor layer structures, and their NDC operation principles also differ from each other.

The Gunn diode is composed of n-doped semiconductor material, such as gallium arsenide (GaAs), and operates based on the Gunn effect (Kroemer, 1964). A Gunn diode structure typically includes two heavily n-doped terminals with a thin layer of lightly n-doped material between them. When a voltage is applied, the current initially

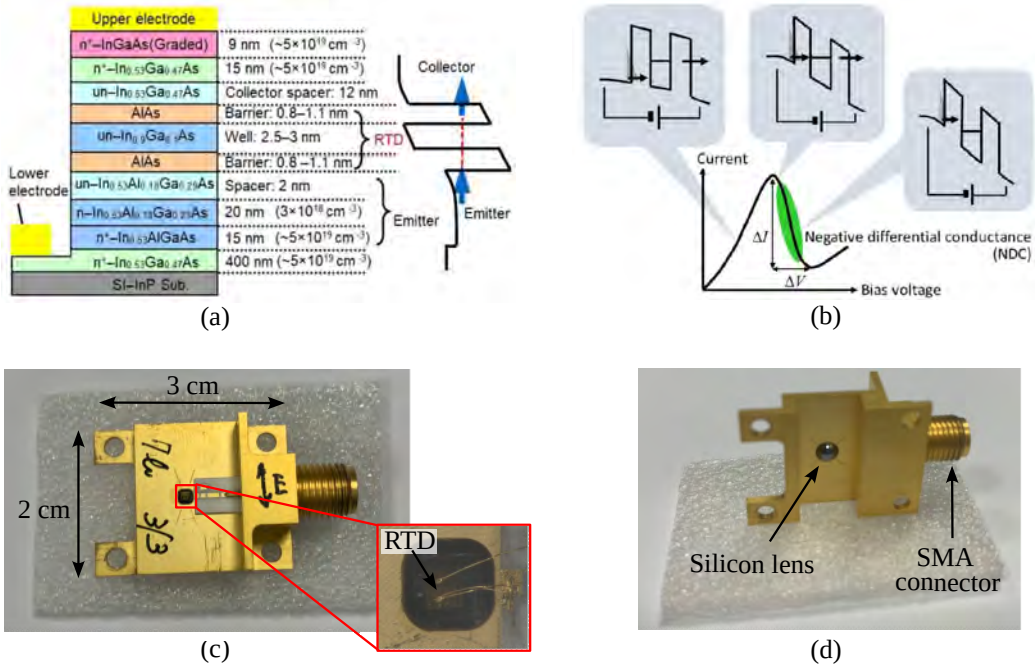

Figure 1.4. Terahertz resonant-tunneling diode (RTD). (a) Typical RTD semiconductor layer structure and (b) its *I*-*V* characteristic. Adopted form Asada and Suzuki (2021). (c, d) Packaged patch-antenna-integrated RTD with a hemispherical silicon lens. The RTD bias voltage is supplied with an SMA feed. The RTD package is fabricated by Tokyo Institute of Technology.

increases with increasing voltage, until the applied voltage is sufficient to create electric field domains within the middle layer. This alteration in conductivity properties leads to a decrease in current, yielding NDC (Khalid *et al.*, 2014).

The IMPATT diode is typically fabricated from compound semiconductors such as silicon or GaAs, featuring multiple junctions and operates based on the avalanche effect. With a high enough bias voltage, carrier electrons gain sufficient kinetic energy to ionize other electrons in the semiconductor material. Under reverse bias voltage conditions, the avalanche effect results in the NDC region (Acharyya and Banerjee, 2014).

The RTD typically consists of an undoped quantum well layer sandwiched between double thin barrier structures, forming a quantum mechanical tunneling region. It operates based on the quantum tunneling effect through a double-barrier structure. RTDs have a resonant energy level that facilitates efficient tunneling when voltage is applied (Asada and Suzuki, 2021). Compared to the other two types of diodes, RTDs benefit from a unique quantum tunneling process that is highly sensitive to the energy levels and barrier thicknesses within the device. The transit time is extremely short due

to the minimal nanometer-scale separation between adjacent energy wells. RTDs are often integrated with slot or patch antennas that can be tuned to match the complex impedance of the RTD, resulting in very compact electronic sources (Asada and Suzuki, 2016). An example of a packaged patch-antenna-integrated RTD with a silicon lens operating at around 300 GHz is shown in Fig. 1.4(c, d). Notably, RTD has achieved an oscillation frequency of 1.98 THz under room temperature, holding a record for the highest fundamental oscillation frequency for electronic sources (Izumi *et al.*, 2017). Despite the fact that RTDs typically operate at a fixed frequency, a slot antenna can be integrated with varactor diodes to develop frequency tunable RTDs for communications applications (Kitagawa *et al.*, 2017). Recent developments, such as the array configuration with patch antennas from Canon, Inc., have achieved over 10 mW output power at 450 GHz (Koyama *et al.*, 2022). The RTD transceiver chip can be integrated with a substrateless dielectric waveguide platform (Yu *et al.*, 2019), demonstrating the promise of RTDs as practical electronic sources (Yu *et al.*, 2022). However, the output power from RTDs as terahertz transmitters remains insufficient for practical wireless communications, and RTDs can only support on-off keying (OOK) modulation through the control of bias voltage, while more complex signal modulation methods are not currently available.

It is worth adding that apart from those compact and integrable fundamental electronic oscillators mentioned earlier, there are alternative types of terahertz sources. Harmonic-based sources, including Schottky diode multipliers and mixers, are predominantly used in commercial terahertz emitters due to their easy integration with hollow waveguides. These devices operate by up-converting radio frequency (RF) signals to terahertz frequencies, and they can benefit from the use of powerful amplifiers. However, the trade-off is that these systems are typically bulkier and less efficient. An example of the VDI signal extension module (SGX), i.e., WR3.4SGX model, which operates in the 220–330 GHz, is shown in Fig. 1.5(a). This model offers options for multiplication by a factor of 9 or 18, allowing the up conversion of RF signals ranging from 24.44–36.67 GHz and 12.22–13.33 GHz to the desired terahertz range. The output power of the SGX is typically low, approximately around 0.6 mW. These devices are commonly paired with a corresponding signal analyzer extension model (SAX) and are often connected to a vector network analyzer (VNA) to characterize electromagnetic wave propagation and transmission. Such configuration provides a broad bandwidth of around 110 GHz, making them suitable for research purposes in laboratory environments, as shown in Fig. 1.5(b).

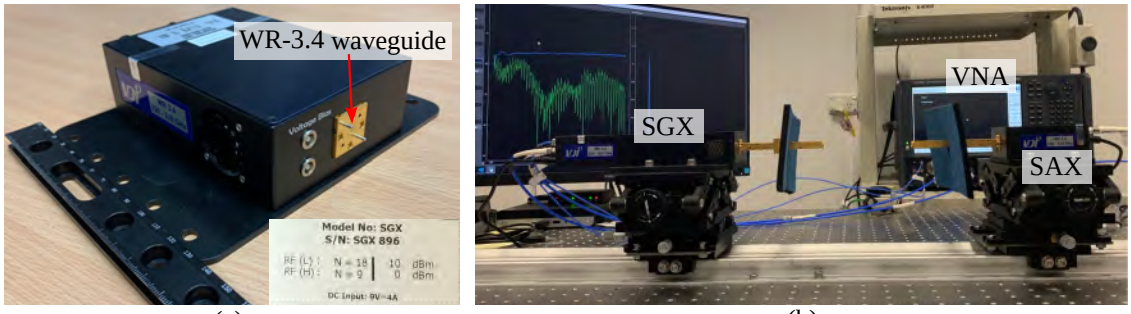

(a) (b)

Figure 1.5. Harmonic-based terahertz source. (a) VDI signal generator extension (SGX) module. The SGX has the function of multiplying the input RF signal frequency to the terahertz range by a factor of 9 or 18. (b) A typical terahertz measurement environment at the Terahertz Engineering Laboratory, the University of Adelaide. The SGX on the left-hand side up-converts the RF signal from the VNA to the WR-3.4 frequency band, and the signal analyzer extension (SAX) module on the right-hand side down-converts the terahertz signals back to RF for characterization using the VNA.

1.2.2 Photonic terahertz generation

Photonic terahertz sources can be typically categorized into pulse radiation mode or continuous-wave radiation mode. Pulse radiation mode can be explained by considering a femtosecond laser burst, which drives a photocurrent with transient time of pico-second level that corresponds to a wide spectral response range of several THz (Burford and El-Shenawee, 2017). On the other hand, the continuous-wave radiation can be explained by considering the frequency-domain signals of two continuous wave laser beams at different optical frequencies, which can be down-converted into terahertz frequency range through photomixing (Ishibashi and Ito, 2022). Photonic-based terahertz sources offer advantages in terms of tunability and coherence, while a limited power output, as well as a complex and costly setup are the major limitations.

Pulse radiation sources rely on photoconductive materials, such as highly resistive semiconductors like low-temperature grown GaAs or InP. These materials can transition from a high resistance state to low resistance when exposed to an optical laser. Typically, a planar metallic antenna, such as a patch or dipole antenna, is integrated with the semiconductor chip and connected to a DC bias voltage. An optical laser illuminates a small gap at the center of the antenna. The applied DC bias separates electrons from holes and generates a photocurrent. This photocurrent causes electrons and holes to drift to the respective contacts of the antenna, emitting terahertz signals into free space (Burford and El-Shenawee, 2017). This structure is commonly referred to as a

photoconductive antenna (PCA). Although PCAs are ideal sources for many THz-TDS systems due to their broad bandwidth, high sensitivity, and rapid response times, their practical applications are primarily limited to fields related to physical sciences such as spectroscopy. Furthermore, since terahertz signals produced by PCAs are not continuous, they are less suitable for communication applications and other engineering-related domains.

Photodiodes are suitable sources for generating continuous-wave terahertz radiation through optical down-conversion. These devices operate based on the principle of the photoelectric effect, where incident light wave energy is absorbed by the semiconductor material, leading to the generation of charge carriers. These carriers are then driven by the intrinsic electric field and bias voltage, resulting in the generation of photocurrent. In the photomixing process, two independent light waves with different frequencies are combined and applied to a photodiode for down-conversion into the terahertz range. For instance, by selecting two lasers with emission frequencies of 193.4 THz and 193.7 THz, a terahertz signal with a frequency of 300 GHz can be generated. One advantage of using photodiodes is the ability to modulate the signal before its conversion to the terahertz range, specifically at the level of the two optical signals. Since these signals are optical, the available bandwidth for modulation is considerably larger compared to electronic up-conversion methods mentioned earlier. However, as a trade-off, the output power of photodiodes is typically lower than that of electronic sources.

Among photodiodes, Positive Intrinsic Negative photodiodes (PIN-PDs) are commonly used due to their simple structure and cost-effectiveness. The structure of a PIN-PD is illustrated in Fig. 1.6(a), and an example of a packaged InGaAs PIN-PD with a bow-tie antenna and an integrated silicon lens from Toptica is also illustrated in Fig. 1.6(c). However, one major limitation of PIN-PDs is that the transit time for holes traveling from the intrinsic layer into the p-layer is slow due to their high effective mass in semiconductors. This discrepancy leads to a saturated high-frequency photocurrent. For instance, the output power from a typical PIN-PD is 100 µW at 500 GHz but drops to 10 µW at 1 THz (Nellen *et al.*, 2020).

To address this limitation and achieve higher-speed responsivity with increased saturation current, the Uni-Traveling Carrier photodiode (UTC-PD) was developed. The structure of the UTC-PD is depicted in Fig. 1.6(b) (Nellen *et al.*, 2020). Building upon the PIN-PD foundation, an additional p-type absorption layer is added next to an intrinsic

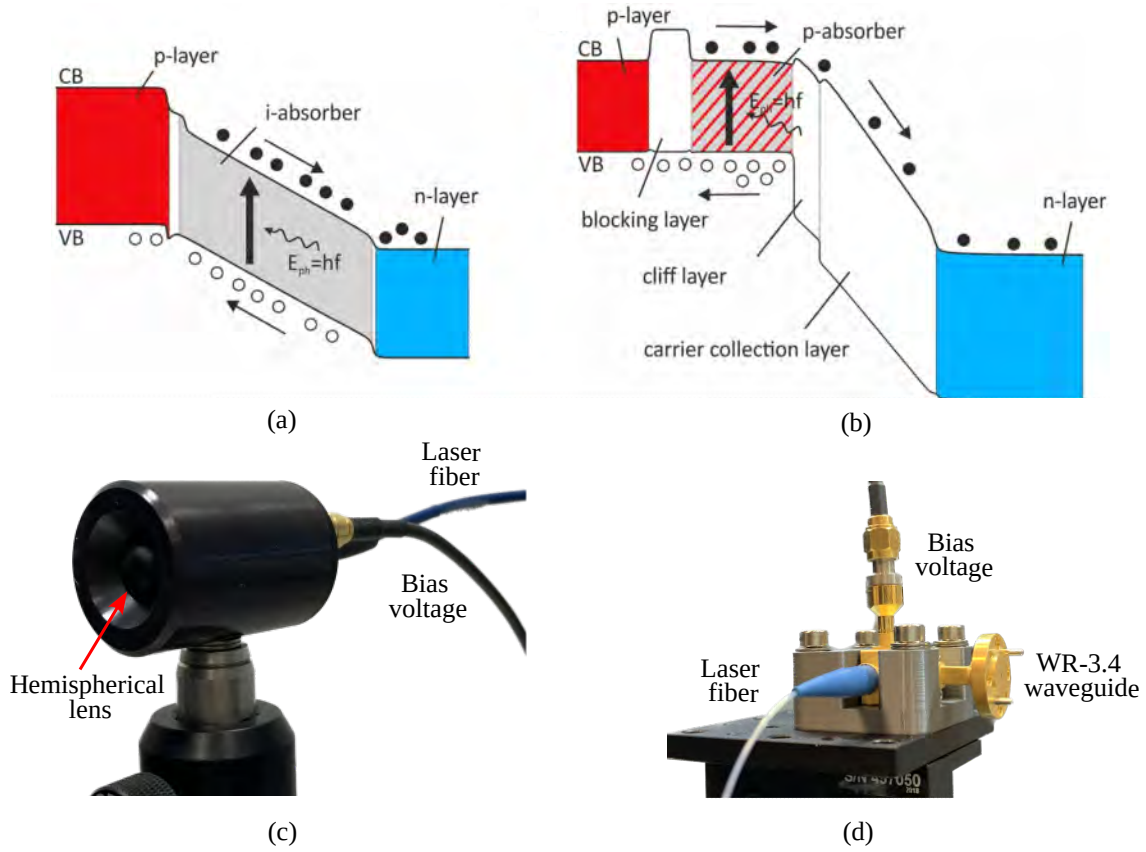

Figure 1.6. Different types of photodiodes. Schematic band diagram of (a) PIN-PD and (b) UTC-PC. Adopted from Nellen *et al.* (2020). (c) Packaged PIN-PD integrated with a hemispherical lens from Topitca. (d) Packaged UTC-PD integrated with a WR-3.4 waveguide from Nippon Telegraph and Telephone Corporation (NTT).

carrier collection region. This modification allows the slower-traveling holes to reach the p-layer quickly without crossing the depletion region. As the name suggests, only fast electrons are injected into the depleted carrier collection layer, resulting in carriers traveling in a single direction (Ishibashi *et al.*, 1997). Consequently, the photo response of the UTC-PD is primarily determined by the electrons travelling in the structure, enabling higher operation frequencies of up to 2.2 THz (Makhlouf *et al.*, 2021). Similar to PIN-PDs, UTC-PDs can be integrated with various antennas, such as bow-tie antennas and slot antennas. The use of an external silicon lens can further enhance the radiation performance. Additionally, UTC-PDs can also be integrated with coplanar waveguides and transition to hollow waveguides. An example of an integrated UTC-PD with a WR-3 hollow waveguide, is presented in Fig. 1.6(d). Recent research efforts have focused on improving the output power of UTC-PDs, including photodiode arrays (Bowers *et al.*, 2014) and monolithically integrated circuits to match the impedance

of UTC-PDs and integrated waveguides (Latzel *et al.*, 2017). The maximum reported output power from UTC-PD at 300 GHz can reach approximately 1 mW (Grzeslo *et al.*, 2023).

In contrast to down-conversion technology, there is an alternative source known as quantum cascade lasers (QCLs), which are direct optical emitters of terahertz radiation and can operate in both pulse mode and continuous wave mode. A terahertz QCL's active region typically comprises multiple quantum wells stacked between two metal layers within a waveguide. These quantum wells are injected with direct current to energize the electrons, allowing them to cascade between the coupled quantum wells in a specific sequence, resulting in the generation of photon energy for terahertz radiation. The output energy level, i.e., typically above 1 mW, can be controlled by the choice of materials and the thickness of the quantum wells (Köhler *et al.*, 2002). It is worth noting that QCLs are traditionally used in the mid-infrared to far-infrared range. However, recent advancements have shown that QCLs can be scaled to produce frequencies down to approximately 1.3 THz (Wen and Ban, 2021). One significant limitation of terahertz QCL devices is the requirement for a cooling system, which restricts their practical applications. A recent progress on room-temperature QCLs with difference frequency generation may provide an attractive pathway, despite a degraded efficiency caused by photon flux conversion (Fujita *et al.*, 2018).

1.3 Planar terahertz antennas and lenses

While substantial efforts have been invested to improving terahertz source output power, it is important to acknowledge that available power levels still remain low. As a result, the practical transmission of terahertz waves in free space is unlikely to be isotropic, where a broadcast signal can be received in many different locations. According to the Friis transmission equation (Friis, 1946), the free-space path loss is proportional to the square of the frequency and propagation distance. Furthermore, terahertz transmission is significantly affected by atmospheric attenuation, primarily due to interference with water vapor molecules. To address this, the terahertz spectrum has been divided into specific windows, such as 220–330 GHz, 625–725 GHz, and 780–910 GHz, where atmospheric attenuation is minimum (Nagatsuma *et al.*, 2016), as shown in Fig. 1.7. The substantial power loss during terahertz wireless transmission, coupled with the limited output power from sources, results in degraded received signal quality.

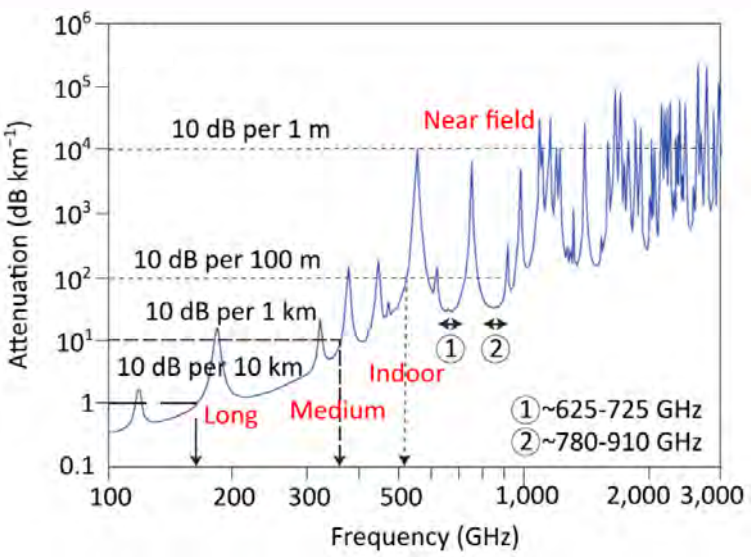

Figure 1.7. Atmospheric attenuation at terahertz frequency. The frequency band is divided into several transmission windows to avoid resonance peaks. Frequency below 500 GHz is suitable for outdoor medium- or long-range wireless communications, while frequency above 500 GHz is only suitable for near-field applications indoor. Adopted from Nagatsuma *et al.* (2016).

This often leads to a low signal-to-noise ratio (SNR), which can impact the channel capacity for communications and degrade system image quality. To mitigate these challenges, terahertz radiation between transceivers is typically highly directive, to counteract the impact of large path loss, and the radiative elements are highly efficient, to preserve the precious power.

In theory, it is possible to scale up lower-frequency devices, circuits, and antennas operating at the microwave or millimeter-wave range to their higher terahertz frequency counterparts by reducing the device size. Conversely, higher-frequency devices, waveguides, and lenses that operate at optical frequencies can be scaled down to terahertz frequencies by increasing their size accordingly. This scalability is facilitated by advanced micro-fabrication technologies such as computer numerical control (CNC) milling (Nguyen and Kim, 2023), silicon micromachining (Gomez-Torrent *et al.*, 2020a), thin-film spin coating processes (You *et al.*, 2022), and advanced 3-D printing technology (Gao *et al.*, 2023). These technologies enable the development of terahertz antennas and lenses that are applicable to terahertz sources. Some recent examples include on-chip antennas, both alone (Gao and Chan, 2024b) and in combination with dielectric lenses (Gao and Chan, 2022b, 2024a) or resonators (Kong *et al.*, 2021). However, it is important to note that the antenna and lens designs suitable for the terahertz frequency band

remain limited. Careful considerations of material choices and design processes related to fabrication resolution and accuracy are essential to achieve a compact, cost-effective, and source-integrable solution that maintains performance consistent with that achieved in the original frequency bands.

1.3.1 Antennas

Terahertz antennas derived from microwave technology are primarily implemented as metallic antennas. Among these metallic antennas, horn antennas are the most commonly used due to their stable radiation pattern, high-gain performance, large bandwidth, and low cross-polarization levels. An example of the VDI WR-3.4 diagonal horn antenna is presented in Fig. 1.8, which consists of a short rectangular waveguide at one end, expanding into an open-ended diagonal-shaped aperture on the other side. This design enables a gradual transition of electromagnetic waves from the waveguide to free space, resulting in a narrow beamwidth. With the corrugated walls, gain performance can further enhanced, while the bandwidth becomes narrower (Tajima *et al.*, 2014; Gonzalez *et al.*, 2017). Despite their excellent performance, integrating horn antennas with terahertz sources is challenging and their fabrication remains complex and costly. Unlike in the microwave range, where aluminium is a cost-effective material choice, terahertz frequencies require the use of gold or gold coating to provide high conductivity, as metals are far from being perfect conductors in this range. Additionally, due to surface roughness, there is an increasing scattering loss, resulting in further heightened ohmic losses (Luk *et al.*, 2017). Furthermore, horn antennas are typically bulky and not suitable for practical applications. For instance, the VDI diagonal horn

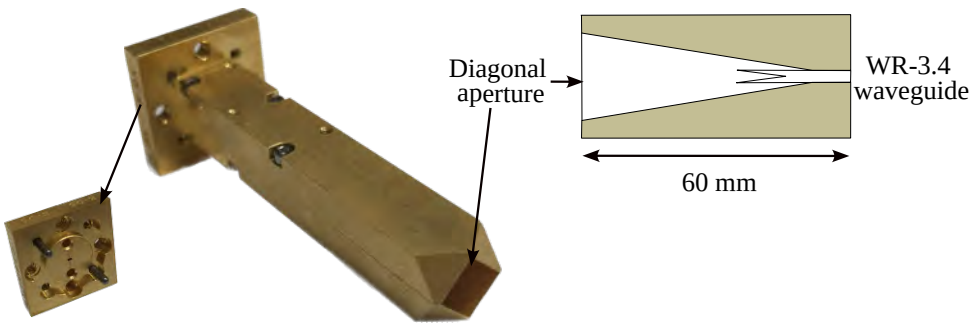

Figure 1.8. VDI WR-3.4 diagonal horn antennas. The horn antenna gradually transitions electromagnetic wave from the WR-3.4 waveguide slot to an large diagonal aperture, with a device length of around 60 mm.

antenna has a length around 60 mm. To achieve a cost-effective, compact, and integrable terahertz antenna, it is essential to further explore planar antenna designs and therefore this section will focus on various types of planar terahertz antennas.

Planar terahertz antennas are typically designed with a patterned metallic layer deposited on a dielectric substrate. These patterned metallic layers can involve various shapes, such as slot antennas (Asada and Suzuki, 2016), patch antennas (Okada *et al.*, 2015), bow-tie designs (Diebold *et al.*, 2016), and spiral configurations (Li *et al.*, 2023d), as illustrated in Fig. 1.9. The radiation properties of these antennas follow the conventional microwave theory, i.e., bow-tie antennas offering a wide bandwidth (Durgun *et al.*, 2011) and spiral antennas generating circularly-polarized (CP) radiation (Zhu *et al.*, 2017). When scaling up from the microwave range, a microstrip line can be employed as the feeding structure, with the planar metallic antenna integrated onto a substrate

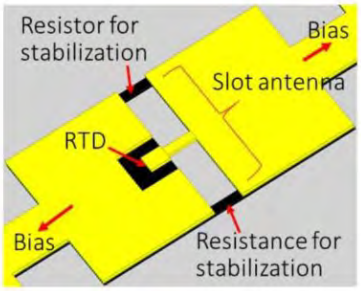

(a)

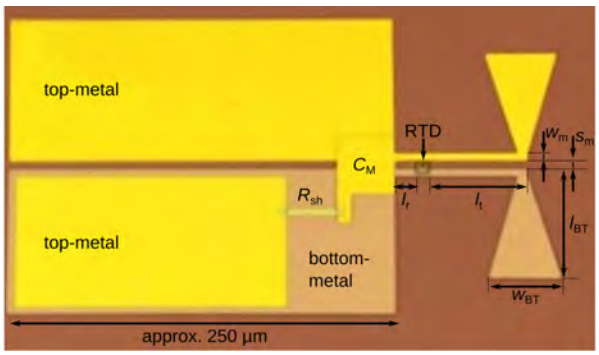

(c) © 2016 IEEE

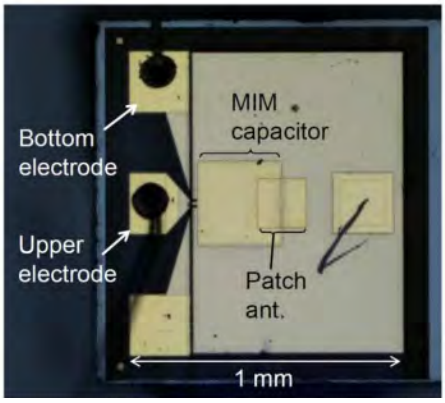

(b) © 2015 IEEE

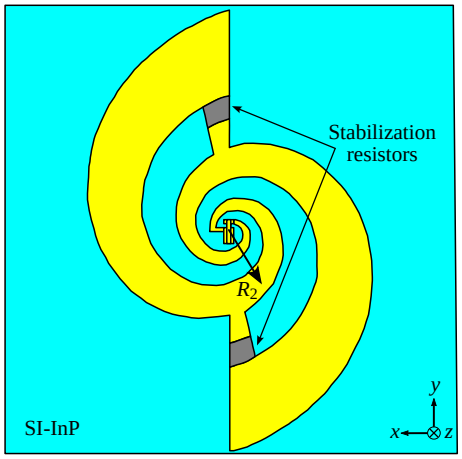

(d) © 2023 IEEE

Figure 1.9. Terahertz planar antennas with patterned metallic layers. (a) Slot antenna Adopted from Asada and Suzuki (2021) (b) Patch antenna Adopted from Okada *et al.* (2015) (c) Bow-tie antenna Adopted from Diebold *et al.* (2016) (d) Log-spiral antenna. Adapted from Li *et al.* (2023d). The excitation sources for (a–d) are RTDs.

either with or without a ground plane (Sharma and Singh, 2009; Diebold *et al.*, 2016). Planar metallic patterned antennas can also be directly excited by either electronic sources like RTDs, or photonic sources like laser pulses. These sources are typically placed at or near the center of the antenna, resulting in a highly compact antenna system. Nevertheless, the circuit model and impedance relationships for different pattern shapes and various excitation methods require further exploration. One challenge of such combination of planar metallic antennas with a dielectric substrate is that, as the frequency approaches the terahertz range, surface wave effects become significant. This drawback leads to considerable energy loss during operation and a notable decrease in antenna radiation efficiency. This effect is enhanced when radiation angle exceeds the cut-off angle, causing energy to become trapped inside the dielectric substrate (He *et al.*, 2020). Consequently, efforts were made to suppress surface waves (Kong *et al.*, 2021; Gao and Chan, 2022a), and it is often necessary to incorporate a secondary radiator, such as lenses, to efficiently capture and outcouple the energy (Li *et al.*, 2023d).

Leaky-wave antennas (LWAs) are a type of planar antennas developed from microwave technology that exploits the electromagnetic wave propagation along a wave-guiding structure, such as air-filled waveguide or microstrip line, where electromagnetic waves are leaking and radiating into free space. One of the key advantages of LWAs is their simple feeding structure, eliminating the need for complex and expensive feed networks typically used in phased arrays (Jackson *et al.*, 2012). The guiding structure can be either a uniform structure that supports an electromagnetic wave with propagation constant β smaller than the free-space wavenumber k_0 (Guerboukha *et al.*, 2023), or it can be a periodic structure that supports a non-radiating fundamental mode with a propagation constant β larger than the free-space wavenumber k_0, and the radiation occurring from the $n = -1$ space harmonic (Murano *et al.*, 2017). Examples of two types of LWA are depicted in Fig. 1.10(a, b). A notable characteristic of LWAs is their frequency-dependent beam steering, where the main lobe direction is determined by the operating frequency. This unique feature finds applications in short-range radar systems, which can exploit the frequency scanning capability (Murano *et al.*, 2017; Matsumoto *et al.*, 2020). Recent developments include LWAs integrated with photonic sources, indicating their progress towards practical applications (Lu *et al.*, 2021). Besides traditional metallic LWAs, there are silicon-based LWAs that enable continuous leakage of a slow wave through a tailored wave tunneling process from a channel waveguide (Headland and Withayachumnankul, 2022), as shown in Fig. 1.10(c). However, LWAs have intrinsic limitations, including their 1-D physical aperture that limits gain, and their angular dispersion, making them

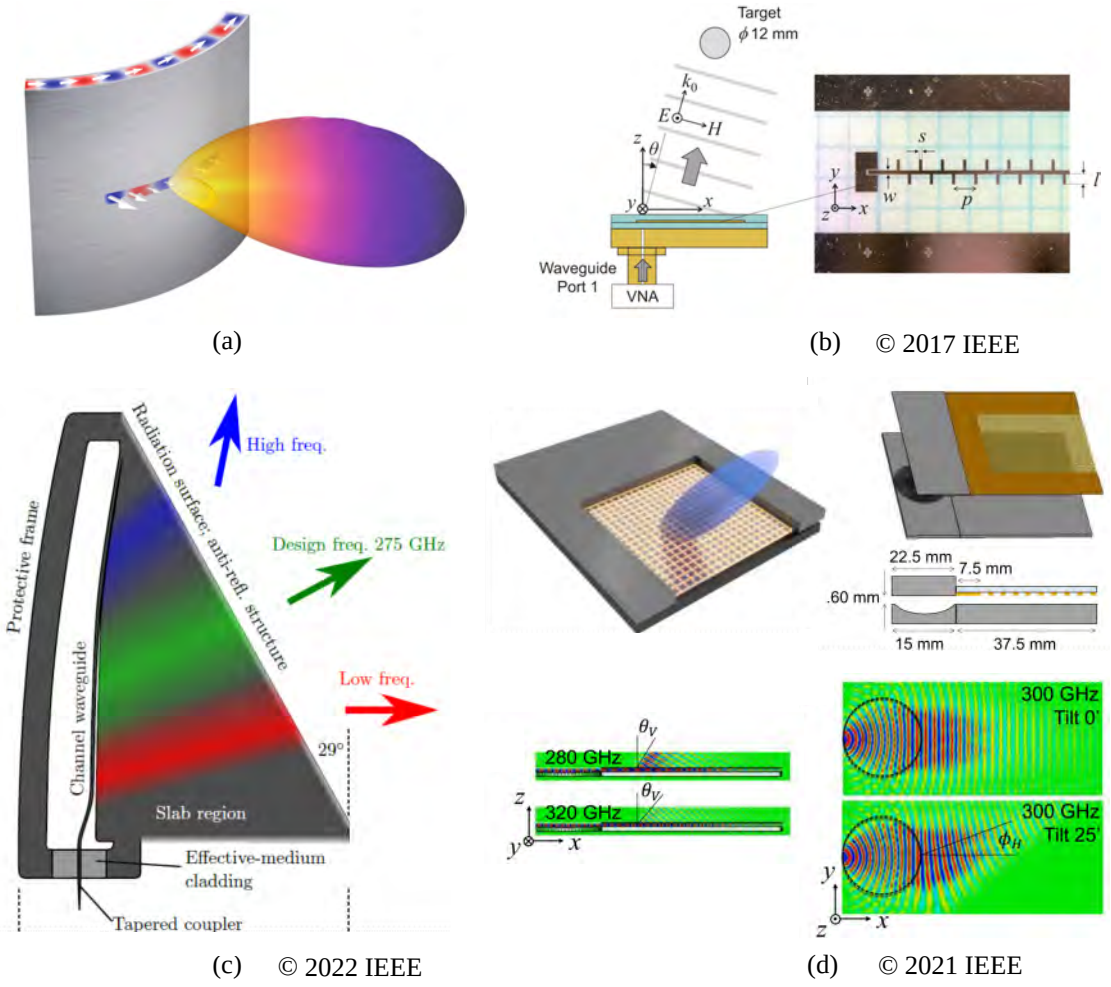

(a) (b) © 2017 IEEE

(c) © 2022 IEEE (d) © 2021 IEEE

Figure 1.10. Terahertz leaky-wave antennas. (a) Parallel-plate waveguide-based LWA. A rectangular slot is cut on one side of the waveguide to allow continuous radiation (Guerboukha *et al.*, 2023). (b) Microstrip line-based LWA. Periodical gratings are constructed along the microstrip line to allow wave leakage into free-space (Murano *et al.*, 2017). (c) Dielectric channel waveguide-based LWA. The separation distance between the channel waveguide and the dielectric slab gradually changed, allowing the leakage energy enter the silicon slab from different directions for different frequencies (Headland and Withayachumnankul, 2022). (d) 2-D LWA. Beam steering with one dimension is controlled by frequency, while the other dimension is controlled by mechanically rotating the source position along a Lundberg lens. Adapted from Sato and Monnai (2021).

unsuitable for communications systems. While 2-D beam steering technologies have been developed, they often involve more complex structures (Gomez-Torrent *et al.*, 2020a) and may rely on a combination of baseband signal control (Wu *et al.*, 2022b) or mechanical rotation (Sato and Monnai, 2021), as shown in Fig. 1.10(d).

Phased array antennas represent a circuit-integrable solution for terahertz planar antennas, utilizing multiple unit cell elements to create a large antenna aperture capable of

steering the beam to specific directions (Monnai *et al.*, 2023). Typically, a local oscillator (LO) signal is used as an input and distributed equally through a distribution network, such as an H-tree distribution (Sengupta and Hajimiri, 2012) or an oscillator-coupled network (Tousi and Afshari, 2015). This LO signal is then transmitted to each unit cell element via transmission lines with equal LO signal delays, ensuring consistent frequency, amplitude, and phase across the array. The equally-distributed LO signal is then up-converted to the terahertz frequency range using a frequency multiplier, and phase shifters are employed to achieve coherent power combination and meet beam steering requirements. A significant challenge faced by phased array antennas is that the LO signal experiences considerable attenuation due to inefficient power splitters, bending structures, and lossy transmission lines. As a result, a large number of amplifiers are required to compensate for these losses, leading to a high-power consumption. Furthermore, electronically controllable phase shifters are not widely available in the terahertz range, as they often rely on CMOS varactors that typically operate below 100 GHz (Quemerais *et al.*, 2015). While recent advancements have demonstrated phased array antennas operating around 260 GHz with a steerable beam within 36°, they face challenges related to insufficient output power due to the lack of power amplifiers, resulting in relatively low data rates (Abdo *et al.*, 2022, 2023). Additionally, beam-forming without phase shifters relied on the combination of standing and travelling waves to create the necessary phase shift between sources (Jalili and Momeni, 2019). However, significant power requirement, lack of efficient phase shifters, and limited bandwidth have hindered the development of terahertz phased array antennas (Headland *et al.*, 2018a).

1.3.2 Lens

Terahertz lenses derived from the photonic frequency range take primarily the form of dielectric lenses. While metallic parabolic reflectors are available, they are often bulky and not easily integrable with most terahertz sources. Therefore, this section will focus on dielectric lenses. Among terahertz dielectric lenses, hemispherical lenses or hyper-hemispherical lenses are the most commonly used, due to their stable high-gain performance and wide bandwidth. These lenses are well-suited for integration with terahertz sources as secondary radiators (Asada and Suzuki, 2016) or with waveguides to provide collimated wavefront output (Llombart *et al.*, 2011). In terms of material choice, dielectric materials with low permittivity are readily available, and these lenses

can be manufactured using conventional CNC machining (Konstantinidis *et al.*, 2017) or 3-D printing technology (Gao *et al.*, 2023). While lenses with low permittivity, such as Teflon, offer better impedance matching to terahertz on-chip sources at a low-cost (Gao and Chan, 2024b), the overall size of such lenses can be relatively large, and dielectric losses are non-negligible. High permittivity materials like silicon are also available, and silicon micromachining allows for smaller lens sizes, although the fabrication process can be more complex and costly (Llombart *et al.*, 2011). While hemispherical lens setups have been widely implemented in various applications, such as astronomy (Baselmans *et al.*, 2022) or industry (Leuchs *et al.*, 2022), there is a growing need for more compact and planar lens antennas, as the size of traditional hemispherical lenses is considered too bulky. A classical solution derived from optical technology is the Fresnel zone plate, comprising adjacent transparent and opaque zones with widths corresponding to usually half of the operation wavelength (Hristov, 2016). While recent fabrication advancements have led to the development of terahertz Fresnel zone plates, their efficiency remains typically low due to innate energy blockage of the design (Ayyagari *et al.*, 2023).

Terahertz planar lens antennas are typically designed based on diffractive lens principles to minimize the device profile and material loss. Advanced 3-D printing technology has played a crucial role in creating these lenses, allowing for precise control of small pillars with varying heights to form terahertz Fresnel lenses (Yi *et al.*, 2016; Zhu *et al.*, 2021). This technology also enables the design of gradient index (GRIN) lenses by controlling the fill factor of local printing area, varying the refractive index within the lens and thus influencing the optical path. For example, a GRIN lens integrated with a printed quarter wave plate was demonstrated to generate circularly polarized radiation at the WR-3 band (Wu *et al.*, 2019a). Several examples of 3-D printed lens antennas are illustrated in Fig. 1.11(a–c). In addition to high-gain lens antennas, 3-D printed lenses are also suitable for focusing applications or multi-spot focusing (Wu *et al.*, 2022a), as demonstrated in the example of a 300 GHz focusing lens shown in Fig. 1.11(d). While 3-D printed lenses offer benefits such as low cost and ease of fabrication, they have a fundamental limitation in terms of non-negligible dielectric losses, which are typically above 2 dB.

To minimize the dielectric loss, high-resistivity silicon is a suitable choice for terahertz planar lens antennas, with a matching layer for efficient energy outcoupling to free-space (Lees *et al.*, 2024; Li *et al.*, 2024b). The GRIN lens can be achieved through implementing effective medium principle, allowing control of the effective refractive index in local

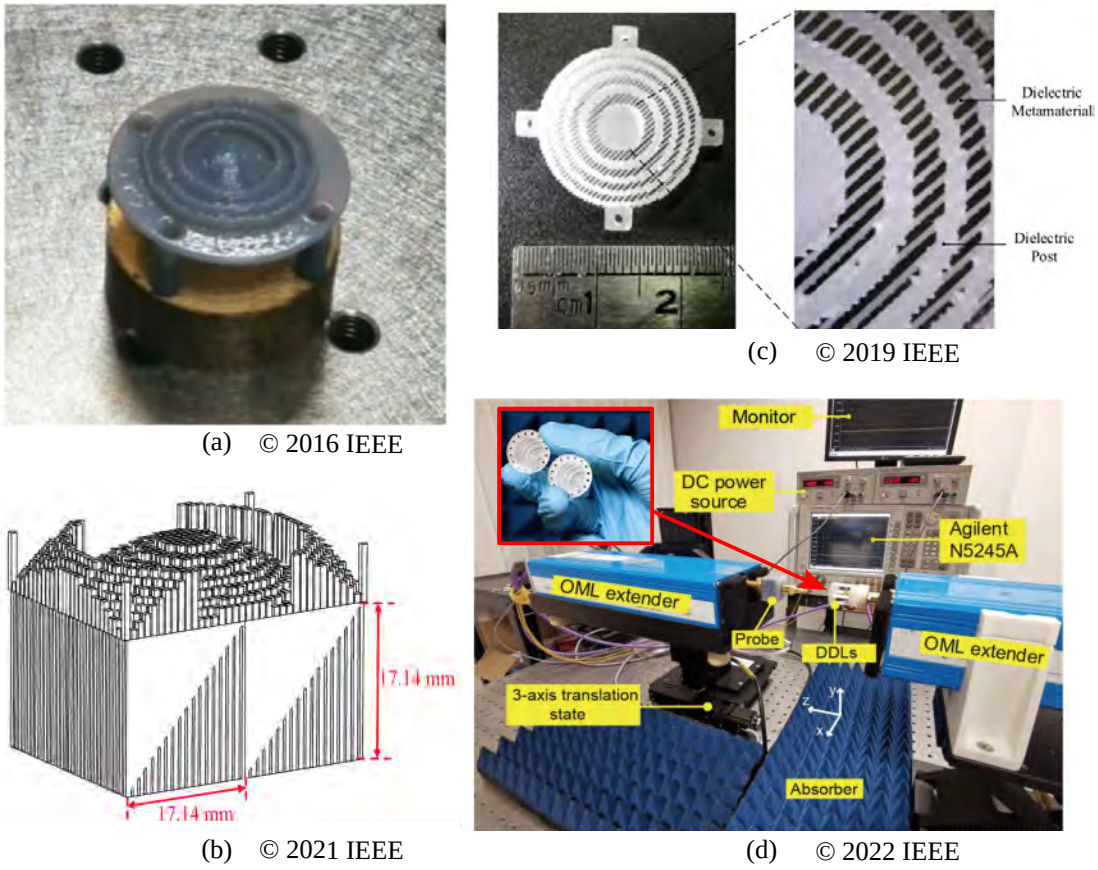

(a) © 2016 IEEE

(c) © 2019 IEEE

(b) © 2021 IEEE

(d) © 2022 IEEE

Figure 1.11. Terahertz 3-D printed lenses. (a) Fresnel discrete lens integrated with a WR-3 open waveguide (Yi *et al.*, 2016). (b) Fresnel discrete lens integrated with a polarization beam splitter. Adapted from Zhu *et al.* (2021). (c) GRIN Fresnel lens with a quarter-wave plate composed of diagonal air gratings for CP radiation (Wu *et al.*, 2019a). (d) Near-field focus scanning lens. Adapted from Wu *et al.* (2022a).

areas. However, current fabrication methods, such as deep reactive ion etching (DRIE) or direct laser etching, face challenges related to limited etching depth, thus hindering the attainment of a full phase coverage range with the effective medium, as discussed by Li *et al.* (2024b). Consequently, silicon-based planar lens antennas for terahertz applications are currently limited to 2-D platforms, with end-fire lenses of physical aperture restricted to 1-D, as shown in Fig. 1.12. Such end-fire lenses provide a radiation pattern with a narrow beamwidth in one plane, while a fan beam occurs out of plane. These 2-D structures typically rely on a substrateless dielectric waveguide feed, using either a photonic crystal waveguide (Yu *et al.*, 2019) or an effective medium waveguide (Gao *et al.*, 2021). End-fire lenses are constructed to radiate terahertz waves into free space, and these lenses can be designed using effective medium techniques, where the etched air holes depth depends on the silicon substrate thickness, and the air hole sizes

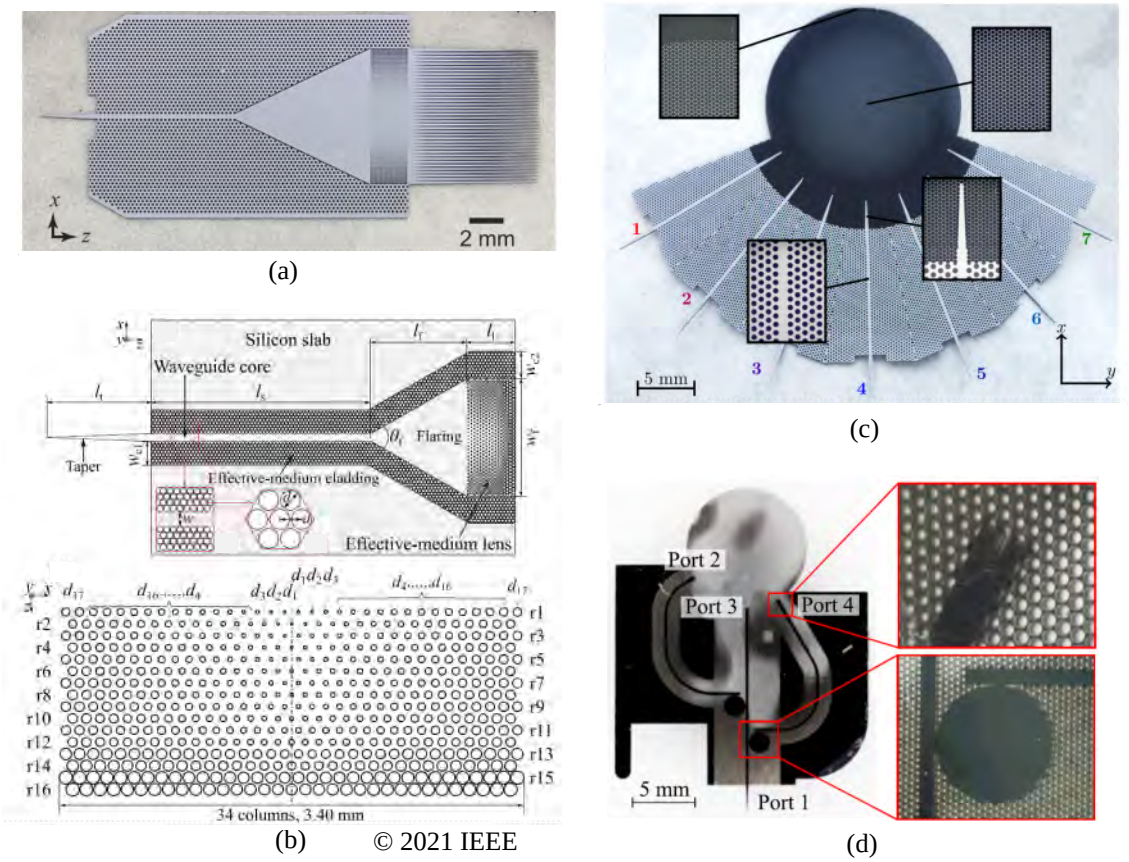

© 2021 IEEE

Figure 1.12. Terahertz end-fire antennas based on the silicon waveguide platform. (a) Effective medium-based GRIN lens with rod-array antenna (Withayachumnankul *et al.*, 2018). (b) Effective medium-based GRIN lens with anti-reflection layer (Liang *et al.*, 2021). Luneburg lens fed by (c) waveguides from different directions (Headland *et al.*, 2018b) and (d) waveguide with switchable directions. Adapted from Dechwechprasit *et al.* (2023).

are varied to form GRIN lenses (Withayachumnankul *et al.*, 2018). Further research has indicated that performance can be enhanced with the addition of an effective medium-based anti-reflection layer before transitioning into free space (Liang *et al.*, 2021). In addition to GRIN lenses, planar Luneburg lenses can be created to enable scanning capabilities (Headland *et al.*, 2018b). The Luneburg lens can be fed by waveguides from different directions or using multiport switches (Dechwechprasit *et al.*, 2023). Several end-fire antennas based on the substrateless waveguide platform are shown in Fig. 1.12.

Metasurfaces derived from the field of flat optics offer an attractive option for terahertz planar lens structures. Metamaterials, made up from sub-wavelength unit cells, with their ability to effectively manipulate electromagnetic waves in terms of amplitude, phase, and polarization, provide a comprehensive platform for planar terahertz lens design. Metasurfaces can be realized using various materials for various functions. For

instance, dielectric silicon resonators can be employed as reflectarrays to create quarter-wave or half-wave mirrors (Lee *et al.*, 2018) or as absorbers (You *et al.*, 2020b). In addition to an all-dielectric metasurface, advanced fabrication techniques allow the deposition of a thin patterned gold film on a dielectric substrate, expanding the design possibilities. Such metasurfaces can be used as transmitarrays with various functionalities. For example, a structure with three gold layers separated by two dielectric layers can serve as a quarter-wave (You *et al.*, 2020a) or a half-wave plate (You *et al.*, 2021), and can be exploited for polarization control over an ultra-wide bandwidth (Ako *et al.*, 2020). In the case of discrete lens design, precise phase control of the unit cell is crucial. The phase response of the unit cell should cover a range of at least 2π to construct a discrete Fresnel-equivalent lens (Chang *et al.*, 2017). A terahertz high-gain metasurface lens based on a tri-layer metasurface has been demonstrated by Medrar *et al.* (2021). A similar lens antenna using a frequency-selective surface (FSS) has also been shown by Hafezi and Sarabandi (2023). Preceding the metamaterial concept, FSSs can be any periodic structure, with the period falling within half of a wavelength. Unlike metamaterials, FSSs do not require homogenization and typically exhibit narrowband characteristics (Gu *et al.*, 2020). Metasurface lenses also found applications in various imaging scenarios (Yang *et al.*, 2014; Song *et al.*, 2024). While these planar metasurface lenses offer high integrability with sources, it is important to note that they still exhibit non-negligible losses, with experimental results typically suggesting a transmission efficiency of around 80% (You *et al.*, 2021).

1.4 Thesis outline and original contributions

While terahertz applications show promise in various fields, the limited output power from both electronic-based and photonic-based sources has hindered the development of practical terahertz applications. Therefore, to save the precious terahertz power, the design of efficient antennas and lenses becomes crucial for enabling the practical implementation of terahertz applications. Traditional antennas and lenses, derived from microwave and optical technologies, are often bulky, lossy, and expensive. Hence, there is an urgent need to explore planar solutions for highly efficient antennas and lenses tailored specifically to the terahertz range. These solutions should be cost-effective, capable of significantly reducing the device profile, and minimizing additional losses. Furthermore, these solutions should have the ability to integrate with sources for system compactness. This thesis aims to investigate innovative approaches to terahertz highly

efficient planar antennas and lenses with integrated sources. These components are expected to solidly support practical and efficient terahertz applications.

This thesis consists of seven chapters, with five chapters dedicated to original contributions. The initial chapter provides essential background knowledge and an overview of relevant literature. The final chapter offers a summary of the findings and an outlook for future research. Chapters are structured as follows:

Chapter 1 (Introduction): provides essential background knowledge on terahertz technology, advanced terahertz sources, and planar antennas and lenses. The literature review in this chapter offers a detailed examination of various electronic-based and photonic-based terahertz sources and source-integrable planar antennas and lenses, with a comprehensive analysis of their performance, applicability, and limitations in the context of terahertz applications.

Chapter 2 (Original contribution): presents an original contribution involving a series-fed patch array antenna integrated with a structure-simplified RTD source. The original structure-simplified RTD exhibited unsatisfactory radiation performance, with a main lobe tilted away from the broadside. In response, the bias lines of the RTD structure are extended, mitigating the interference between RTD and bias pads, and enabling controllable surface wave propagation. This extended bias line structure incorporates a series-fed patch array antenna, directing the surface wave towards the broadside. Experimental validation demonstrates that the RTD with the series-fed patch array antenna achieves a broadside main lobe, along with a narrower beamwidth and a lower sidelobe when compared to the original RTD. The content of this chapter has been presented at conference Li *et al.* (2021) and published in Li *et al.* (2023c).

- **Li-M. S.**, Suzuki-S., Fumeaux-C., and Withayachumnankul-W. (2021). Improving the radiation performance of resonant-tunneling diode by using planar metallic arrays, *2021 46th International Conference on Infrared, Millimeter, and Terahertz Waves (IRMMW-THz)*, Chengdu, China, pp. 1–2.
- **Li-M. S.**, Mai-T. V., Fumeaux-C., Suzuki-S., and Withayachumnankul-W. (2023c). Terahertz resonant-tunneling diode with series-fed patch array antenna, *IEEE Transactions on Terahertz Science and Technology*, **13**(2), pp. 178–187.

Chapter 3 (Original contribution): presents an original contribution involving a log-spiral antenna integrated with a cavity RTD source. Building upon the insights gained

from the previous RTD with a series-fed patch array design, the extended bias lines with surface wave propagation, are further explored as a platform for innovation. The extended bias lines are configured in a log-spiral pattern to generate circularly-polarized (CP) radiation. Simulation results illustrate a broad operating band with an axial ratio below 3 dB and a narrow broadside beamwidth. The content of this chapter has been presented at conference Li *et al.* (2023d).

- **Li-M. S.**, Suzuki-S., Fumeaux-C., and Withayachumnankul-W. (2023d). Resonant-tunneling diode with spiral bias connections for circularly polarized radiation, *2023 48th International Conference on Infrared, Millimeter, and Terahertz Waves (IRMMW-THz)*, Montreal, Canada, pp. 1–2.

Chapter 4 (Original contribution): presents an original contribution involving a tri-layer metasurface lens for near field beam shaping. The Gaussian beam generated from a diagonal horn antenna is converted into a flat-top beam through the metasurface lens. The process involves obtaining an appropriate phase profile using a modified iterative algorithm. Additionally, the spherical incoming wavefront is considered to achieve a compact illumination system, given that the metasurface is placed in the near-field region of the source. The discrete phase profile are mapped to the metasurface unit cells to create the planar metasurface lens. Simulations and measurement results validate the successful conversion from a Gaussian to a flat-top beam, with a high conversion efficiency over 80%. The content of this chapter has been presented at conference Li *et al.* (2022b) and published in Li *et al.* (2023b).

- **Li-M. S.**, Fumeaux-C., and Withayachumnankul-W. (2022b). Terahertz beam shaping: Gaussian to flat-top beam conversion through tri-layer metasurface, *2022 47th International Conference on Infrared, Millimeter, and Terahertz Waves (IRMMW-THz)*, Delft, Netherlands, pp. 1–2.
- **Li-M. S.**, Ako-R. T., Sriram-S., Fumeaux-C., and Withayachumnankul-W. (2023b). Terahertz metasurface for near-field beam conversion, *Optics Letters*, **48**(8), pp. 2202–2205.

Chapter 5 (Original Contribution): presents an original contribution involving a planar high-gain silicon cavity lens antenna based on effective medium for wireless communications. The proposed lens antenna is constructed using a single 2-mm thick silicon

wafer. To address phase coverage limitations stemming from fabrication constraints, specifically the tapered side walls of etched air holes, effective medium including different air hole patterns are laser-etched on both sides of the silicon wafer to serve as GRIN lenses for phase compensation. Simulation and measurement results validate the high-gain performance, achieving approximately 19 dBi, and a substantial 3-dB bandwidth of around 29%. This design is notable for providing the smallest device profile among state-of-art integrable terahertz lens antennas. The content of this chapter has been presented in conferences Li *et al.* (2022a) and Li *et al.* (2023a), and is published in Li *et al.* (2024b).

- **Li-M. S.**, Fumeaux-C., and Withayachumnankul-W. (2022a). 275-GHz planar high-gain resonant cavity antenna with effective medium, *2022 International Symposium on Antennas and Propagation (ISAP)*, Sydney, Australia, pp. 121–122.
- **Li-M. S.**, Ako-R. T., Sriram-S., Fumeaux-C., and Withayachumnankul-W. (2023a). High-gain, low-profile, integrable planar lens antenna at 275 GHz, *2023 IEEE 11th Asia-Pacific Conference on Antennas and Propagation (APCAP)*, Guangzhou, China. **(Invited)**.
- **Li-M. S.**, Ako-R. T., Sriram-S., Fumeaux-C., and Withayachumnankul-W. (2024b). Terahertz planar cavity antenna based on effective medium for wireless communications, *IEEE Transactions on Terahertz Science and Technology*, **14**(2), pp. 248–257.

Chapter 6 (Original contribution): presents an original contribution involving a 3-D printed frequency-diverse antenna for direction-of-arrival estimation. The proposed lens antenna consists of an oversized cavity containing multiple metallic scatters with random orientations, along with a 3-D printed lens featuring random pillar heights. This arrangement fully breaks the symmetry of the antenna system, resulting in entirely random and uncorrelated radiation patterns across the operating frequency range. The antenna is simulated, and the performance is analyzed with a machine learning algorithm. In the experimental measurements, the predicted direction-of-arrival closely matches the expected results. Despite its non-planar structure, this design offers an efficient, compact, and single-component solution for estimating the direction-of-arrival of terahertz signals. The author's original contribution includes the antenna's design and simulation, along with the experimental measurements and data collection. The content of this chapter is accepted for publication in Li *et al.* (2024a).

- **LI-M. S.**, ABDULLAH-M., HE-J., WANG-K., FUMEAUX-C., AND WITHAYACHUMNANKUL-W. (2024a). Frequency-diverse antenna with convolutional neural networks for direction of arrival estimation in terahertz communications, *IEEE Transactions on Terahertz Science and Technology*, Early access, doi: 10.1109/TTHZ.2024.3358735.

Chapter 7 (Summary and outlook): concludes this thesis and provides an outlook for future developments based on the proposed terahertz planar antennas and lenses.

Chapter 2

Terahertz resonant-tunneling diode with series-fed patch array antenna

RESONANT-tunneling diodes (RTDs) are promising electronic sources for terahertz waves. A recently proposed slot-based RTD simplifies the fabrication process by removing the metal-insulator-metal (MIM) capacitor, which is used for DC separation, and introducing an etch stopper layer for simple air bridge formation. The simplified RTD structure, however, exhibits an unexpected large tilt angle in the main lobe of its radiation pattern due to the coupling between the slot antenna and the bias pads. This chapter presents a series-fed patch array design that exploits the biasing structure and directs leakage surface waves to the broadside direction. The simulation result shows that the main lobe is along the broadside, with a maximum directivity over 12 dBi and a 3-dB bandwidth around 20%. The radiation efficiency is improved from 22% to 28% at 275 GHz. An experimental validation with a bullet lens indicates that the RTD device with a series-fed patch array antenna has a narrower beamwidth and a sidelobe level much lower compared to the original RTD.

2.1 Introduction

Resonant-tunneling diodes (RTDs) are promising candidates for solid-state electronic sources. An oscillation frequency of 1.98 THz has been reported with an RTD based upon a reduction in the conduction loss (Izumi *et al.*, 2017). That work has held a record for the highest fundamental oscillation frequency for single-component electronic sources under room temperature. Meanwhile, RTDs with novel epitaxial structures (Cimbri *et al.*, 2022a) or with an integrated rectangular cavity (Kobayashi *et al.*, 2020; Han *et al.*, 2021) were proposed to increase the output power. A recent report from Canon Inc. presented a 6×6 RTD array configuration with patch antennas, to obtain over 10 mW output power at 450 GHz (Koyama *et al.*, 2022). Such a compact, low-power consumption semiconductor-based source is suitable for various sensing applications such as three-dimensional imaging (Dobroiu *et al.*, 2022) and radar systems (Konno *et al.*, 2021; Dobroiu *et al.*, 2020). Moreover, the non-linearity that occurs in the negative differential conductance (NDC) region can be exploited for RTD operation as detector, with a much higher sensitivity than a standard Schottky barrier diode (Arzi *et al.*, 2019; Cimbri *et al.*, 2022b). An example of 8K video transmission by using RTD as a coherent detector was demonstrated in (Webber *et al.*, 2021). Recently, efficient coupling between an RTD transceiver chip and a substrateless waveguide has been developed (Yu *et al.*, 2022; Headland *et al.*, 2023), which is a critical step toward integrated communications systems.

Despite the above promising benefits of the RTD, there is one general concern with RTD fabrication: the complex lithography process. A three-dimensional integration for conventional RTDs requires at least four exposure and three evaporation processes (Orihashi *et al.*, 2005). Considering necessary coating, surface contamination removal, and the lift-off process, the overall fabrication is complicated and time-consuming. A recently proposed simplified RTD structure removed the metal-insulator-metal (MIM) capacitor, which is used for DC isolation in conventional RTDs (Mai *et al.*, 2020). This planar structure therefore tremendously simplifies the overall fabrication process, which requires one electron beam exposure, one photolithography exposure, and one evaporation process. The newly introduced etch stopper layer also allowed easier air bridge formation (Mai *et al.*, 2020). This simplified structure reduces the fabrication duration by around 75%. As such, it shows considerable advantage in the laboratory environment and particularly suits future array-level expansion. Subsequent research indicated that the oscillation frequency can be increased by an integrated split ring resonator (SRR) (Yu *et al.*, 2021) and the output power can be improved by a backside-coupled

rectangular cavity (Fujikata *et al.*, 2021) or an off-set fed slot antenna Mai *et al.* (2022). Nevertheless, the radiation performance of this type of RTD configuration has not been thoroughly investigated. The strong conductive coupling between the bias pads and the slot antenna results in a large bidirectional beam tilt. This non-ideal radiation pattern is a general concern for RTDs coupled with a slot antenna and other terahertz sources and detectors that connect to bias lines. It compromises the overall efficiency and sets a great challenge to the implementation of the large-scale array (Koyama *et al.*, 2022; Campo *et al.*, 2020) and future flat lens systems (Brincker *et al.*, 2016; Pisano *et al.*, 2020).

In this chapter, a series-fed patch array is applied to an RTD working at around 275 GHz to significantly improve the radiation performance. Series-fed patch array antennas, which have been well-developed in the microwave (Nguyen-Trong *et al.*, 2022) and millimeter-wave frequency bands (Khalily *et al.*, 2016), essentially radiate electromagnetic power gradually along a transmission line. In order to mitigate the aforementioned strong coupling between bias circuit and the slot antenna, the connection strips are first extended to exacerbate the surface wave behavior. Then the series-fed patch array is utilized to direct the surface wave radiation to the broadside direction, i.e., the $+z$ direction, orthogonal to the slot plane. A detailed analysis of the effect of the bias lines and the design of the series-fed patch array is provided in Section 2.2. The proposed RTD structure is then compared with a conventional RTD device and evaluated with a bullet lens. The design process and simulation results will be demonstrated in Section 2.3. The measurement setup and experimental results will be included in Section 2.4, followed by a conclusion of this chapter.

2.2 Design and analysis

2.2.1 RTD characteristics

For most conventional implementations, the lower electrode of the RTD is located on one side of the slot antenna and the upper electrode is connected to the other side through a MIM capacitor. Essentially this capacitor behaves as a high-pass filter that isolates the DC bias but completes the terahertz oscillation circuit (Orihashi *et al.*, 2005). The recently proposed planar RTD removes the need for a MIM capacitor, as shown in Fig. 2.1(a), and therefore significantly simplifies the fabrication process (Mai *et al.*, 2020). The current-voltage (I-V) characteristic of the RTD exhibits a NDC region, where the current decreases when a bias voltage is applied. This NDC region compensates

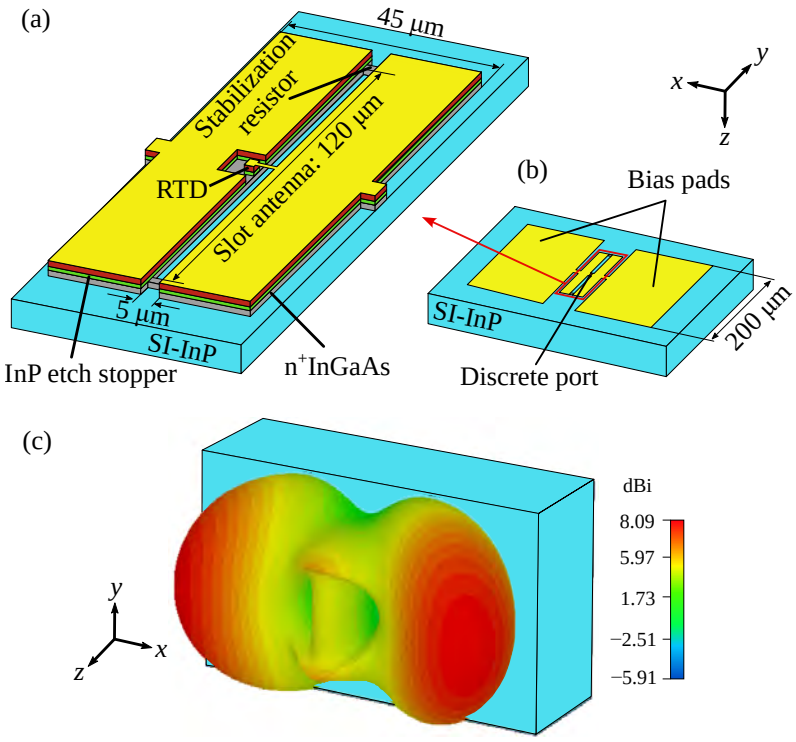

Figure 2.1. Simplified RTD structure without the MIM capacitor. (a) RTD schematic. The slot antenna has a length of 120 µm and a width of 45 µm to operate at around 275 GHz. The RTD is placed on one side at the slot center. The NDC characteristic of the RTD counteracts the antenna losses and enhances the terahertz oscillation. (b) RTD model under standard bias pads condition. The slot antenna is connected with two bias pads, where the bias voltage is applied. The bias pad size is 200×200 µm^2. For simplicity the RTD excitation is represented by a discrete port located at the center of the slot antenna in simulations. (c) Simulated 3-D radiation pattern of the RTD structure at 275 GHz.

the antenna losses and becomes a gain for terahertz oscillation. Unlike conventional RTD structures, n$^+$InGaAs stabilization resistors are embedded on the sides of the slot antenna. Consequently, the conductance of the slot antenna can be expressed as (Mai *et al.*, 2020):

$$G = \frac{R_s}{R_s^2 + \omega^2 L_{slot}^2} + G_{rad}, \tag{2.1}$$

where R_s is the stabilization resistance, L_{slot} is the slot antenna inductance, and G_{rad} is the antenna radiation conductance. Since the impedance of L_{slot} is large at terahertz frequencies, the overall antenna conductance is small enough to be compensated by the negative conductance from the RTD. At low frequencies, the impedance of L_{slot} becomes much smaller, resulting in a large antenna conductance to suppress the parasitic

oscillation. Detailed characteristics and a circuit model analysis can be found in Mai *et al.* (2020, 2022).

In this chapter, the radiation performance of such a simplified RTD structure in connection with the necessary bias pads is investigated. The RTD model is simulated in CST Microwave Studio, assuming no reflections from the semi-insulating (SI) indium phosphide (InP) substrate and a discrete port is used to represent the RTD excitation, as shown in Fig. 2.1(b). This RTD configuration, however, exhibits a symmetrical dual-beam radiation pattern, with a large tilt angle from the broadside direction, as illustrated in a 3-D representation in Fig. 2.1(c). In order to understand the undesired radiation performance, three different bias lines conditions are analyzed and compared. The first condition removes the bias pads and is merely composed of the fundamental slot antenna, in essence the isolated structure of Fig. 2.1(a). The standard bias pads condition of Fig. 2.1(b) follows the previously mentioned structure, where the distance between the bias pad and the slot antenna is 10 µm. Figure 2.2 shows the extended bias lines condition, where the connection strips are extended to around 600 µm to exacerbate the surface waves travelling along the lines. The effects of these three conditions on the radiation pattern, broadside directivity and radiation efficiency are summarized in Fig. 2.3.

The case of the RTD without bias lines (black dashed curves) reveals the envelope of the radiation. Since the RTD source is placed at an interface between an InP substrate and free-space, the pattern has specific characteristics with zeros occurring at a critical angle of 16° in the *E*-plane and maxima occurring at another critical angle of 17° in

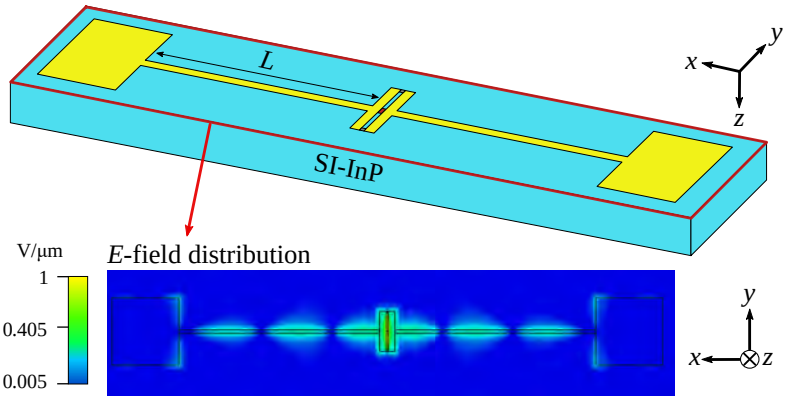

Figure 2.2. Schematic of RTD structure under extended bias lines condition. The instantaneous *E*-field distribution indicates that a surface wave is propagating along the bias in the $\pm x$ directions and radiating towards the InP substrate ($+z$-direction).

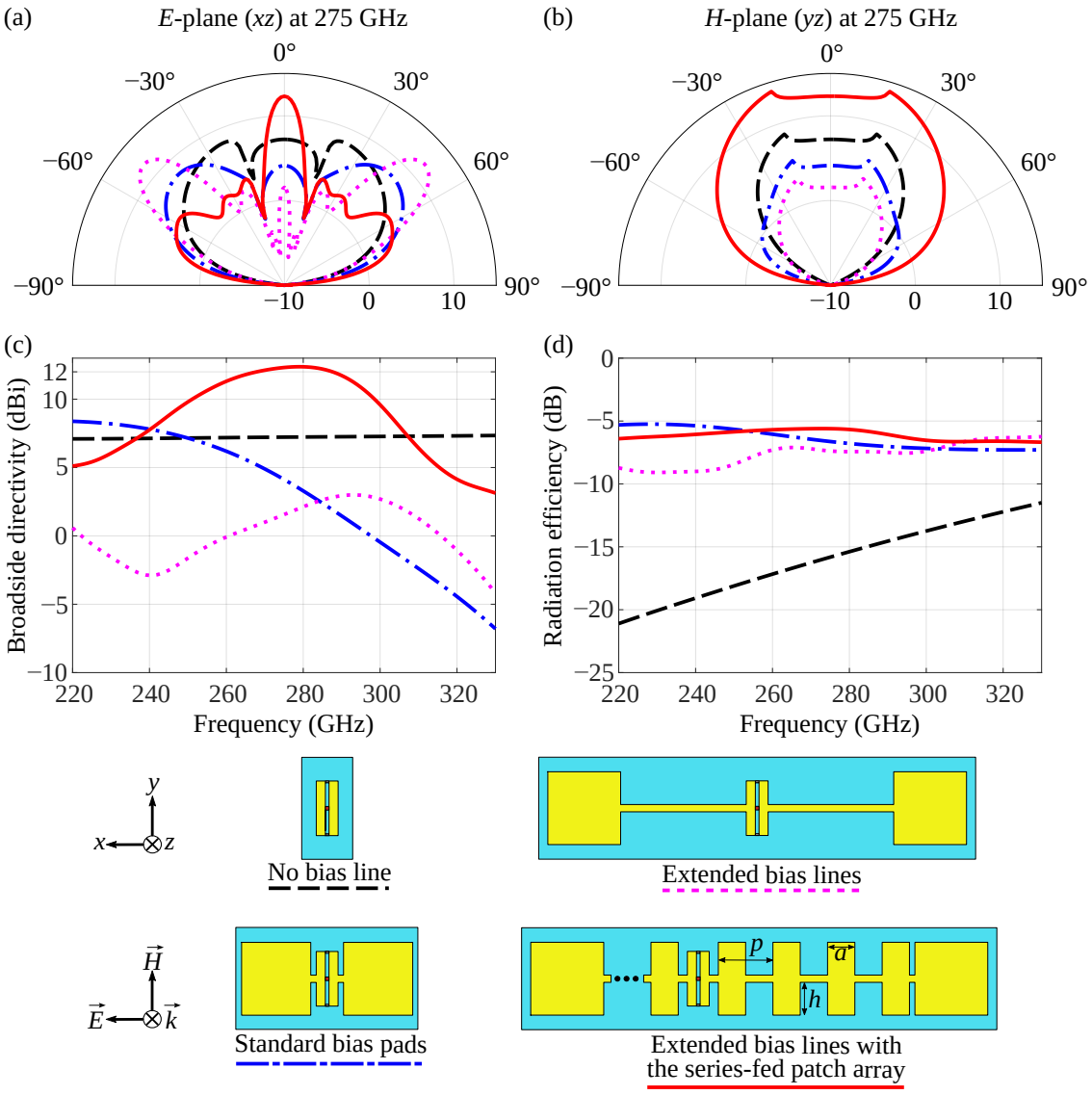

Figure 2.3. Comparison of RTD structures. These structures include no bias line condition (black dashed curves), standard bias pads condition (blue dashed-dotted curves), extended bias lines condition (purple dotted curves), and extended bias lines with a series-fed patch array (red solid curves). (a, b) Radiation pattern at 275 GHz in the *E*-plane and *H*-plane. (c, d) Broadside directivity and radiation efficiency over the WR-3 frequency band from 220–330 GHz.

the *H*-plane. These characteristics agree with the classical theory of planar antennas on a dielectric/air interface (Brewitt Taylor *et al.*, 1981). The slot antenna alone has an acceptable radiation pattern and the broadside directivity remains almost constant at 6.5 dBi over the WR-3 frequency band. Considering the stabilization resistor as the most lossy RTD component, ideally the current density around the resistor area should be as low as possible. However, since the stabilization resistors are located where the current is maximum in this case, the ohmic loss is high and the device exhibits a limited

radiation efficiency. The standard bias pads condition (blue dashed-dotted curves), as previously mentioned, has a large symmetrical main lobe tilt in the *E*-plane, with a deviation from the broadside direction by 44°. This radiation pattern results from the multiplication of two effects: a pattern from coupling with the bias pads and the previously mentioned pattern of a source at an interface. The zeros and maxima in the *E*-plane and *H*-plane remain at 16° and 17°, respectively. Due to the strong coupling between the bias pad and the slot antenna, the main lobe at broadside is suppressed by the leaky-wave behavior and the sidelobes are expressed bidirectionally. The broadside directivity remains low and is steadily decreasing over the WR-3 frequency band. However, it is notable that this radiation behavior of the bias pads channels the energy away from the lossy resistor and therefore the efficiency is improved compared to the no bias line condition. The simulated ohmic loss contributed by the stabilization resistors is reduced by around 40% from the previous slot-only case. The extended bias lines condition (purple dotted curves) is then introduced to enhance the surface waves on the bias lines. This surface wave also radiates as fast wave towards the InP substrate, which leads to a further expressed main lobe tilt at 49° while the broadside directivity remains low. Similarly, the zeros and maxima of the envelope pattern (antenna at interface) remain at the same angular positions. Nevertheless, it is observed that by extending bias lines, the leaky-wave behavior becomes controllable, which will be described in the following section.

2.2.2 Series-fed patch array design

Theoretically, the leaky-wave behavior can be eliminated by placing an absorber or filter along the strip lines. For example, a bandpass filter based on split ring resonators (SRRs) (Horestani *et al.*, 2013), or a plasmonic absorber derived from spoof surface plasmon polaritons (SPPs) (Fernandez-Dominguez *et al.*, 2008), could be integrated onto the line to improve the beam quality (Li *et al.*, 2021). However, the efficiency will be compromised due to intentional power dissipation. Instead of confining and damping the leakage energy, here we introduce a more efficient solution to control the leaky-wave behavior with the aim of improving the radiation performance, noting that preliminary findings with simulation results have been previously reported in Li *et al.* (2021). As shown in Fig. 2.4(a), the series-fed patch array comprises four patch elements between the bias electrode and the slot antenna on each side. For simplicity the effective wavelength for the strip line and the patch are assumed to be the same. The period p

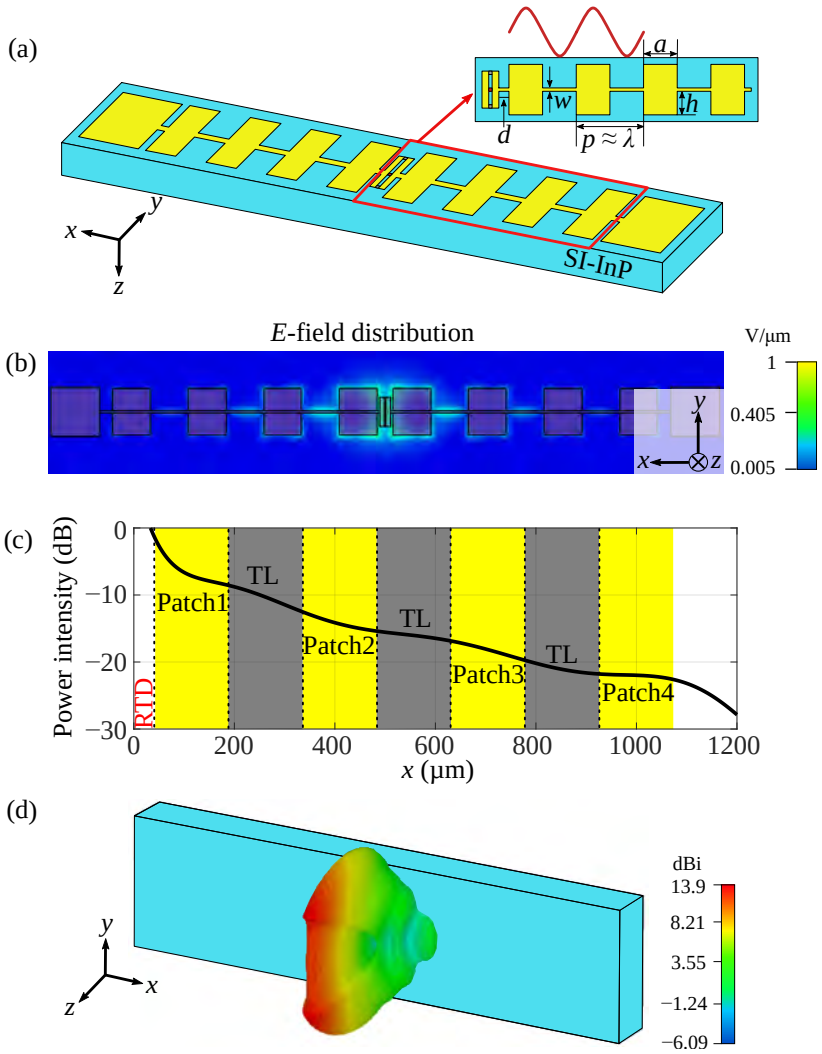

Figure 2.4. RTD with a series-fed patch array. (a) Structure schematic. Four patch elements are connected between the slot antenna and the bias pad on each side. The patch configuration is uniform. The patches are connected by strip lines of width w and the patch array is placed at d from the slot antenna. (b) E-field amplitude distribution. (c) Relative power intensity along the $+x$ direction, positioned at the middle point of the y-axis and on the surface of the metal. (d) 3-D simulated radiation pattern at 275 GHz.

and separation a are chosen as one effective wavelength and half effective wavelength, respectively, to ensure same phase output from the patches, following a classical series-fed patch array requirement. The effective wavelength follows a general microstrip line theory expression: $\lambda_{\text{eff}} = \lambda_0/\sqrt{(\epsilon_{\text{InP}}+1)/2}$, where the relative permittivity of the InP substrate $\epsilon_{\text{InP}} = 12.1$ (Asada and Suzuki, 2015). Since the InP substrate thickness of 200 μm is less than one wavelength, the material is assumed lossless for simplicity. In this case, the period p, strip separation a, and half patch width h are parametrically

optimized in CST Microwave Studio to 310 µm, 155 µm, and 90 µm, respectively. The strip width w is 10 µm and the initial patch array pairs are placed at $d = 10$ µm from the slot antenna for best phase matching. Since the patches are radiating into the substrate, the power level of the traveling waves decreases along the extended bias lines. Figure 2.4(b) shows the simulated maximum E-field distribution and the fourth patch sees a power level down to around -20 dB, as demonstrated in Fig. 2.4(c). These patch elements essentially exploit the traveling surface wave for in-phase feeding, leading to a planar wavefront generated along the connection strip and propagating to the broadside direction. When such a leaky-wave pattern is multiplied with the interface pattern, the broadside main lobe is reinforced and the sidelobes are lowered. The resulting 3-D radiation pattern is shown in Fig. 2.4(d). While it is possible to further increase the directivity by adding parasitic patch elements (Wi *et al.*, 2007) in the y-direction, the beam quality in the H-plane is currently sufficient to support the silicon lens as a secondary radiator.

It is worth mentioning that the series-fed patch array should not have a significant effect on the oscillation behaviors of the RTD. The susceptance of the RTD can be roughly expressed as ωC_{rtd}, where ω is the angular frequency and C_{rtd} is the RTD capacitance, which can be controlled by adjusting the RTD mesa area. The oscillation frequency is estimated by comparing the negative RTD susceptance $-\omega C_{\text{rtd}}$ and the antenna susceptance $\text{Im}(Y_{\text{ant}})$, i.e., the oscillation frequency is at the crossing point where their susceptances cancel. In this case, the crossing point is expected to occur at

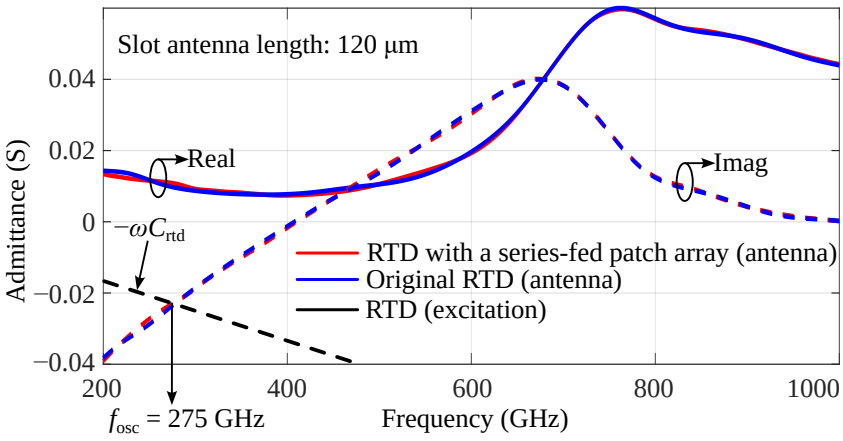

Figure 2.5. Comparison of Y-parameters simulated from the original RTD and RTD with a series-fed patch array. The oscillation frequency is at the crossing point with the negative susceptance of the RTD excitation, where the susceptances of the RTD and antenna cancel.

275 GHz. A detailed RTD model excited by a discrete face port, as shown in Fig. 2.1(a), is necessary to obtain accurate Y-parameters in CST simulations. As shown in Fig. 2.5, the original RTD and RTD with a series-fed patch array have almost identical Y-parameters, suggesting that the RTD oscillation frequency is purely determined by the slot antenna and not affected markedly by the series-fed patch array antenna. A simple explanation for the identical Y-parameters behavior is that the patch antenna arrays cause negligible reflections back to the RTD, hence the I-V characteristic of the antenna remains the same. A detailed radiation performance summary of the series-fed patch design has been included in Fig. 2.3, which clearly indicates that the main lobe is back at broadside in the E-plane, with a maximum directivity over 12 dBi, which is 8 dB higher than the original RTD structure. The sidelobes are at around 58° and about 8 dB lower than the broadside main lobe. The broadside directivity smoothly changes over the frequency and the 3-dB fractional bandwidth against the center frequency of 275 GHz is around 20%. The radiation efficiency, which is defined as the ratio of radiated power to accepted power, is improved from 22% to 28% at 275 GHz, since the same phase output leads to a more efficient coupling and the dissipation loss contributed by the stabilization resistors remains unchanged. It should be clarified that gold is represented with the Drude model (Lucyszyn, 2007) in simulation and the surface impedance is relatively small at low terahertz frequencies. As a result, the metal loss caused by the series-fed patch array is negligible. A simulation with a series-fed patch array made of perfect electric conductor (PEC) suggests a minor efficiency variation within 0.3 dB.

2.3 Bullet lens validation

The radiation performance of the RTD chip is not directly measurable due to the strong internal reflections inside the InP substrate, where the radiation gets trapped. Therefore, a silicon lens ($\epsilon_{\mathrm{Si}} = 11.68$) is mounted on the substrate side of the RTD chip to couple the field to free space, allowing experimental validation of the series-fed patch array design. A hyper-hemispherical lens is commonly used for a collimated output wavefront. Although the large aperture of such a lens can cover most of the radiation beamwidth from most devices, the beam quality of conventional RTD is less desirable due to multiple lobes (Asada and Suzuki, 2015). To clearly observe the effect of the RTD with a series-fed patch array, here we consider a bullet lens structure, with the cross-sectional view shown in Fig. 2.6(a). The bullet lens is basically composed of a hemisphere of radius R with a reduced aperture of diameter D, and a cylindrical base of

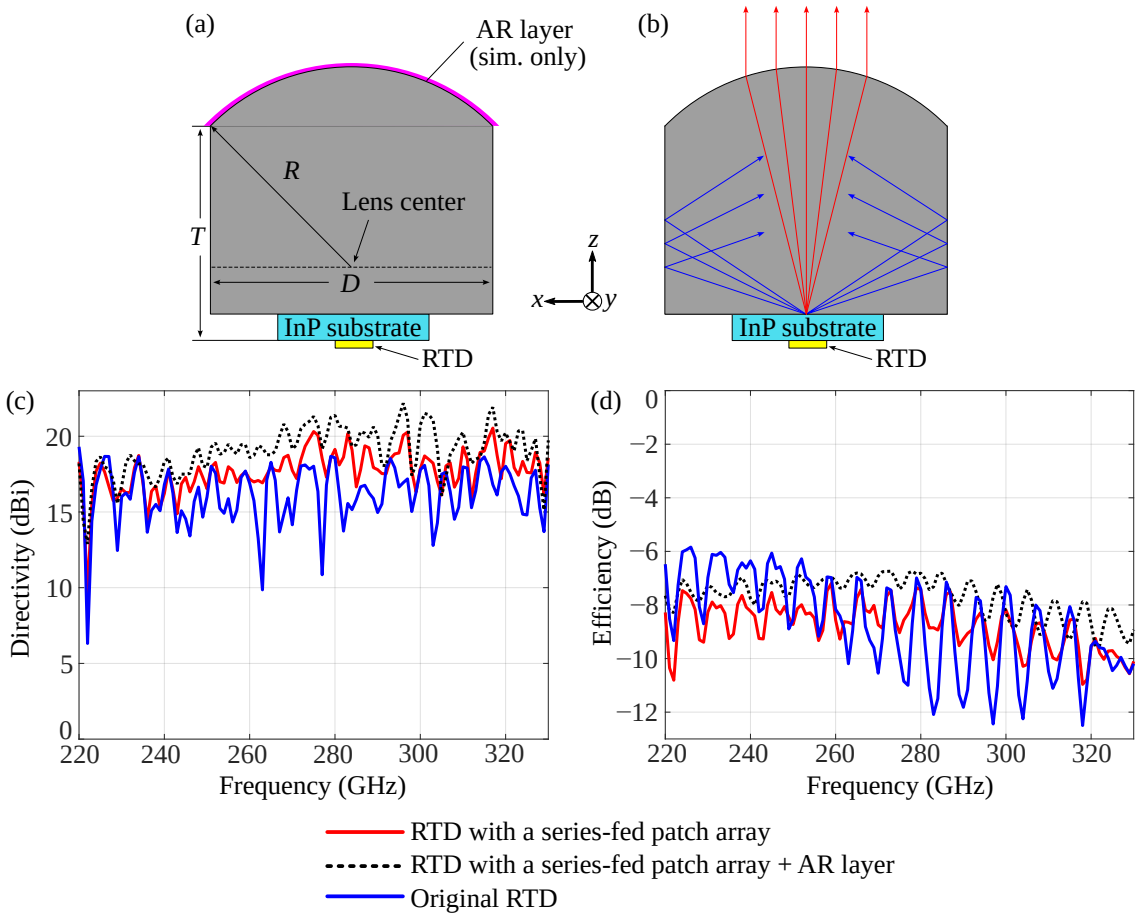

Figure 2.6. Bullet lens geometry and simulated RTD performance. (a) Cross-sectional view of the proposed bullet lens. The bullet lens is composed of a hemisphere of radius R with a reduced aperture of diameter D, and a cylindrical base of thickness T. Note that the thickness T includes the InP substrate thickness of 200 µm. (b) The reduced aperture results in strong internal reflections for the original RTD (blue), while the RTD with a series-fed patch array still operates well due to the improved radiation performance (red). (c, d) Simulated directivity and efficiency comparison for the original RTD and RTD with a series-fed patch array.

thickness T. They follow a general relation described in Asada and Suzuki (2015):

$$T = \frac{R}{\sqrt{\epsilon_r} - 1} + \sqrt{R^2 - (D/2)^2}. \tag{2.2}$$

It is worth noting that here T also includes the 200 µm thickness of the InP substrate. Since InP ($\epsilon_{InP} = 12.1$) and silicon ($\epsilon_{Si} = 11.68$) have very similar relative permittivity values, for simplicity the InP substrate is considered as a part of the cylindrical base. For packaging reasons, the bullet lens is designed as $R = 3$ mm and $D = 4.8$ mm. Therefore, the cylindrical base is initially chosen as $T \approx 3$ mm. T is then parametrically optimized

in CST Microwave Studio to 2.8 mm to provide highest directivity at 275 GHz. The simulated broadside directivity of the bullet lens is shown in Fig. 2.6(c). For the RTD with a series-fed patch array, the radiation patterns appear to be highly directive over the frequency band, with a maximum directivity over 20 dBi at 275 GHz. Some fluctuations are observed, which can be explained by the reflections at the top silicon-air interface and the limited aperture size. An anti-reflection (AR) layer is added on top of the silicon lens in simulation, which can generate an 1 dB increase overall the WR-3 band. The AR material has a permittivity of the geometric mean of surrounding materials: $\epsilon_{\mathrm{AR}} = \sqrt{\epsilon_{\mathrm{Si}}\epsilon_{\mathrm{air}}}$ and thickness of a quarter effective wavelength at 275 GHz. However, for a simple and cost-effective fabrication process, the AR layer will not be included in the following discussion and experiment. A generally lower level of directivity is found for the original RTD, accompanied by some extremely strong fluctuations, e.g., the directivity even drops below 10 dB at 263 GHz. This is because the original RTD device has a large main lobe tilt, causing strong internal and multi-path reflections inside the bullet lens. In contrast, the RTD with a series-fed patch array exhibits weak fluctuations since the strong main lobe is in the broadside direction. A simple explanation by an illustrative ray-tracing diagram for the two RTDs can be found in Fig. 2.6(b). To further validate that the series-fed patch array improves the beam quality in a wide band, Fig. 2.7 includes the radiation patterns in the E-plane for both RTDs at four different frequencies. As expected, the original RTD generates strong sidelobes while a clear

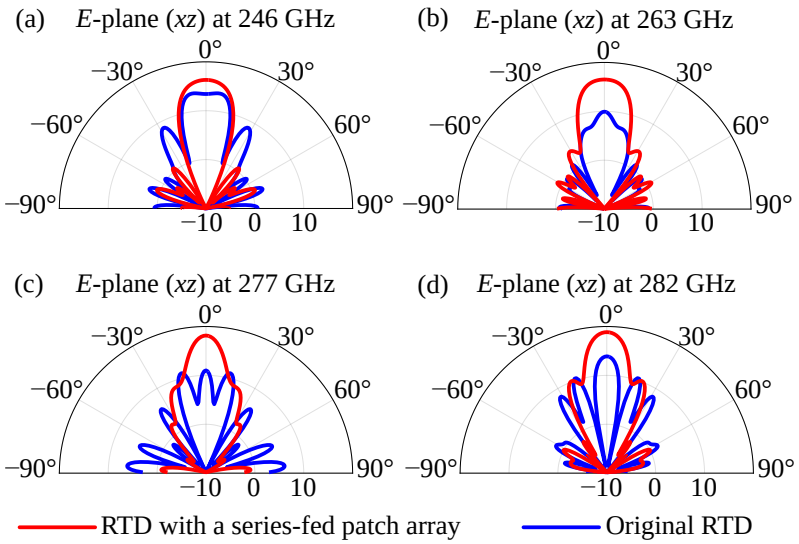

Figure 2.7. Comparison of simulated radiation patterns in the E-plane with the bullet lens: RTD with a series-fed patch array (red) and original RTD (blue). (a) 246 GHz. (b) 263 GHz. (c) 277 GHz. (d) 282 GHz.

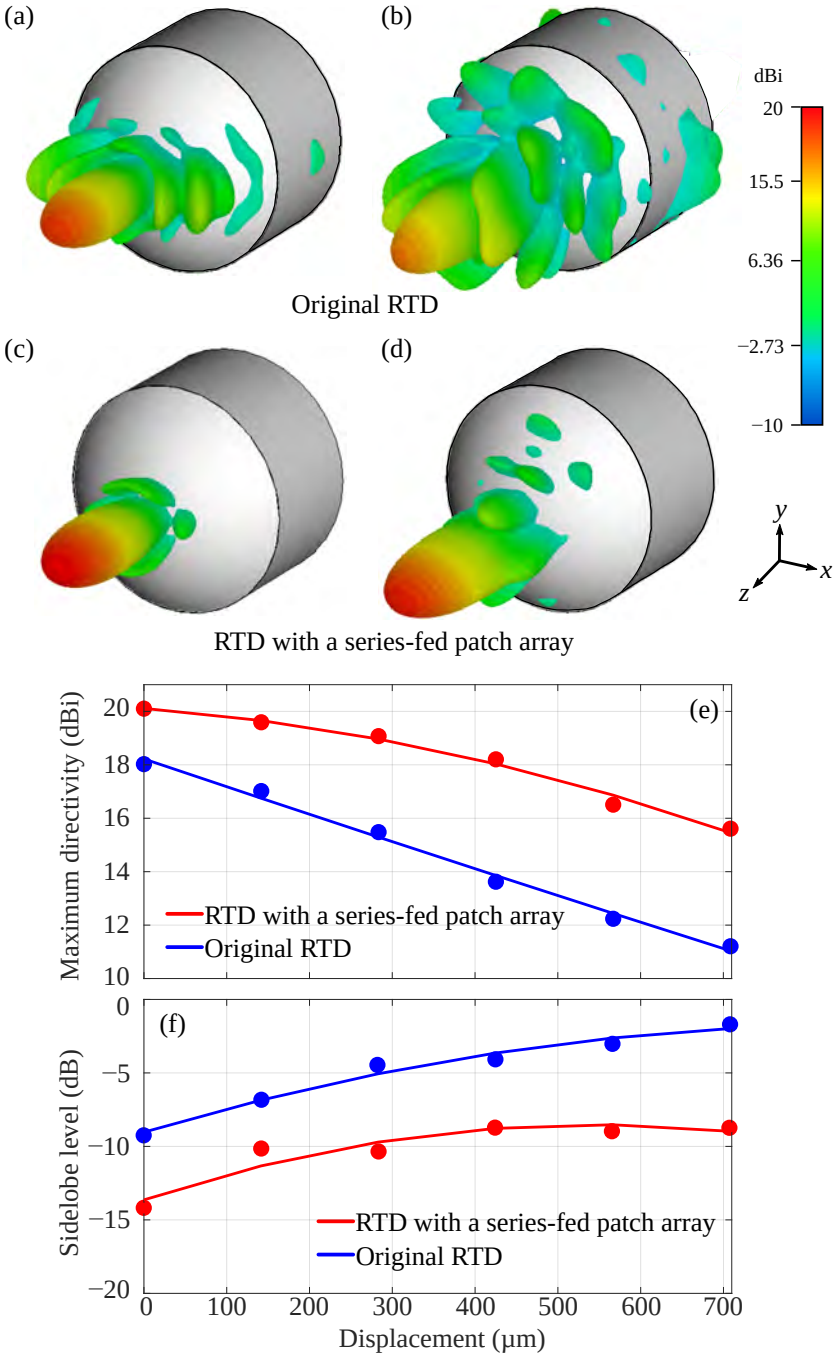

Figure 2.8. Simulated radiation performance at 275 GHz. (a, c) 3-D radiation patterns: Original RTD and RTD with a series-fed patch array. (b, d) 3-D radiation patterns: Original RTD and RTD with a series-fed patch array. RTD chips are misaligned with the bullet lens by 200 μm in both the x- and y-directions. (e, f) Main lobe directivity and sidelobe level against the misalignment. The RTD chips are misaligned with the bullet lens in the diagonal direction up to around 700 μm.

main lobe can be found in the broadside direction for the RTD with a series-fed patch array. The simulated efficiency of the RTDs with a bullet lens is shown in Fig. 2.6(d).

Due to the aforementioned silicon-air interference and truncated aperture size, strong fluctuations are observed for both RTDs. The original RTD experiences a stronger level of fluctuation due to the multi-path reflections inside the bullet lens. Such fluctuations lead to difficulty in comparing the efficiency in measurement. Therefore, the remaining discussion will focus on the improvement on radiation patterns and only the measured power of the RTD with a series-fed patch array will be reported.

Another important advantage of the series-fed patch array is a better tolerance to misalignment between the lens and the RTD. It is costly to use accurate position equipment or the recently proposed transfer-substrate process (Kress *et al.*, 2022). Therefore, in most cases the RTD chip is manually placed on the silicon lens. The simulated 3-D radiation patterns for the two RTDs at 275 GHz are given in Fig. 2.8(a, c). They clearly indicate that the RTD with a series-fed patch array has a higher broadside directivity, with a reduced sidelobe level in the *E*-plane. To further investigate, the simulated 3-D radiation patterns at 275 GHz of the two RTDs misplaced by 200 µm in both the *x*- and *y*-directions are shown in Fig. 2.8(b, d). A clear main lobe can be found with the series-fed patch array, while strong multiple sidelobes can be observed for the original RTD. Meanwhile the main lobe of the proposed RTD antenna is 4 dB higher than the original RTD main lobe. This clearly demonstrates that in a misaligned configuration, it is much more convenient to find a stable main lobe and its direction for the RTD with a series-fed patch array. Figure 2.8(e, f) show the robustness against packaging deviation in simulation. Both RTD chips are shifted in the diagonal direction, and the resulting directivity curves as a function of misalignment suggest that the main lobe directivity of the original RTD falls much quicker than the RTD with a series-fed patch array. Similarly, the sidelobe level of the original RTD increases more quickly than the RTD with a series-fed patch array.

2.4 Fabrication and measurement

The epitaxial structure of the utilized RTD is shown in Fig. 2.9(a). The measured *I*-*V* characteristics of an RTD mesa area of 1.8 µm^2 is shown in Fig. 2.9(b), and the RTD parameters are estimated as follows: peak-to-valley current difference ΔI = 14.3 mA, peak-to-valley current ratio (PVCR) = 2.95, peak-to-valley voltage difference ΔV = 0.292 V, and RTD conductance $G_{\mathrm{RTD}} = -73.3$ mS. The RTD capacitance C_{RTD} is estimated as 9.9 fF from simulation. The RTD with a series-fed patch array antenna was fabricated

successfully. The microscope picture is shown in Fig. 2.10(a) and the SEM image of the RTD excitation is given in Fig. 2.10(c). To simplify the fabrication process, the same

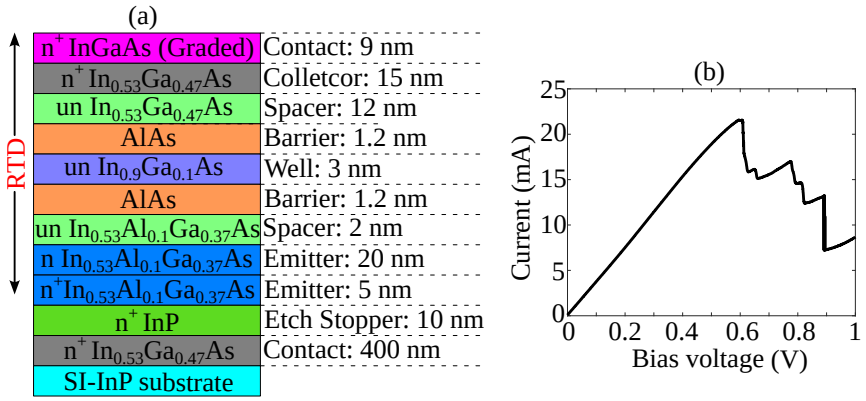

Figure 2.9. Employed RTD structure. (a) Epitaxial layer. (b) Measured I-V characteristic.

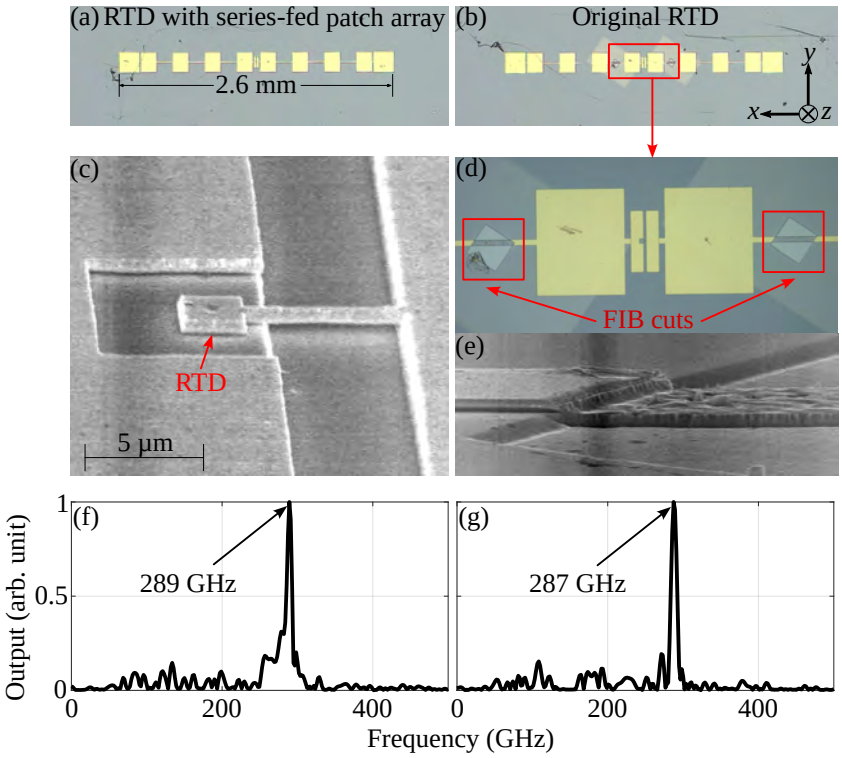

Figure 2.10. Fabricated RTD samples. (a, c) Microscope picture of the RTD with a series-fed patch array antenna and an SEM image of the RTD excitation. (b, d) Microscope picture of the fabricated original RTD device. The geometry is the same as (a) and focused ion-beam (FIB) process is applied to cut the bias lines. The bias voltage is applied at the first patch doubles. (e) SEM image of the edge of the bias line. The gold strip is removed and the InP substrate underneath is exposed. (f, g) Oscillation spectrum: RTD with a series-fed patch array and original RTD oscillates at 289 GHz and 287 GHz, respectively.

geometry of the RTD with a series-fed patch is used for the original RTD. Focused ion beam (FIB) lithography, which is an inherently destructive process, is used to cut the connection strips between the first and second pairs of patch elements. The first pair of patches becomes the bias pads, where the bias voltage is applied. By doing so the RTD with a series-fed patch array is converted back to the original RTD. The microscope pictures of the original RTD are shown in Fig. 2.10(b, d) and the SEM image of the FIB cutting is shown in Fig. 2.10(e), suggesting that the bias lines are properly cut. The remaining bridge is an undercut part of the substrate. A simulation confirms that the effect of parasitic coupling between the detached patches is negligible. To measure the oscillation spectrum, the RTDs chip is placed on a large hemispherical silicon lens with a diameter of 30 mm. The output radiation is collimated by an off-axis parabolic mirror and detected by a Helium-cooled bolometer connected with a lock-in amplifier. The oscillation is extracted by a Fourier transform infrared (FTIR) spectrometer. As shown in Fig. 2.10(f, g), the RTD with a series-fed patch array and the original RTD oscillate at 289 GHz and 287 GHz, respectively. The measured oscillation frequencies are nearly identical and close to the anticipated value of 275 GHz. This validates that the oscillation behavior of the RTD is not affected markedly by the series-fed patch array antenna. A slightly broader spectrum can be observed from the RTD with a series-fed patch array, potentially caused by a relatively small detected power. The detailed RTD fabrication process has been previously reported in Mai *et al.* (2020).

To measure the output power, the RTD is packaged with a bullet lens on a PCB and the radiation is captured by the power meter with a horn antenna (Erickson PM5). Estimated from the power ratio of transmission at the silicon-air interface and the duty-cycle, the measured output power of the RTD with a series-fed patch array antenna is around 28 µW. The experiment setup and its schematic for the radiation pattern measurement are shown in Fig. 2.11. The packaged RTD is placed on the rotator, which is set to an angular resolution of 1°. An iris is placed at distance d_1 from the lens. The surrounding effects are minimized due to line-of-sight propagation. The iris size d_{iris} is determined as 7 mm, so that the sidelobes are measurable compared to the noise, and the angular resolution of 1° can be attained simultaneously. The Helium-cooled bolometer is placed at d_2 from the iris, to collect the far-field radiation from the RTD. The distance d_1 and d_2 are set as 150 mm and 100 mm, respectively. The total distance of 250 mm is much larger than the far-field distance of around 50 mm. The bolometer is connected to a lock-in amplifier (NF LI5660) to extract the signal from the noisy surrounding. This lock-in amplifier is set for a time constant of 200 ms and a sensitivity of 2 mV. A precise

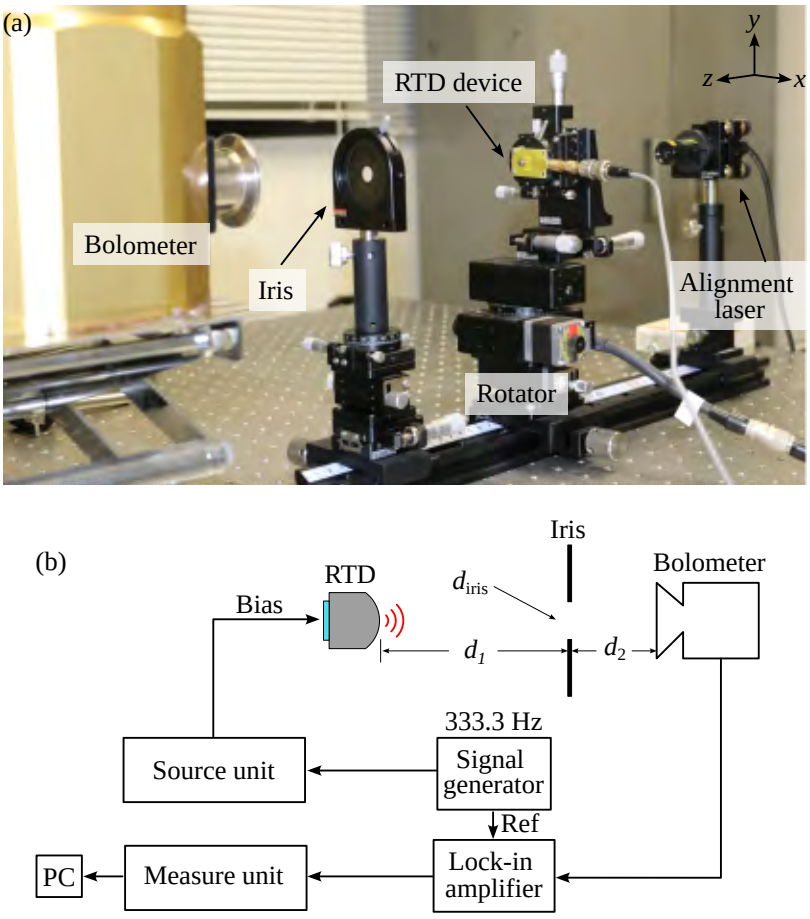

Figure 2.11. Measurement setup. (a) The bullet lens is placed on the rotator with an angular resolution of 1°. A signal from the RTD is transmitted through an iris and is detected by the bolometer. The laser placed behind the bullet lens is used for device alignment. (b) Measurement schematic.

source/measurement unit (Agilent B2902A) is used to provide the RTD biasing with a duty cycle of 5% and measure the output from the lock-in amplifier. An external signal generator (Tektronix AFG1062) provides a reference signal of 333.3 Hz for the source unit and the lock-in amplifier.

The measurement results of both RTDs with the bullet lens are shown in Fig. 2.12. It is clear that the RTD with a series-fed patch array provides high-directivity patterns in both *E*- and *H*-planes, i.e., *xz*- and *yz*- planes. As shown in Fig. 11(a, b), the 3-dB beamwidth amounts to an angle of 13° in the *E*-plane and 10° in the *H*-plane. To ease comparison with the original RTD patterns, the 10-dB beamwidth is within an angle of 20° in the *E*-plane and 14° in the *H*-plane. On the contrary, the original RTD has a much larger beamwidth and a higher sidelobe level. As can be seen from Fig. 2.12(c, d), the 10-dB beamwidth is within an angle of 51° in the *E*-plane and 42° in the *H*-plane,

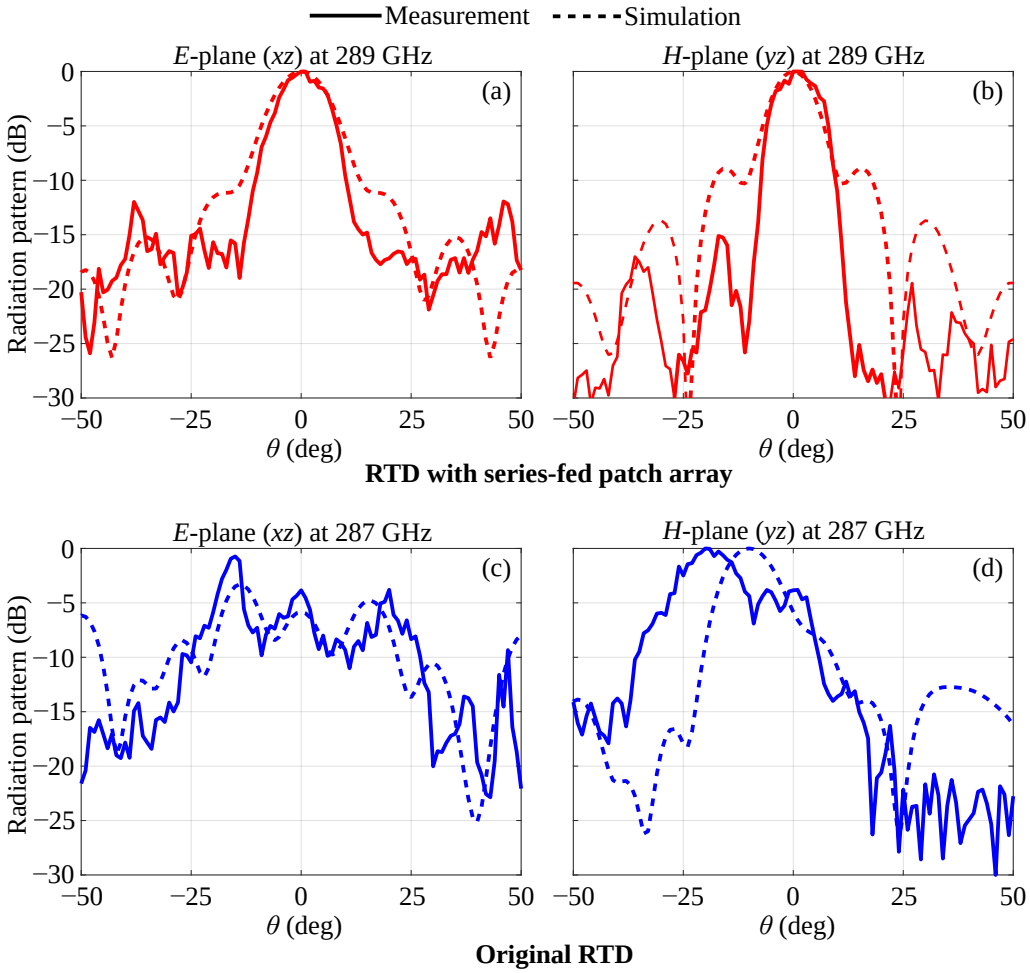

Figure 2.12. Measurement and simulation results. The patterns are normalized to their maximum values of the E- and H-planes. (a, b) Radiation pattern at 289 GHz for the RTD with series-fed patch array. (c, d) Radiation pattern at 287 GHz for the original RTD. The bullet lens is misplaced by 30 µm and 200 µm in the E-plane and H-plane in CST simulation to match the measured patterns.

and there is no clear main lobe found in the E-plane. For the original RTD case, the measurement is compared with a simulated RTD misaligned with the lens by 30 µm in the E-plane and 200 µm in the H-plane. It should be pointed out that, it is difficult to obtain perfectly matched simulation and measurement results. As previously discussed for Fig. 2.6(c), the bullet lens is without an AR layer and its aperture is small, so the patterns for both RTDs will significantly vary with frequency. A combined effect of strong internal reflections in the lens and misalignment makes it more difficult to obtain well-matched results particularly for the original RTD. Nevertheless, these comparisons are within an acceptable range and the overall pattern shapes are reasonably similar.

2.5 Conclusion

In this chapter, an RTD with an advanced antenna design to improve the radiation performance has been proposed. Compared with other notable antenna structures coupled with the RTD, as shown in Table 2.1, the proposed series-fed patch array antenna significantly improves the radiation performance. With a similar antenna area, the 3-dB beamwidth of our design is consistent with existing high-directivity RTD designs. The RTD characteristics and the effect of the bias lines have been thoroughly investigated. The overall radiation pattern can be considered as a multiplication of the pattern of a source at an interface and a leaky-wave pattern. While the envelope of the radiation pattern is determined by the slot antenna at the dielectric interface, the conductive coupling between the bias pad and the slot antenna reinforces the side lobes in the leaky-wave pattern, therefore leading to a large main lobe tilt. Instead of eliminating the leaky-wave behavior, a series-fed patch array is used to efficiently exploit the traveling wave and direct the leaky-wave pattern to the broadside. Simulation results show that the main lobe can be brought back to the broadside direction in the *E*-plane, with a maximum directivity over 12 dBi and 3-dB bandwidth of around 20%. The radiation efficiency theoretically increases from 22% to 28% at 275 GHz. The design is experimentally validated with a bullet lens. Comparison with the original RTD clearly suggests a much narrower beamwidth and a lower sidelobe level, combined with robustness to source-lens misalignment. Such a series-fed patch array antenna can be generally applicable to slot-antenna integrated RTD structures and other antenna-integrated sources connected to bias lines. Benefitting from its simple structure, the

Table 2.1. Comparison on radiation performance of RTD integrated with antenna. HPBW: half power beamwidth. *Estimated from the radiation pattern plot.

Design	Frequency (GHz)	Number of RTDs	Integrated antenna	Radiator	Configuration	Size (λ^2)	HPBW (*E*-plane)	HPBW (*H*-plane)
Koyama *et al.* (2022)	450	2	Patch	N.A.	6×6 array	20	13°	13°
Iwamatsu *et al.* (2021)	354	2	Slot ring	Silicon lens	Single	154	8°	8°
Kasagi *et al.* (2019)	1000	1	Slot	Dipole array	10×10 array	29	*40°	*90°
This work	289	1	Slot with patch array	Silicon lens	Single	18	13°	10°

concept can be easily scaled for higher oscillation frequencies, where such non-ideal radiation performance is more likely since the size of bias pads becomes much larger than the wavelength. The benefits in the radiation performance in light of reduced antenna efficiency at such a high frequency remains to be investigated. It can be anticipated that this design can contribute to a wide range of future investigations, including large-scale arrays, flat lens designs, and other potential planar structures based on the extended bias line platform.

Chapter 3

Terahertz resonant-tunneling diode with log-spiral antenna

RESONANT-tunneling diodes (RTDs) with extended bias line connections allow surface wave propagation. In Chapter 2, a series-fed patch array antenna has been employed to improve the radiation performance of such devices. The extended bias line structure can be further utilized as a platform for different applications. In this chapter, the bias lines are formed into a log-spiral configuration to provide circularly polarized (CP) radiation. Full-wave simulation suggests that the structure can radiate with an axial ratio generally lower than 2 dB and a radiation efficiency above -5 dB from 400–600 GHz. The radiation efficiency is improved from the original dipole design due to a reduction in ohmic losses imposed by stabilization resistors that are now located further from the RTD. A broadside directivity of around 25 dBiC can be achieved at 500 GHz when the spiral structure is used to feed a hyper-hemispherical silicon lens.

3.1 Introduction

The limited output power of terahertz sources remains a challenge in the practical implementation of terahertz wireless communications. Despite numerous demonstrations of terahertz communications with RTDs, the achieved data rates typically fall below 50 Gb/s due to limited signal-to-noise ratio (Cimbri *et al.*, 2022b). In the pursuit of higher output power, the configuration of RTD arrays with coherent power combination has gained popularity (Kasagi *et al.*, 2019; Koyama *et al.*, 2022). Recent studies have explored operation modes for array oscillators (Meng *et al.*, 2023), with a particular focus on the odd-mode operation that supported a structure-simplified RTD array, leading to an enhanced output power of approximately 0.77 mW at 530 GHz (Mai *et al.*, 2023). In terms of single oscillator power enhancement, considerable attention has been directed towards cavity-coupled RTDs in recent years (Han *et al.*, 2022, 2023). Different types of resonant cavity, such as rectangular or cylindrical cavities, exhibit low loss and low inductance characteristics, leading to an increased RTD mesa area and consequently, an enhanced output power. A novel rectangular-cavity coupled RTD with a heat dissipation structure has been proposed as an advancement, replacing the low thermal conductivity n^+InGaAs with high thermal conductivity n^+InP (Fujikata *et al.*, 2022). This replacement allows for a doubling of the RTD mesa area without heat-induced destruction, thereby further enhancing output power (Tanaka *et al.*, 2023). However, a common issue with this type of cavity-coupled RTDs is that the cavity also functions as a radiator, equivalently acting as a dipole. The dipole length is primarily determined by the oscillation circuit, which may not be optimal for radiation. This suboptimal configuration can result in reduced radiation efficiency, posing a challenge to be addressed.

In this Chapter, a log-spiral antenna is applied to the cavity-coupled RTD to generate efficient circularly polarized (CP) radiation from 400-600 GHz. Different from its role as a radiator in previous configurations (Tanaka *et al.*, 2023), the cavity purely serves as an oscillation circuit. Hence, the antenna part can be separately designed for optimal radiation performance. As previously discussed in Chapter 2, the surface wave can propagate along the extended bias lines. In this specific application, these extended bias lines are configured to form a log-spiral radiator excited by the cavity-coupled RTD. The propagation of the surface wave along this log-spiral configuration results in the desired CP radiation characteristics. Such CP radiation facilitates easier polarization alignment between transceivers and enhances spectral efficiency for terahertz communications. While a similar spiral bias connection structure has been reported in Clochiatti *et al.*

(2021), it was mainly used as a detector in a different RTD design and the radiation characteristics were not thoroughly investigated. Importantly, due to proximity, the stabilization resistors necessary for RTD operation imposed considerable loss in that early CP design (Arzi *et al.*, 2018; Clochiatti *et al.*, 2021). Section 3.2 provides a comprehensive analysis of the design, and the simulation results are provided in Section 3.3. A summary is given in Section 3.4.

3.2 Design and analysis

The schematic of the cavity-coupled RTD is illustrated in Fig. 3.1(a). It features a rectangular resonator cavity integrated with a large line-shaped RTD mesa area to achieve

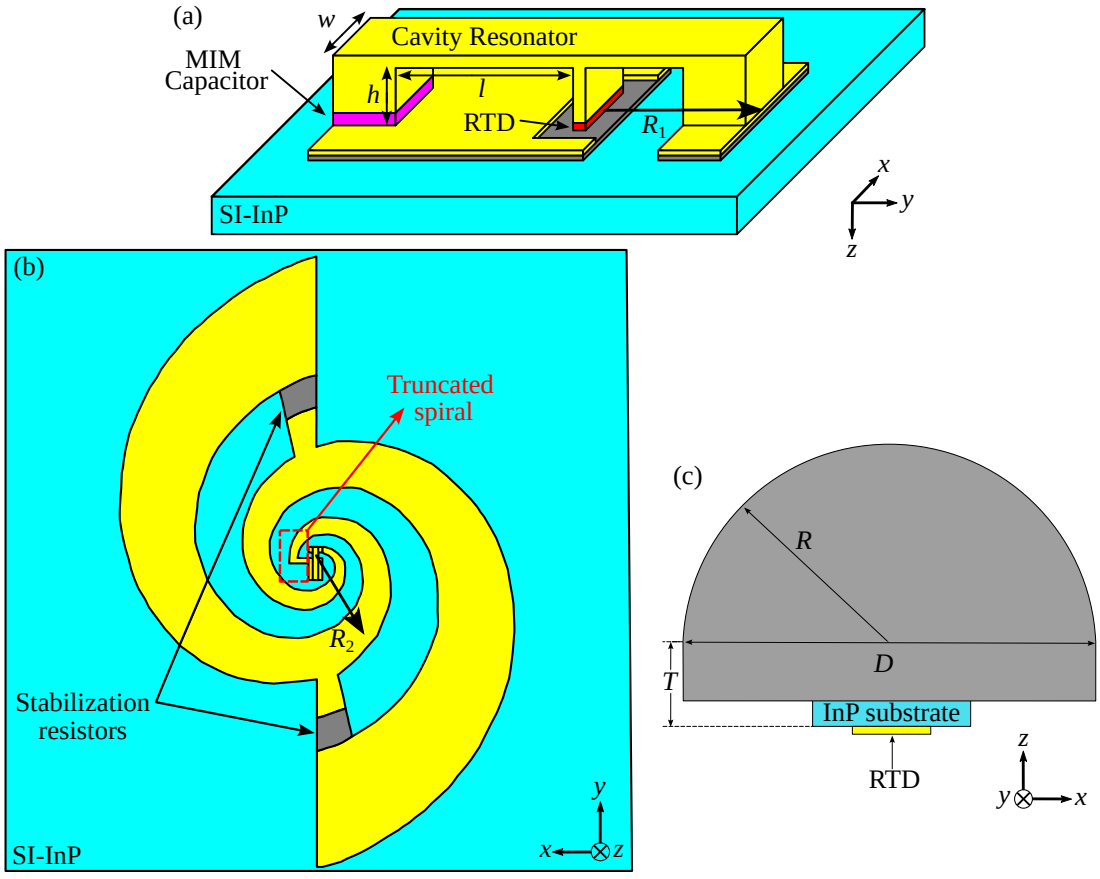

Figure 3.1. CP RTD structure. (a) Cavity-resonator-coupled RTD schematic. The rectangular cavity with length l, width w and height h helps improve the output power. R_1 refers to the inner radius of the log-spiral antenna intended for radiation. (b) Cavity-coupled RTD with spiral bias connections. R_2 refers to the outer radius of the log-spiral antenna. (c) RTD with a hyper-hemispherical silicon lens to collimate the output wavefront. The silicon lens has a diameter of $D = 2R$ and an extended thickness of T, which includes the InP substrate thickness.

high output power. A metal-insulator-metal (MIM) capacitor, separating the top and bottom electrodes, serves to isolate the DC bias. Due to its low RF impedance, the MIM capacitor also forms part of the cavity wall. While the cavity dimensions remain unchanged from Fujikata *et al.* (2022), the extended metal area is removed to suppress direct radiation, since the cavity no longer serves as a radiator. This allows to accommodate an inner radius R_1 of the logarithmic spiral antenna small enough to support the highest operating frequency point $f_{\text{high}} = c/(2\pi R_1\sqrt{(\epsilon_{\text{InP}}+1)/2})$, where the relative permittivity of the indium phosphide (InP) substrate $\epsilon_{\text{InP}} = 12.1$. A planar view of the CP RTD structure is presented in Fig. 3.1(b). The cavity-coupled RTD is connected to the logarithmic spiral bias connections, where the outer radius R_2 of the spiral antenna supports the lowest operating frequency $f_{\text{low}} = c/(2\pi R_2\sqrt{(\epsilon_{\text{InP}}+1)/2})$. The design generally follows the principle of classical spiral antenna theory (Grossman *et al.*, 1991). Notably, one spiral arm is truncated earlier on the inner side and connected to the cavity-coupled RTD at the mesa position. This design follows the original linearly polarized design (Fujikata *et al.*, 2022), contributing to improved efficiency compared to a normal spiral. While different types of spiral antennas such as an Archimedean spiral or a square spiral are available, the choice of a logarithmic spiral antenna is favored for its increasing width, which is advantageous for biasing. The width of each spiral arm at its end is approximately 300 µm, facilitating the wire bonding process and eliminating the need for additional bias pads in this design. To suppress the undesirable low-frequency oscillations, stabilization resistors made of n^+InP with a conductivity of 306000 S/m are designed to be around 100×100 µm^2, so that the total positive conductance compensates for the negative differential conductance (NDC) from the RTD. To minimize ohmic loss at terahertz frequencies and heat generation near the RTD, these resistors are positioned far away from the outer radius R_2 of the logarithmic spiral antenna. This arrangement ensures that the stabilization resistors have a negligible impact on electromagnetic radiation, and ohmic loss is minimized. To prevent strong internal reflections within the InP substrate, a hyper-hemispherical silicon lens is mounted on the substrate side of the RTD to couple the output power to free space, as depicted in Fig. 3.1(c).

3.3 Simulation results

The CP RTD is simulated using CST Microwave Studio, with the assumption of no reflections from the semi-insulating (SI) InP substrate. A discrete face port is employed

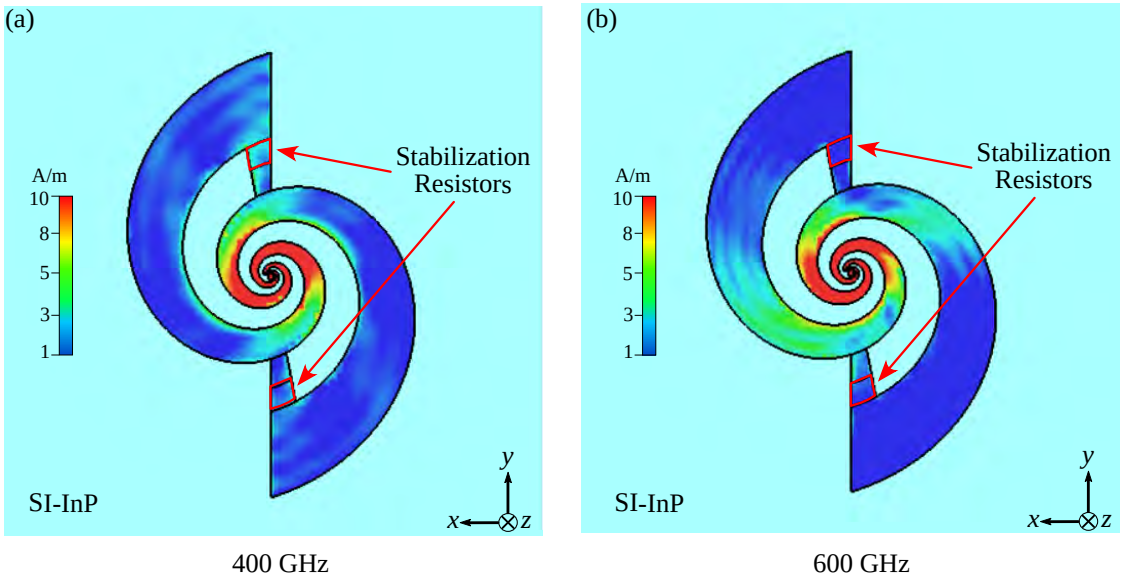

Figure 3.2. Simulated current amplitude distributions along the log-spiral antenna surface. (a) 400 GHz. (b) 600 GHz. The same colormap applies to both plots.

to represent the RTD excitation. Figure 3.2 illustrates the simulated current amplitude distributions along the log-spiral antenna. At the lowest operating frequency of 400 GHz, the current flows along the spiral up to the outer radius area. As anticipated, the current flow through the stabilization resistors is nearly negligible, effectively minimizing ohmic loss. At the highest operating frequency of 600 GHz, the current flow remains close to the inner radius area. It is worth noting that the applied log-spiral

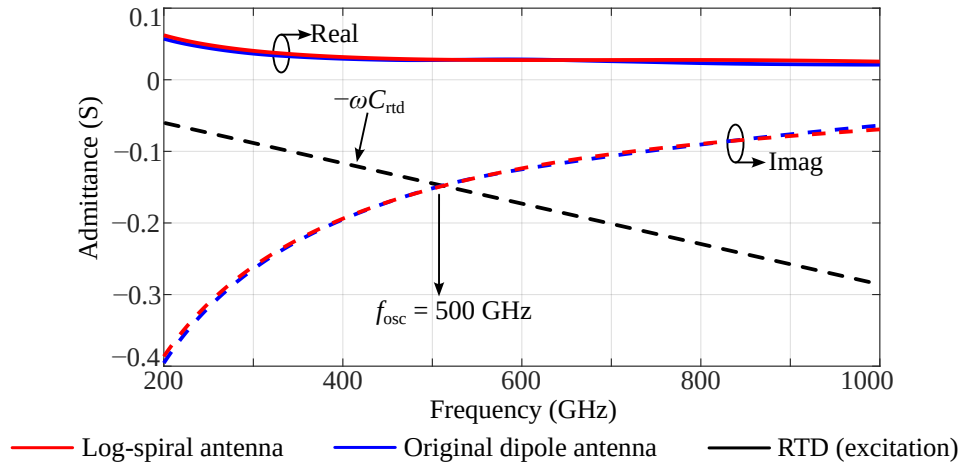

Figure 3.3. Comparison of Y-parameters simulated from the original dipole antenna and RTD with a log-spiral antenna. The oscillation frequency is at the crossing point where the negative susceptance of the RTD excitation balances the susceptance of the antennas.

antenna should not significantly affect the oscillation behaviors of the cavity-coupled RTD. The oscillation frequency occurs at the crossing point where the negative RTD susceptance and the antenna susceptance perfectly compensate each other. As depicted in Fig. 3.3, the original dipole design and the cavity RTD with a log-spiral antenna exhibit nearly identical Y-parameters, suggesting that the oscillation behaviors of the RTD is not affected by the spiral bias connections.

As shown in Fig. 3.4, the proposed CP RTD exhibits a radiation efficiency generally higher than the original dipole antenna design (Fujikata *et al.*, 2022). This improvement can be attributed to the reduction in losses induced by the stabilization resistors. The RTD with one truncated spiral arm provides a higher radiation efficiency than the normal spiral. The efficiency remains identical when the stabilization resistors are included. This result confirms that the ohmic loss from the resistors is negligible. The axial ratio is shown in Fig. 3.5(a). It is clear that the cavity-coupled RTD with the

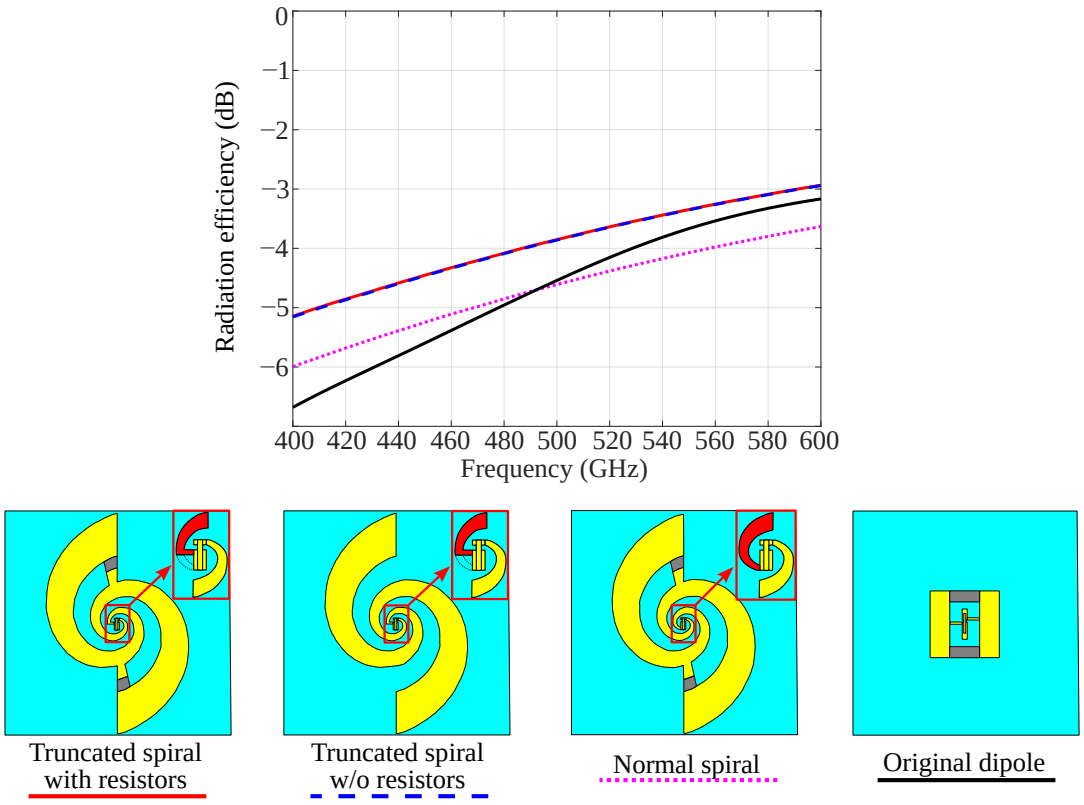

Figure 3.4. Simulated radiation efficiency. Original dipole (black curve), cavity-coupled RTD with normal spiral arms (purple dotted curve), truncated spiral arms (red curve) and truncated spiral arms without the stabilization resistors (blue dashed curve). The latter two overlap. The insets highlight the difference between the truncated spiral and normal spiral, emphasized by the red spiral arms.

spiral bias connections generates CP radiation with an axial ratio generally lower than 1 dB with a minimum 0.15 dB at around 520 GHz. When the silicon lens is included, reflections at the Si/air interface result in a slightly increasing and fluctuating axial ratio, which is overall still below 2 dB. As shown in Fig. 3.5(b, c), the hyper-hemispherical

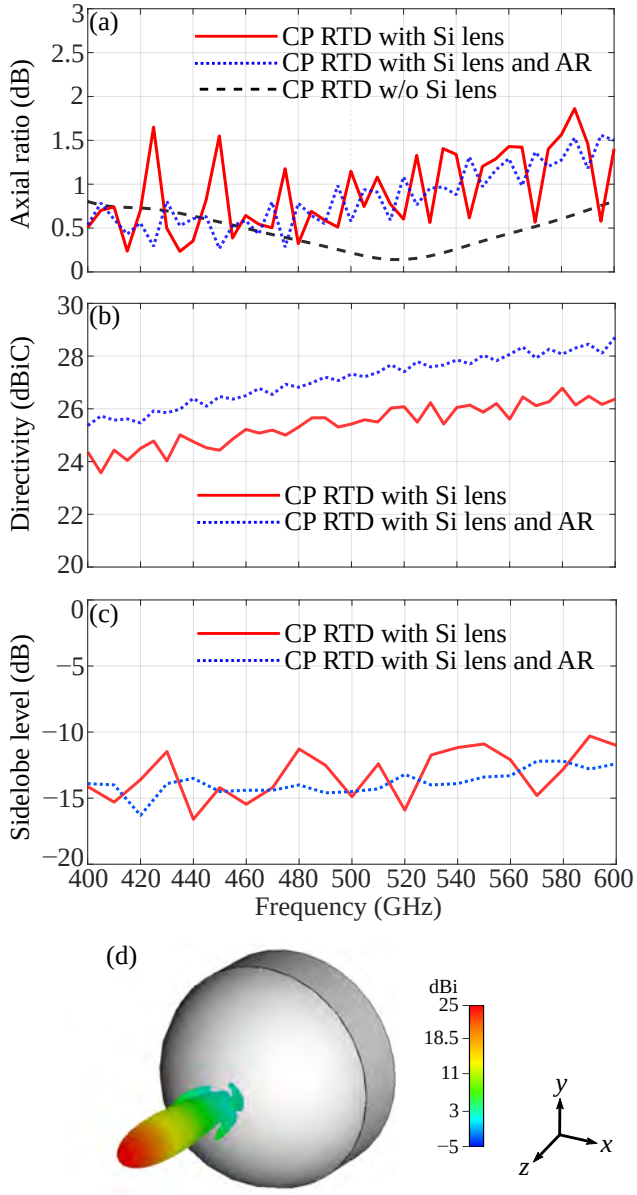

Figure 3.5. Simulation results between 400–600 GHz. (a) The axial ratio comparison for the CP RTD with a silicon lens with an ideal anti-reflection layer (blue dotted curve) and without the anti-reflection layer (red solid curve), and without the silicon lens (black dashed line). (b, c) Broadside directivity and sidelobe level for the CP RTD with a silicon lens with an ideal anti-reflection layer (blue dotted line) and without the anti-reflection layer (red solid curve). (d) 3-D CP radiation pattern at 500 GHz.

silicon lens extracts the output power and results in a broadside directivity of 25 dBiC with a 3-dB beamwidth of around 7°, and a sidelobe level of −15 dB at 500 GHz. The 3-D radiation pattern is shown in Fig. 3.5(d). While an anti-reflection layer on top of the silicon lens is expected to effectively smoothen the axial ratio, reduce the sidelobe level and further improve the directivity, it would raise cost issues. Compared to the previous CP RTD design with a radial line slot antenna (Horikawa *et al.*, 2018), this work is expected to provide a broader bandwidth with a smooth, low and stable axial ratio. Moreover, integration with the silicon lens contributes to a high gain performance, essential for future terahertz communications.

3.4 Conclusion

In this chapter, a cavity-coupled RTD with spiral bias connections for CP radiation has been proposed. The spiral arms are modified to match the RTD feed so that the radiation efficiency is improved. The stabilization resistors are placed beyond the active region of the spiral at the lowest operating frequency, so that the ohmic loss is minimized and their impact on the desired CP radiation is negligible. Simulation results clearly suggest that a highly directive and highly efficient CP radiation can be achieved with the silicon lens.

One challenge in future CP performance measurements is the limitation posed by the receiver equipment, a Helium-cooled bolometer which measures power intensity and is polarization insensitive. To address this challenge, the measurement can be conducted by incorporating a wire-grid polarizer. For perfect CP radiation, the received power intensity should remain consistent regardless of the rotation angle of the wire-grid polarizer. The rotation direction of the CP waves can be determined using a quarter-wave plate, which converts CP radiation into linearly polarized radiation. Following the quarter-wave plate, a wire-grid polarizer can be positioned to determine the CP rotation direction. A further investigation will include experimental wireless data transmission with both left-handed circular polarization (LHCP) and right-handed circular polarization (RHCP) antennas.

Chapter 4

Terahertz metasurface for near-field beam conversion

A uniform illumination over a screen is crucial for terahertz imaging. As such, conversion from a Gaussian beam to a flat-top beam becomes necessary. Most of the current beam conversion techniques rely on bulky multi-lens systems designed for a collimated input and operate in the far-field. This chapter presents a single metasurface lens to efficiently convert a quasi-Gaussian beam from the near-field region of a WR-3.4 horn antenna to a flat-top beam. The design process is divided into three steps to minimize simulation time and the conventional Gerchberg–Saxton (GS) algorithm is supplemented with the Kirchhoff-Fresnel diffraction equation. Experimental validation confirms that a flat-top beam with an efficiency of 80% has been achieved at 275 GHz.

4.1 Introduction

Benefitting from a unique non-destructive penetration capability and high spatial resolution, terahertz radiation is highly promising for a wide range of imaging applications (García-Rial *et al.*, 2019; Lee *et al.*, 2020, 2022; Moradikouchi *et al.*, 2022). A flat-top beam with a homogeneous area of illumination is preferable to a commonly used Gaussian beam for applications such as active imaging systems (Kleindienst *et al.*, 2010) and super-resolution techniques (Stehr *et al.*, 2019). It should be clarified that in the microwave community, a flat-top beam is typically a far-field concept that refers to the flatness of power as a function of angle (Singh *et al.*, 2019). In this chapter, we follow the near-field concept from the optical society to observe a uniform illumination on a planar screen.

Conversion from a Gaussian to flat-top intensity distribution requires a beam-shaping technique. While physical truncation of a Gaussian beam is the simplest solution to generate a quasi-flat-top profile, the overall efficiency is significantly degraded. In the optical regime, commercial refractive beam shapers have been already employed with high efficiency for laser wavelengths ranging from ultraviolet to mid-infrared. However, as the wavelength becomes longer in the terahertz frequency band, such refractive curved lenses (Abbaszadeh *et al.*, 2019) or aspheric lens combinations (Price *et al.*, 2020) that refract the incident wave are generally bulky, lossy and non-integrable for terahertz systems. Alternatively, low-profile diffractive elements fabricated by 3-D printing technology are popular beam-shapers for computational holographic imaging (Liao *et al.*, 2020; Jia *et al.*, 2022) to generate arbitrary field distribution. The 2π phase coverage is typically realized by varying the dielectric pillar height. A terahertz Gaussian beam to flat-top intensity transformation through two diffractive phase plates was demonstrated (Ye *et al.*, 2018). However, the separation between phase plates of around 50 wavelengths gravely compromises the system compactness. The conversion efficiency and overall uniformity, which can be expressed by the variance of the field intensity, remain low.

One promising approach for beam shaping is the use of a metasurface, which is a quasi-periodic sub-wavelength resonator array that tailors the electromagnetic wave behavior. A recently-proposed all-dielectric metasurface lens designed via the geometry transform technique was predicted to convert a Gaussian input beam to a flat-top beam at 100 GHz with high efficiency (Abbaszadeh *et al.*, 2020). However, the structure was not realized since it requires a complicated etching process and additional anti-reflection layers. A flat-top beam shaper can be further scaled to the microwave range, e.g., 10 GHz (Li *et al.*,

2020) based on simultaneous phase and amplitude control. Most of the aforementioned methods assume a collimated input wavefront, which requires additional spherical lenses and operates in the far-field region from the source. Moreover, conventional metasurfaces typically provide relatively low conversion efficiency below 70%, while an all-silicon metasurface at 300 GHz requires an etching depth of over 600 µm, which is difficult to realize.

As an alternative, multi-layer metasurfaces (Grady *et al.*, 2013; Cong *et al.*, 2013, 2014; Chang *et al.*, 2017) allow manipulation of terahertz wave transmission with high efficiency. Recent progress suggests that a tri-layer metasurface consisting of three metallic layers and two dielectric spacers can achieve a highly efficient polarization conversion within ultra-wide bandwidth (0.2–1.0 THz) (Ako *et al.*, 2020) and can be extensively implemented for high-gain antennas (Medrar *et al.*, 2021) and multi-channel holographic imaging (Zhao *et al.*, 2023).

In this chapter, a tri-layer metasurface lens is adopted for beam conversion in the near-field of a 275 GHz terahertz source. Preliminary simulation results have been previously reported in Li *et al.* (2022b). The unit cell is designed and simulated over the WR-3.4 frequency band (220–330 GHz) in CST Microwave Studio, including an investigation on the tolerance of the unit cell to the incidence angle, since angle variations are exacerbated in the near field. The phase profile is then calculated for the metasurface lens based on the modified Gerchberg–Saxton (GS) algorithm (Gerchberg and Saxton, 1972). This work tackles two design challenges. Firstly, the metasurface lens is placed close to the horn antenna for portability and, therefore, the near-field input wavefront is non-planar. Secondly, simulation of the entire structure is impractical due to the intrinsic deep subwavelength meshing required for resolving the metasurface against a large near-field space with respect to wavelength. The proposed solutions of the metasurface design and the hybrid-task simulation in CST will be discussed.

4.2 Design and analysis

4.2.1 Unit cell

The three-dimensional view of the tri-layer metasurface unit cell (Grady *et al.*, 2013) is shown in Fig. 4.1(a). A split ring resonator (SRR) is located between two orthogonal wire grids. These three metallic layers are separated by two cyclic olefin copolymer

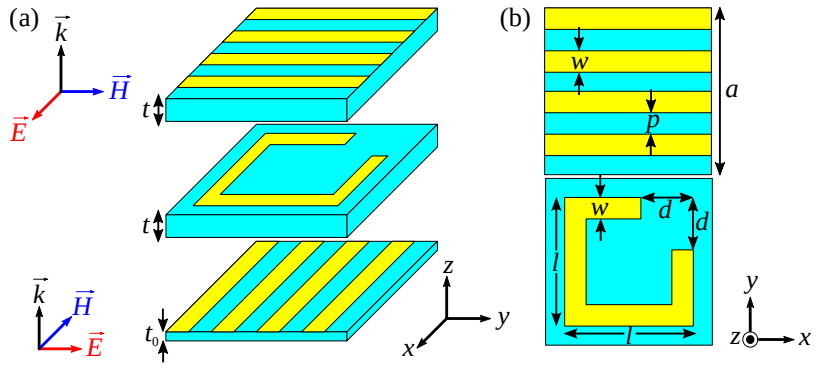

Figure 4.1. Tri-layer metasurface unit cell. (a) Exploded view. The two top COC spacers have identical thickness t of 100 µm, which is within the fabrication limits. The bottom COC layer has a thickness t_0 of 3 µm to support the bottom wire grids. (b) Dimensions of the wire grids layer and the resonator layer. The square unit cell size a, gold wire strip width w and separation p are chosen as 240 µm, 15 µm and 15 µm, respectively. The middle SRR has a variable size of l, an opening gap of d and the same strip width of $w = 15$ µm. All gold layers have a thickness of 200 nm.

(COC) spacers with an identical thickness of t. COC as a low-loss material, has a relative permittivity of $\epsilon_r = 2.33$ and loss tangent of $\tan\delta = 0.0005$ over the WR-3.4 frequency band. Figure 4.1(b) shows the detailed dimensions of the wire grid and the middle SRR. The square unit cell size a of 240 µm is in the sub-wavelength scale to avoid diffraction. The SRR geometry is controlled to achieve different phase responses. The tri-layer metasurface is able to efficiently rotate a linearly polarized wave and operate as a phase shifter. Assuming a linearly polarized wave in the y-direction that is normally incident to the metasurface, the wave will experience multiple reflections inside the dielectric cavity while being scattered by the middle SRR, which will result in a cross-polarized output in the x-direction (Grady *et al.*, 2013). The metasurface structure is designed through full-wave simulations, applying unit cell boundary conditions and a plane-wave excitation in CST Microwave Studio.

As can be seen from Fig. 4.2(a), the cross-polarized transmission magnitudes for four different SRRs are above -1 dB at the desired operating frequency of 275 GHz and the responses remain stable for both TE and TM modes for an incidence angle of up to 30°. As shown by the shaded areas in Fig. 4.2(a), the maximum magnitude variations are within -0.4 dB. The co-polarization level remains below -30 dB. The corresponding phase responses for the eight represented SRRs for the normal incidence are shown in Fig. 4.2(b). The graph clearly indicates that the adjacent configurations have a 45° phase

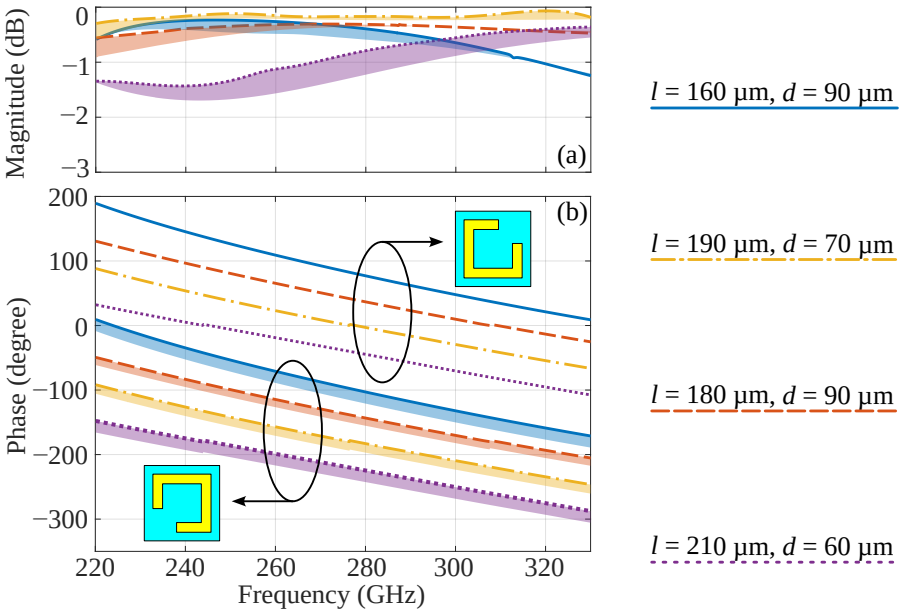

Figure 4.2. Simulated performance of unit cells. Four unit cells based on different resonator parameters l and d are simulated and the transparent areas underneath indicate the variations in response to an oblique incidence angle up to 30°. (a) Magnitude responses. (b) Phase responses. Flipping the resonators results in 180° phase difference while the magnitude responses remain the same.

difference and a total of eight SRRs (four SRRs and their flipped versions) is able to cover the 2π phase range. The phase variations for the incidence angle of up to 30°, as shown by the shaded areas, are within 15°. These resonators can be mapped to the discretized spatial phase profile that is required to convert a Gaussian beam to a flat-top beam.

4.2.2 Metasurface lens

The schematic of the proposed Gaussian to flat-top conversion is shown in Fig. 4.3(a). A diagonal horn antenna WR-3.4 from Virginia Diodes, Inc., is used to generate a quasi-Gaussian input. The metasurface lens is placed at a distance of d_1 from the horn's aperture to allow field expansion while the field is confined within the desirable metasurface aperture. The observation plane is at d_2 from the metasurface lens. Considering the system compactness, d_1 = 10 mm and d_2 = 50 mm, which are within the near-field region of the horn antenna and the metasurface, respectively. While dictated by application, d_2 must be large enough that the metasurface lens has a phase variation sufficiently

slow to be resolved. The metasurface lens comprises 52×52 unit cells and the overall size is around 12×12 mm^2, resulting in a maximum incidence angle around 30°. Based on the phase variations in Fig. 4.2(b), the effect of oblique incidence is negligible. It should be clarified that this angular tolerance is applicable at the unit cell level to account for the effect of beam divergence. The Gaussian input profile can be expressed as: $E(r) = E(0) \cdot \exp[-(r/w_1)^2]$, where w_1 is the Gaussian beam radius at the input to the metasurface and r is the radial distance. The target flat-top beam profile can be expressed as a super-Gaussian function: $E(r) = E(0) \cdot \exp[-(r/w_2)^q]$, where w_2 is the flat-top radius and q is the order of the super-Gaussian function where higher q results in steeper edges of the profile. Note that a steeper edge leads to a quicker distortion of the flat-top profile away from the target distance. For this flat-top beam shaper, at an operating frequency of 275 GHz, an input Gaussian beam with w_1 = 2.6 mm is converted to a flat-top beam with w_2 = 20 mm and q = 6. The order q is determined to have best uniformity. It is worth pointing out that a large beam size with respect to the projection distance demands a metasurface with a rapid phase variation, which is prone to error due to coupling between different unit cell designs.

The phase profile of the beam shaper can be obtained through various classical methods, such as GS algorithm (Gerchberg and Saxton, 1972), Yang-Gu algorithm (Yang *et al.*, 1994) and geometrical transform technique (Bryngdahl, 1974). Since the conventional analytical solution for Gaussian to flat-top conversion is not suitable for future investigations on shaping arbitrary beams, the phase profile of this metasurface lens is obtained through an adaptive GS algorithm, which is more general. An analytical solution is later shown for comparison. For a standard GS algorithm, the target plane is assumed at the far-field region from the beam shaper so the relationship between the source and the target diffraction pattern can be expressed by the Fraunhofer diffraction equation, which is basically a Fourier transform. In this case, the target is placed in the near-field region from the metasurface. Therefore, the conventional Fourier transform is replaced by the Fresnel transform, i.e., the relationship is expressed by the Kirchhoff-Fresnel diffraction equation instead of the Fraunhofer diffraction equation. Since the metasurface lens is to be placed in the near-field region of the source, the size of the lens is reasonably small and the calculation process finishes in less than 10 minutes for a standard workstation. The GS algorithm starts with an arbitrary phase profile and the resultant profile is shown in Fig. 4.3(b). Since the metasurface lens is operating in the near-field region and therefore the input wavefront is non-planar, an additional phase profile is required as demonstrated in Fig. 4.3(c) to collimate such a non-planar wavefront. Consequently, the

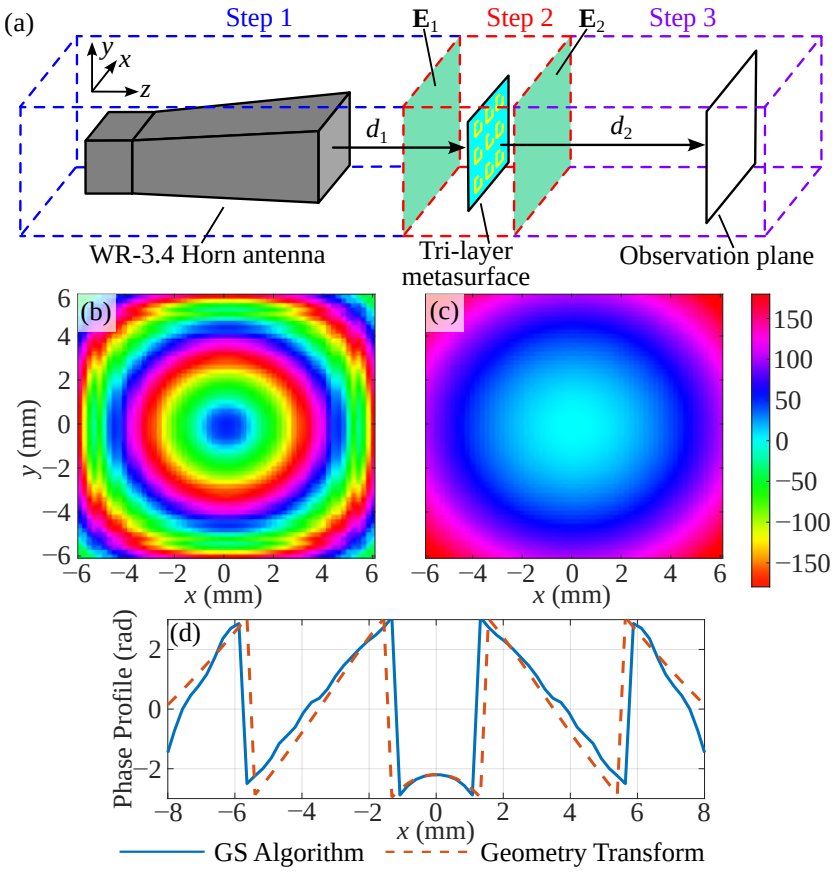

Figure 4.3. Metasurface lens phase profile. (a) Design schematic. (b) Phase profile obtained from GS algorithm for Gaussian to flat-top beam conversion. (c) Phase profile for spherical wavefront collimation. (d) Phase profile for the metasurface lens, as a summation of (b) and (c).

metasurface lens is designed with functionalities of beam collimation and beam shaping simultaneously. The final phase profile for the metasurface lens is a summation of the two aforementioned phase profiles. To validate the retrieved phase profile, an analytical expression is obtained from the geometrical transform technique (Abbaszadeh *et al.*, 2020). Figure 4.3(d) indicates that the phase profiles calculated from the two synthesis methods are consistent.

The phase profile is discretized and mapped to the metasurface lens through the eight unit cells. Its operation is then verified in CST simulation software. The simulation is divided into three parts as shown in Fig. 4.3(a), since the intrinsic subwavelength meshing for the metasurface is computationally demanding, especially for a long propagation distance with respect to wavelength. The first step merely simulates the horn antenna and records the complex E-field distribution $\mathbf{E}_1(x, y)$ close to the metasurface. The second step simulates the metasurface lens excited by the previously

recorded field source $\mathbf{E}_1(x,y)$. The boundary is placed at a very close distance from the metasurface so that the simulation time remains reasonable. Meanwhile, the E-field distribution $\mathbf{E}_2(x,y)$ is recorded in the second step. Then the field source $\mathbf{E}_2(x,y)$ is used as an excitation in the third step, which simulates a large empty space in front of the metasurface and provides the final flat-top beam distribution at a desired distance. Since the reflection coefficients of most unit cells are lower than -10 dB, this process neglects muti-reflections between the metasurface lens and the horn antenna.

4.3 Fabrication and measurement

As shown in the experiment setup in Fig. 4.4, a vector network analyzer Keysight N5222B with VDI extension modules operating from 220–330 GHz is used to conduct the measurement. The quasi-Gaussian profile output from the diagonal horn antenna WR-3.4 is converted to a flat-top profile output at the observation plane, which is then detected by the near-field probe connected with a waveguide twist to account for polarization rotation. The detector is mounted on a two-axis motorized stage for a scanning area of 50×50 mm^2. The spatial resolution of the scanner is set to 1 mm to match the diffraction limit. The inset shows a microscope image of the resonator layer of the metasurface lens and the detailed fabrication process has been previously reported in Ako *et al.* (2020).

Figure 4.5(a, b) shows the simulated 2-D intensity comparison at 275 GHz with and without the proposed tri-layer metasurface lens, and the measured 2-D intensity comparison is shown in Fig. 4.5(c, d). It clearly indicates that after applying the metasurface

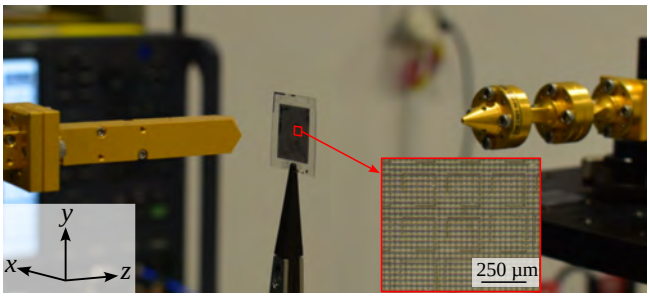

Figure 4.4. Measurement setup. The horn antenna is placed at the left as the source and the near-field probe with a waveguide twist is placed at the right for complex amplitude detection. The inset shows a microscope image of the resonators.

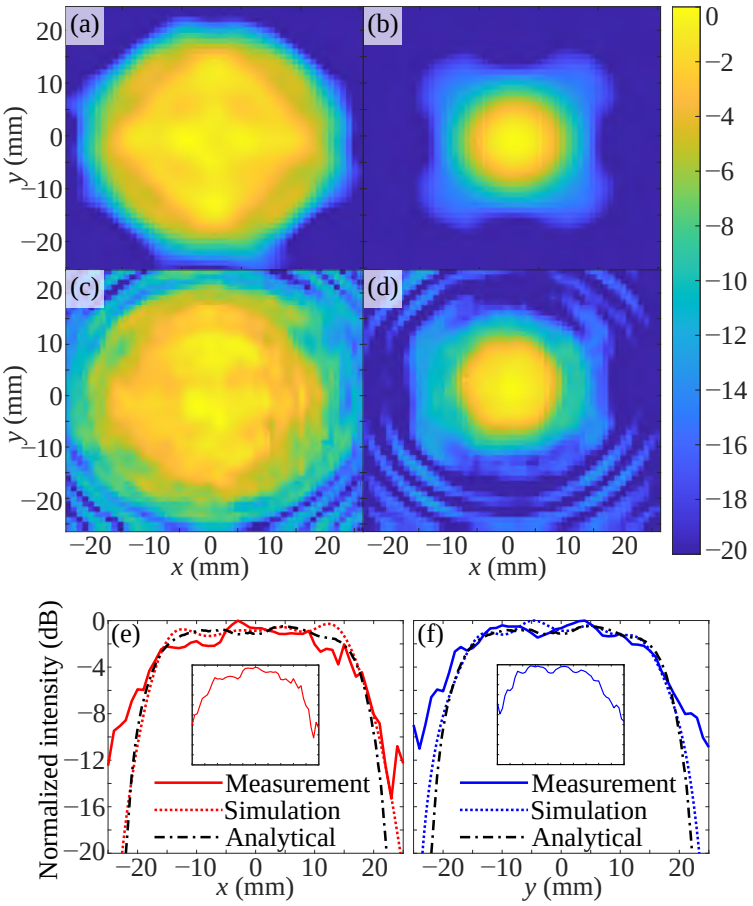

Figure 4.5. Measurement results at 275 GHz. The intensity distributions are normalized to their own maximum values. (a, c) Simulated and measured flat-top beam with the metasurface lens. (b, d) Simulated and measured quasi-Gaussian beam without the metasurface lens. (e, f) Comparison between simulated, analytical and measured flat-top profiles at $y = 0$ and $x = 0$, respectively. The insets show the measured profile when the sample is not well-aligned, with scales showing the behavior within the same limits as the main graph.

lens the distribution becomes a flat-top profile, while it remains Gaussian without the metasurface lens. The sidelobes observed in the measurement can be explained by the limited aperture size. The measured intensity in both the *E*- and *H*-planes are then compared with an analytical estimation obtained through the Fresnel diffraction integral and the simulation results obtained from CST. As shown in Fig. 4.5(e, f), the comparisons show good agreement. The angular tolerance is roughly estimated to $<5°$ to attain the expected performance. The efficiency is a ratio between the integrated measured power of the flat-top beam, and the Gaussian beam power generated by the horn antenna at the same distance without the metasurface. As can be seen from Fig. 4.6(a), a measured efficiency of over 80% ($\sim$0.15 mW power loss from the Gaussian

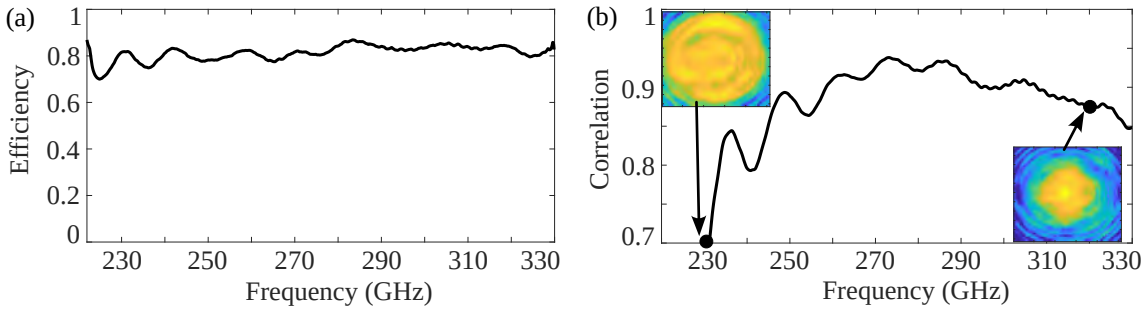

Figure 4.6. Measurement results over the WR-3.4 frequency band. (a) Measured efficiency. (b) Correlation between the measured intensity and the ideal super-Gaussian intensity in linear scale. The insets show the measured intensity at 230 GHz and 320 GHz. Same colorbar as Fig. 4.5(a–d) applied.

beam power of 0.77 mW) can be achieved by this tri-layer metasurface, suggesting a highly efficient conversion and the result is consistent with previous work (Ako *et al.*, 2020). Figure 4.6(b) quantifies the quality of the flat-top beam. The correlation between the normalized measured intensity and the ideal flat-top intensity peaks at around the center operating frequency of 275 GHz. At marginal frequencies, e.g., 230 GHz and 320 GHz, the beam shapes deviate from the flat-top beam.

4.4 Conclusion

In this chapter, a highly efficient Gaussian to flat-top beam conversion through a tri-layer metasurface has been proposed. The phase profile of the metasurface lens is obtained by the modified GS algorithm. Eight configurations of the resonators covering the 2π phase range are mapped to the discretized phase profile of the metasurface lens. The metasurface lens is placed in the near-field region of a horn antenna for a compact illumination system. Hence the phase profile for the spherical input wavefront is taken into consideration as well. Measured results agree well with simulated and analytical results, suggesting successful Gaussian to flat-top beam conversion. Future investigations will include arbitrary input field distributions from different sources, arbitrary output field distribution for holographic applications, mitigating the interference between adjacent unit cells and a flat-top beam illuminated from an angle.

Chapter 5

Planar high-gain antenna for terahertz communications

TERAHERTZ sources require compact lenses for efficient outcoupling and manipulation of terahertz waves. Traditional terahertz lenses are bulky and require high-precision fabrication techniques such as micromachining, which limit their flexibility in integrated systems. In this chapter, a planar high-gain cavity antenna integrated with a waveguide feed is presented. The antenna is made by laser-etching of high-resistivity float-zone silicon to create non-uniform hole arrays, which function as gradient-index (GRIN) lenses for beamforming. To address the insufficient phase coverage range caused by limitations in feasible etching depth and the intrinsically tapered side walls of the holes, direct laser-etching is performed on both sides of the silicon wafer. The silicon cavity antenna is experimentally validated, with results confirming that a maximum broadside gain of 19 dBi can be achieved at the center frequency of 275 GHz, with a 3-dB bandwidth of around 29%. Such a high-gain antenna is applicable to error-free point-to-point short-range wireless signal transmission. A demonstration of uncompressed 4K-resolution video transmission is also included.

5.1 Introduction

High-gain antennas are crucial to support the link budget and to conserve precious power for terahertz communications and sensing. To achieve stable high-gain and large-bandwidth performance, silicon-micromachining technology enables the realization of complex structures with micrometer-level features, such as corporate-feed array antennas (Gomez-Torrent *et al.*, 2020b) and parallel-plate waveguide-based antennas (Gomez-Torrent *et al.*, 2020a). Nevertheless, their practical utilization is hindered by the complicated micromachining and bonding techniques. The insertion loss significantly increases with the array size, in particular due to the ohmic loss. Lenses are commonly used to achieve high-gain radiation with integrated sources, as they can be easily scaled and attached to waveguide sources to facilitate the outcoupling of terahertz radiation (Konstantinidis *et al.*, 2017). However, the small size of the waveguide slot limits the effective aperture, thereby requiring a larger lens size for aperture expansion. To overcome this limitation, the resonant cavity antenna (RCA) has emerged as a promising solution in the millimeter- and submillimeter-wave ranges (Hayat *et al.*, 2020; Baba *et al.*, 2019). As mentioned in Afzal *et al.* (2015), the RCA is also known by various names such as Fabry-Perot cavity antennas (FPAs), partially reflective surface (PRS) antennas, electromagnetic band gap (EBG) antennas, 2-D leaky-wave antennas (LWAs), and most recently spaceplate (Mrnka *et al.*, 2022). These names essentially refer to a similar low-profile antenna structure that utilizes an air gap for aperture expansion. The concept offers advantages such as mechanical scanning capabilities (Goudarzi *et al.*, 2022) and polarization control (Guo *et al.*, 2021). Subsequent research suggests that the antenna gain and bandwidth can be further improved through the use of a curved cavity and multi-level partially reflective surface (Wu and Luk, 2017; Niaz *et al.*, 2021).

To extend the functionality of cavity antennas to terahertz frequencies, the concept of a terahertz cavity antenna is typically implemented using a hyper-hemispherical silicon lens and an air cavity with a half-wavelength dimension (Llombart *et al.*, 2011; Alonso-delPino *et al.*, 2019). In recent years, extensive investigations have been conducted on such quasi-optical setups, including rigorous analysis methodology (Bosma *et al.*, 2022a), polarization control (Campo *et al.*, 2021a) and lens array for a large scanning range of $\pm 25°$ (Bosma *et al.*, 2022b; Campo *et al.*, 2021b; Alonso-delPino *et al.*, 2021). A recently proposed silicon frusta structure, fabricated by laser ablation on a curved surface, was shown to provide broadband, nearly lossless impedance matching between a silicon-air interface (Bueno *et al.*, 2022). While those costly solutions are suitable for

niche applications such as astronomy (Baselmans *et al.*, 2022) and specialized industries (Leuchs *et al.*, 2022), they may not be viable for high-volume consumer products. To minimize the device profile, Fresnel lens or discrete lens designs have been reported through 3-D printing technology (Wu *et al.*, 2019a; Yi *et al.*, 2016). Besides the sacrificed bandwidth, the radiating performance is constrained by the printing resolution and a non-negligible dielectric loss. Another integrable approach for discrete lenses is the use of metasurface. A transmitarray composed of half-wavelength unit cells enables local phase control for beamforming. However, a substantial dielectric loss of $\sim$2 dB has been reported at the terahertz frequency band (Medrar *et al.*, 2021).

While planar silicon lens antennas based on effective medium are promising, they mainly interface 2-D integrated platforms with free-space on one substrate edge and hence in this configuration the aperture remains limited to 1-D (Withayachumnankul *et al.*, 2018; Liang *et al.*, 2021; Headland *et al.*, 2018b; Dechwechprasit *et al.*, 2023). For applications where a pencil beam is required, broadside effective-medium antennas are needed. An example of such an antenna with circularly polarized radiation was proposed in the millimeter-wave range (Melendro-Jimenez *et al.*, 2023). Interestingly, existing designs at terahertz frequencies have shown significant reflection loss and limited directivity (Pursula *et al.*, 2019; Lamminen *et al.*, 2022).

In this chapter, a planar silicon high-gain cavity antenna with an integrated waveguide feed operating from 228–308 GHz is presented. The fabrication process involves direct laser-etching of blind cylindrical air holes on a 2 mm thick high-resistivity float-zone silicon wafer. By adjusting the density of these fixed-sized holes, the effective dielectric constant can be spatially controlled on the wafer for phase correction. To address the issue of insufficient phase coverage range caused by the limited feasible etching depth and the intrinsically tapered side walls, a cavity antenna design that incorporates both top and bottom effective medium layers as gradient-index (GRIN) lenses is proposed. Additionally, an air cavity is introduced between the waveguide and the silicon to facilitate aperture expansion. The analysis of the cavity antenna is provided in Section 5.2. The detailed fabrication process and measurement results is included in Section 5.3. In Section 5.4, wireless communications capabilities supported by the proposed planar cavity antenna is demonstrated, before the conclusion of the chapter in Section 5.5.

5.2 Antenna Design and analysis

5.2.1 Effective medium for GRIN

An example illustrating the effective medium principle is shown in Fig. 5.1(a) from a top view. In this example, we consider a float-zone silicon substrate with a relative permittivity ϵ_{si} of 11.68 ($n_{si} = 3.418$) and a resistivity of 20 kΩ-cm. Such high-resistivity silicon is a desirable material for terahertz antennas due to its broadband low dissipation loss, i.e., $\tan\delta = 0.00002$ at 1 THz (Dai *et al.*, 2004). The effective medium is implemented using blind air holes with a subwavelength period and a fixed diameter d. Given the fabrication repeatability and controllability, it is crucial to maintain a constant air hole size while adjusting the density. Although varying the hole size could be an alternative to realize GRIN lenses (Lamminen *et al.*, 2022), it may introduce unexpected effects in radiation performance due to variable side wall angles. The relative permittivity of the effective medium stays between that of air and silicon, and it is determined by the percentage of air fill within the unit cell. From Fig. 5.1, as the air hole density becomes

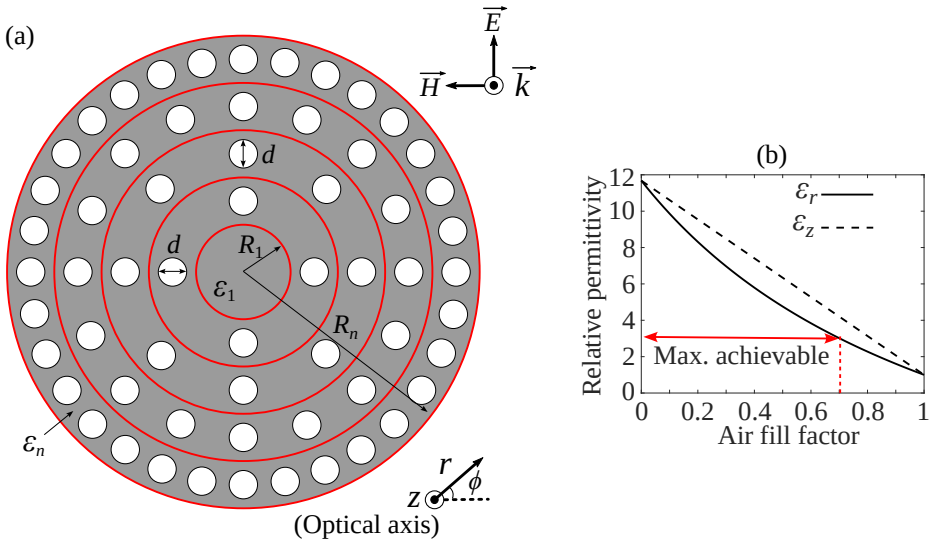

Figure 5.1. Effective medium principle. (a) Top view showing a GRIN lens. The high-resistivity float-zone silicon disk is divided into five rings, each containing fixed-size air holes with varying density. The air holes have sub-wavelength separation, and their density increases along the radial direction, resulting in a reduction of the relative permittivity in each ring. (b) Effective relative permittivity as a function of the air fill factor. The maximum air fill factor achievable is around 70%. This limit is due to the ring configuration and necessity of a minimum 10 µm air gap between adjacent holes to avoid merging.

larger in the radial direction, the effective relative permittivity of each ring decreases. More specifically, the relation can be obtained from Maxwell-Garnett approximations Cheben *et al.* (2018); Subashiev and Luryi (2006) for polarization-dependent effective relative permittivity. For the E-field components perpendicular to the optical axis E_r and parallel to the optical axis E_z, the corresponding relative permittivities ϵ_r and ϵ_z are given by:

$$\epsilon_r = n_r^2 = \epsilon_{\text{si}} \frac{(\epsilon_{\text{si}} + \epsilon_{\text{air}}) + (\epsilon_{\text{air}} - \epsilon_{\text{si}})\zeta_n}{(\epsilon_{\text{si}} + \epsilon_{\text{air}}) - (\epsilon_{\text{air}} - \epsilon_{\text{si}})\zeta_n} , \tag{5.1}$$

$$\epsilon_z = n_z^2 = \epsilon_{\text{si}} + (\epsilon_{\text{air}} - \epsilon_{\text{si}})\zeta_n , \tag{5.2}$$

where ϵ_{air} and ϵ_{si} are the relative permittivities of air and silicon, which equal 1.00 and 11.68, respectively. The air fill factor ζ_n represents the percentage of air in the n^{th} silicon ring and can be calculated by using the following equation:

$$\zeta_n = \frac{N_n \pi d^2}{4 A_{\text{ring}}} , \tag{5.3}$$

where N_n is the number of air holes in the n^{th} ring, d is the hole diameter and A_{ring} is the area of the silicon ring that can be expressed by $(R_n^2 - R_{n-1}^2)\pi$. As shown in Fig. 5.1(b), the effective relative permittivity for both polarizations exhibits a monotonous decrease with increasing fill factor. However, since the optical axis aligns with the z-axis, the E_r component dominates the wave propagation and the E_z component that would be a paraxial approximation can be neglected for lens design. Nonetheless, it is prudent to use the equivalent anisotropic permittivity tensors in full-wave simulations to ensure accurate results.

5.2.2 Cavity antenna design based on effective medium

To design the effective medium, we first consider the ideal air hole depth required for a single layer of effective medium to achieve a required 2π phase range, as obtained when adjusting the hole density:

$$h_{\text{EM}} = \frac{2\pi}{k_0 (n_{\text{max}} - n_{\text{min}})} , \tag{5.4}$$

where k_0 is the wave number at the center frequency of 275 GHz, n_{max} is the refractive index of solid silicon = 3.418 and n_{min} is the effective refractive index corresponding to the largest fill factor. Given a fixed hole diameter d, the largest achievable fill factor is typically smaller than 100%, i.e., 100% fill factor corresponds to pure air. Given the hole

diameter d and ring width of $R_n - R_{n-1}$, the largest number of air holes achievable can be expressed by:

$$N_{\max} = 2\pi/\phi_{\min} \,, \tag{5.5}$$

where the smallest central angle $\phi_{\min}$ is

$$\phi_{\min} = 2\sin^{-1}\left(\frac{d}{R_n + R_{n-1}}\right) \,. \tag{5.6}$$

By combining Eqs. 5.3, 5.5, and 5.6, the largest air fill factor achievable by adjusting the air hole density can be simplified to the following equation when $\phi_{\min}$ is small:

$$\zeta_{\max} = \frac{d\pi}{4(R_n - R_{n-1})} \,. \tag{5.7}$$

In order to keep the ring in the sub-wavelength scale, the ring width is chosen as 80 µm. Adjacent holes require a clearance of 10 µm to minimize the aspect ratio for ease with fabrication, hence the air hole diameter is chosen as 70 µm. Such a setting will provide a maximum fill factor of 70%. Therefore, from Eqs. 5.1 and 5.4, the required minimum air hole depth is equal to 630 µm and rounded to 600 µm.

However, the current fabrication process faces challenges in achieving straight air holes etched down into silicon over significant depth. While the aperture-depth aspect ratio of 70:600 falls within the conventionally acceptable range of 1:10, the absolute depth of 600 µm poses difficulties for laser etching. A sliced silicon sample with etched holes of around 600 µm depth is depicted in Fig. 5.2(a), illustrating the tapered nature of the air

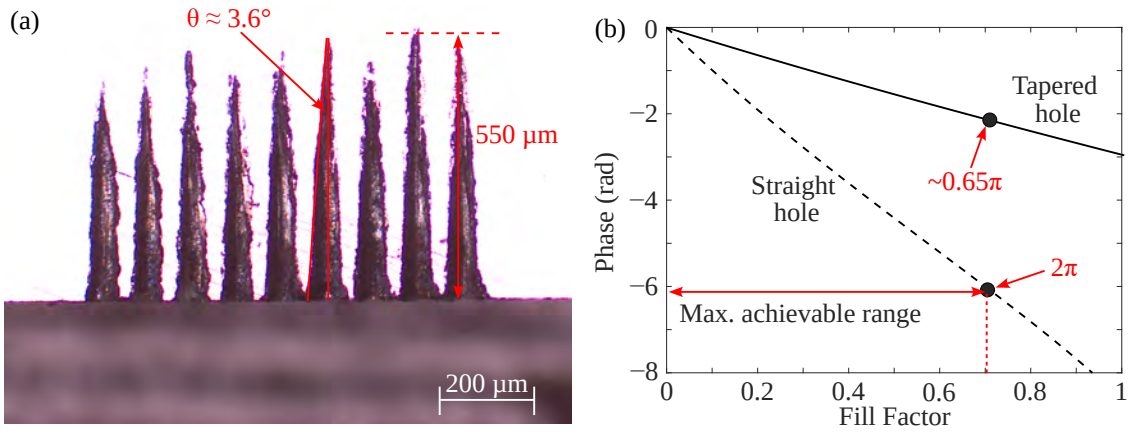

Figure 5.2. Tapered air hole structure. (a) Cross-sectional view of a sliced silicon sample. The air hole with a diameter of 70 µm is designed for a targeted etching depth of 600 µm. The actual etching depth achieved is approximately 550 µm and the side wall exhibits a tapered angle of around 3.6°. (b) Phase coverage at center 275 GHz as a function of fill factor.

5.2.2 Cavity antenna design based on effective medium

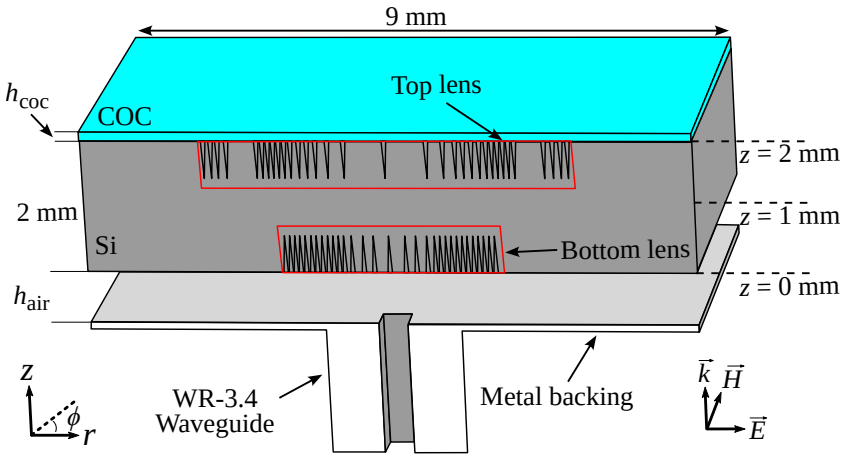

Figure 5.3. Silicon cavity antenna based on double-sided effective medium. Cross-sectional view. The WR-3 waveguide with a metal backing is positioned $h_{air} = 700$ µm below the silicon substrate to create the air cavity. Fixed-size air holes are laser-etched from both sides of the silicon substrate. A COC film of $h_{coc} = 100$ µm is placed on top of the silicon to mitigate the silicon-air impedance mismatch.

holes with an approximate angle of 3.6°. The presence of tapered side walls significantly impacts the phase correction performance of the GRIN lens. With straight air holes, as depicted in Fig. 5.2(b), the phase coverage reaches around 2π at a maximum achievable fill factor of approximately 70%. However, considering the 3.6° tapered angle, the phase coverage range is reduced to around 0.65π, which is less than half of the requirement. The insufficient phase coverage leads to a less-planar output wavefront. For example, in the case of our previous design based on simulation (Li *et al.*, 2022a), where the bottom effective medium layer functioned as a cavity and only the top effective medium functioned as a GRIN lens to correct the wavefront, the tapered side walls resulted in a low radiation gain.

To overcome the issue of insufficient phase coverage, both the top and bottom surfaces of the silicon wafer are etched to form effective medium layers that collectively operate as complementary GRIN lenses. The overall structure is illustrated in Fig. 5.3. Here, blind fixed-sized air holes are laser-etched into both sides of a 2 mm high-resistivity float-zone silicon wafer. This structure hosts two effective medium layers that increase the flexibility for the planar cavity antenna design. To improve the impedance matching to free-space on the top surface, a COC film of approximately a quarter wavelength is placed on the top side of the silicon cavity antenna. To enable moderate field expansion, an air gap of h_{air} is introduced between the silicon cavity antenna and the waveguide. Wave propagation undergoes partial phase correction through the bottom effective

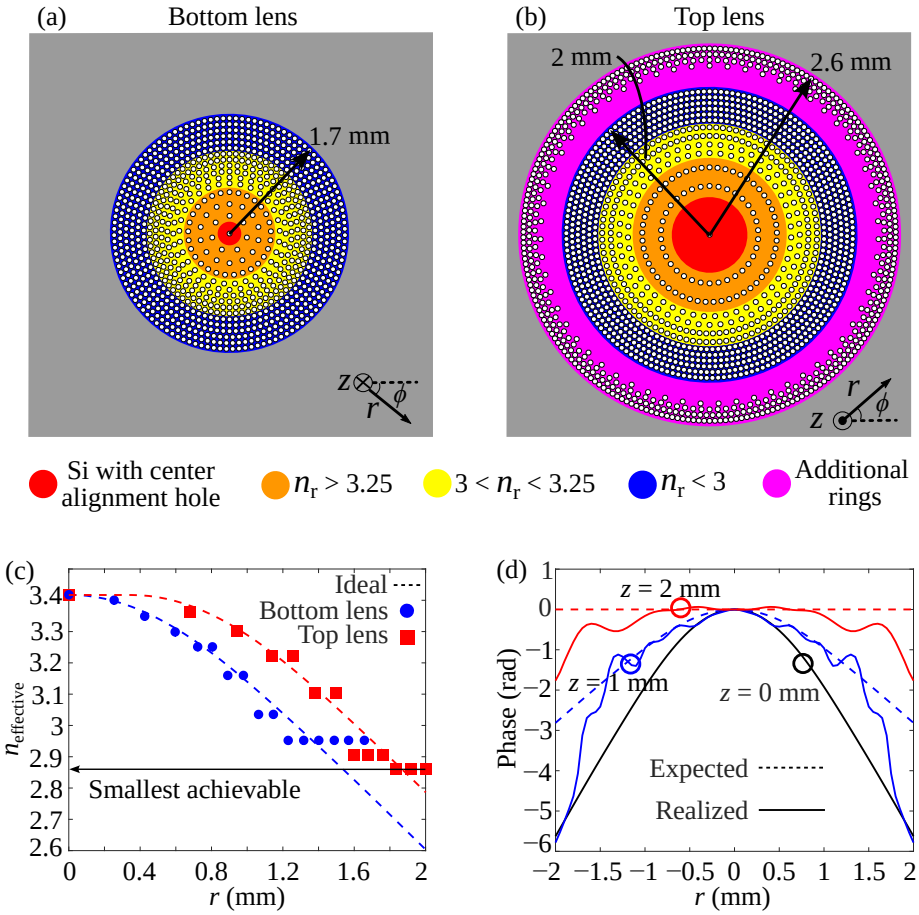

Figure 5.4. Laser-etched air hole patterns. (a, b) Bottom and top lens pattern. The colormap indicates different parts of the GRIN lenses. (c) Effective refractive index along the radial direction, under the condition of tapered air holes. The dashed lines indicate the continuous refractive index distributions for ideal phase compensation. (d) Simulated phase profile along the E-plane at different z locations. The phase profiles along the E- and H-planes are similar due to the radial uniformity of the GRIN lens.

medium, followed by an expansion through a short propagation path within the bulk silicon, and ultimately generates a planar wavefront after passing through the top effective medium. Figures 5.4(a) and 5.4(b) show the patterns for the bottom and top effective medium lenses, respectively. The effective refractive indices in different regions of both lenses can be found in Fig. 5.4(c). Initially, in the design simulation performed with CST Microwave Studio, reflections from the top silicon side are neglected for simplicity. The design of the bottom effective medium begins with an estimation that h_{air} should be selected close to half a wavelength at the center frequency of 275 GHz or $h_{\text{air}} = 550$ µm to radiate the leaky-wave mode to broadside. To eliminate the need of a matching iris (Llombart *et al.*, 2011), h_{air} is optimized to 700 µm to maximize return loss.

5.2.2 Cavity antenna design based on effective medium

The matching between the open waveguide and the silicon cavity antenna also benefits from the gradual permittivity transition caused by the tapered side walls, similar to the concept presented in Alonso-delPino *et al.* (2021).

The simulated phase profile at the beginning of the silicon $z = 0$ mm is depicted in Fig. 5.4(d) with the solid black line. Due to the limited required aperture, the bottom effective medium, as shown in Fig. 5.4(a), is confined within $R_{\text{bot}} = 1.7$ mm, where the power level drops down to around -10 dB. Theoretically, the bottom effective medium is expected to compensate for half of the required phase. To that effect, the expected phase profile after propagating through the bottom effective medium at $z = 1$ mm is shown in Fig. 5.4(d) with the dashed blue line. Given the phase difference $\Delta\theta$ between the phase profile at $z = 0$ mm and expected phase profile at $z = 1$ mm, the required refractive index of each ring for the bottom layer follows the standard GRIN lens calculation:

$$n_r = n_{\text{si}} - \Delta\theta / (k_0 h_{\text{EM}}) \,, \tag{5.8}$$

and the simulated output phase profile at $z = 1$ mm is shown in Fig. 5.4(d) with the solid blue line. As anticipated, the spatial phase variation is partially corrected within $R = 1.55$ mm, corresponding to a 0.65π phase variation that agrees with the previously mentioned phase coverage capability. When $R > 1.55$ mm, difference occurs due to the insufficient phase coverage capability. The top effective medium lens, as shown in Fig. 5.4(b), is designed to further correct the wavefront based on the intermediate phase profile at $z = 1$ mm and the expected constant phase profile at the top of the silicon at $z = 2$ mm is shown as the red dashed line in Fig. 5.4(d). To simplify the top lens hole pattern, three unit cell rings are combined together when $n_{\text{r}} > 3.25$ and two unit cell rings are combined together when $3 < n_{\text{r}} < 3.25$. These relative refractive indexes are under the condition of tapered holes. The design of the top effective medium follows the same procedure, resulting in a nearly planar phase profile within the range of $R < 1.55$ mm. The output phase profile confirms that a $2 \times 0.65\pi$ spatial phase variation has been corrected by the two effective medium layers. To slightly improve the gain, four additional effective medium rings are obtained through optimization for the top GRIN layer, resulting in an expanded physical aperture to approximately $R_{\text{top}} = 2.6$ mm. The effective refractive indices of these four effective medium rings are 3.24, 3.04, 2.92, and 2.86, arranged from inner to outer rings. To ensure alignment between the top and bottom lenses, an air hole is introduced at the center of both lenses.

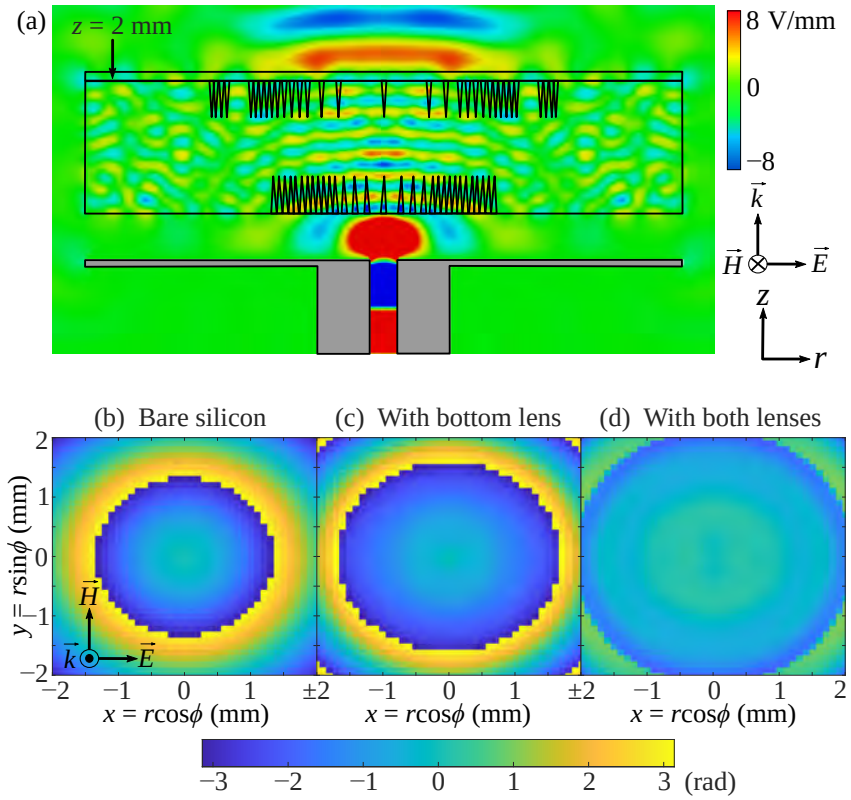

Figure 5.5. Electric-field distributions from CST simulation. (a) Instantaneous E-field amplitude distribution in linear scale from a cross-sectional view. The cutting plane is aligned with the E-plane. Phase distribution of the E-field at $z = 2$ mm for the case of (b) bare silicon, (c) with only the bottom lens, (d) with both the top and bottom lenses.

The antenna structure is further optimized and the final patterns for the bottom and top effective medium lenses are shown in Fig. 5.4(a) and (b), respectively.

Finally, a COC film is placed on the top side of the cavity antenna to assist in silicon-air impedance matching. With a relative permittivity of $\epsilon_r = 2.33$ and a loss tangent of $\tan\delta = 0.0005$ over the WR-3.4 frequency band, COC is chosen as a low-loss material (Nielsen *et al.*, 2009). The ideal silicon-air anti-reflection layer requires a material with a permittivity equal to the geometric mean of the surrounding materials: $\epsilon_{AR} = \sqrt{\epsilon_{si}\epsilon_{air}} = 3.418$ and an effective quarter wavelength thickness of 150 µm. However, considering the gradual permittivity transition from the top effective medium, COC with a slightly lower permittivity is considered acceptable, and a thickness of 100 µm is selected due to availability.

The proposed silicon cavity antenna with actual tapered side walls is simulated in CST. In the simulation, the WR-3.4 waveguide and the metal backing are assumed to be perfect electric conductors, as their non-resonant nature implies negligible losses.

The loss tangent of the COC material ($\tan\delta = 0.0005$) is accounted for, while silicon is considered as a lossless dielectric material. It is worth noting that the roughness of the laser-etched air holes and some resulting compositions might introduce additional losses. A snapshot of the final instantaneous E-field distribution with open space on the top side is shown in Fig. 5.5(a), confirming the wave propagation characteristics mentioned earlier. The 2-D phase profiles at the top of the silicon at $z = 2$ mm are given in Fig. 5.5(b–d), demonstrating the evolution of the phase correction. Progressing from the bare silicon case to the case with bottom lens and finally with both top and bottom lenses, the phase profile becomes increasingly planar. It is worth re-emphasizing that this two-layer topology aims at providing a feasible solution given fabrication limitations. Thus, it is not possible to obtain an arbitrarily high gain due to a limited aperture size imposed by a limited phase coverage in each effective medium layer. Nevertheless, the design principle relies on the phase correction occurring within the central area ($R < 1.55$ mm) where most of the power resides, which leads to a broad bandwidth due to the absence of phase wrapping requirements.

5.3 Fabrication and measurement

The silicon cavity antenna is fabricated by a laser micromachining technique. A 2-mm thick float-zone, 4-inch silicon wafer, with a resistivity of 20 kΩ-cm is first diced to 9×9 mm^2 using a dicing saw (DISCO DAD 321-NanoFab) machine. In the laser micromachining process, a Circuit CAM 7 Laser Plus software is used to convert the layout of the blind cylindrical air holes to machine readable template for a DCT laser micromachining tool to trace the layout. To drill a depth of approximately 600 µm, the laser parameters including average power, frequency and offset/time are optimized to 75% of 9.1 W, 50 kHz, 0.05 mm/time and run 12 times. The bottom face is aligned by using a tracer to find the center wafer piece from its edge. The fabricated silicon cavity antenna sample is illustrated in Figs. 5.6(a) and (b). The air hole diameter is fixed at 70 µm and its density increases periodically towards the outer radius, as depicted in both the top view and bottom view. To ensure the quality of the air holes, micro-computational-tomography scanning with 10 µm resolution is conducted, providing a cross-sectional view of the structure as shown in Fig. 5.6(c). The cross-section reveals an approximate tapered angle of around 3.6°, which agrees well with the previous estimation. The cavity antenna is integrated with a WR-3 hollow waveguide using a 3-D printed COC holder, as shown in Fig. 5.7(a). The printed COC holder creates an air

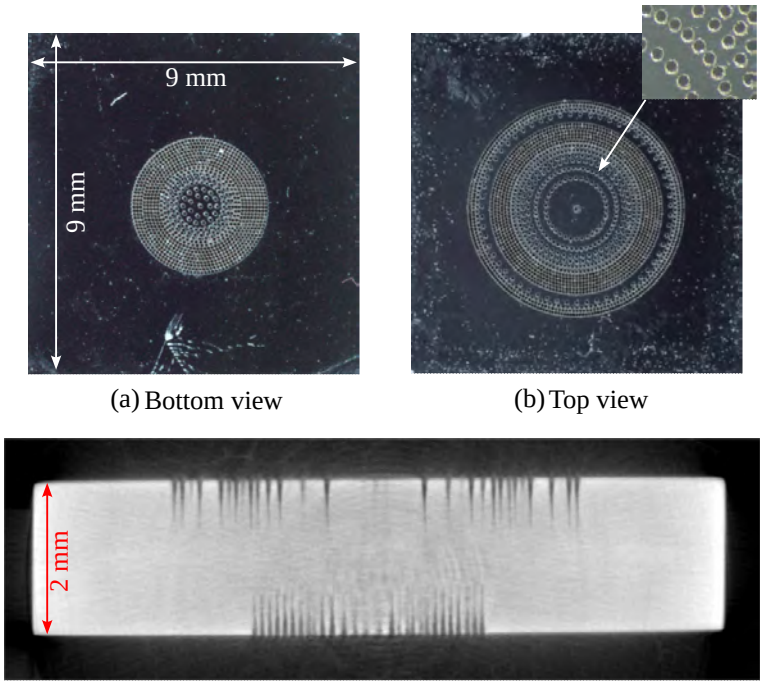

(a) Bottom view (b) Top view

(c) Cross-sectional view

Figure 5.6. Fabricated silicon cavity antenna sample. (a) Bottom lens. (b) Top lens. The inset displays a microscopy image highlighting the holes. (c) Cross-sectional view of the sample. The sample is subjected to a micro-computational-tomography scanning with a 10 µm resolution to generate a 3-D model. The cutting plane is chosen to provide a clear depiction of the hole cross-sections.

gap of 720 µm, which is close to the anticipated 700 µm. A COC film of 100 µm is placed on top of the silicon wafer to mitigate the silicon-air impedance mismatch. Figure 5.7(b) shows the final device under testing (DUT). The cavity antenna is securely clamped in the holder, which is then fixed to the waveguide flange using screws.

The radiation pattern measurement setup is shown in Fig. 5.7(c). A vector network analyzer Keysight N5222B with VDI extension modules operating from 220–330 GHz is used to conduct the measurement. The silicon cavity antenna is positioned at a distance of 450 mm from the receiver horn to ensure far-field conditions, approximately occurring beyond 200 mm. On the transmitter side, the rotating stage is set to an angular resolution of 0.5° for a rotation range of ±35° to measure the *H*-plane pattern. Two waveguide twists are added on both transmitter and receiver sides to measure the *E*-plane pattern. The measured transmission magnitude is compared to a VDI WR-3.4 diagonal horn antenna to calculate the gain. Due to the strong free-space path loss and line-of-sight propagation, the signal decays very rapidly and it is not strictly necessary to build an anechoic environment like in the microwave range.

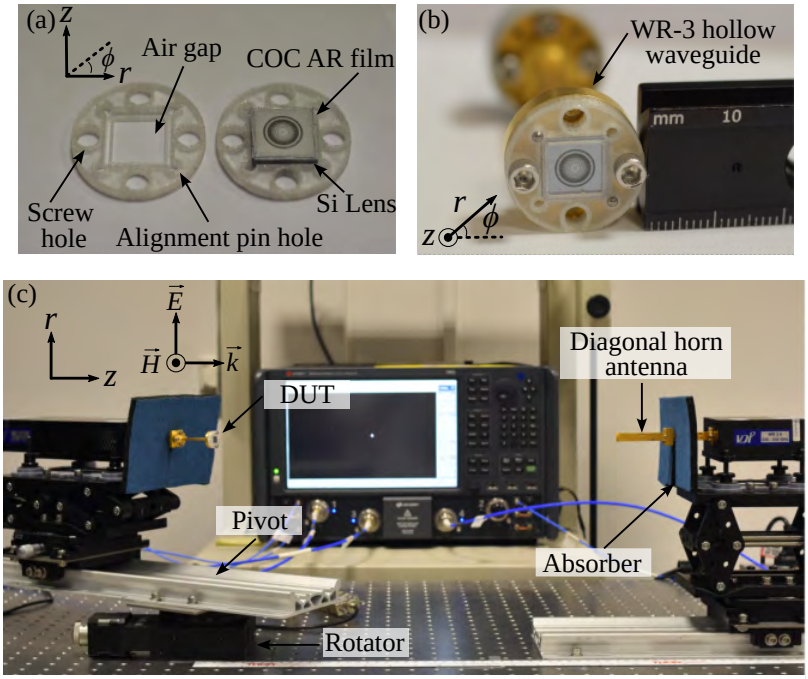

Figure 5.7. Radiation measurement setup. (a) Silicon cavity antenna with the 3-D printed COC holder. The COC film is placed on the top side of the silicon cavity antenna. (b) The holder securely clamps the COC film on top of the silicon substrate, and both are firmly held together with the waveguide flange using screws. (c) Measurement setup. The device under testing (DUT) is placed on the rotator with an angular resolution of 0.5°. The emitted radiation from the DUT propagates through free-space over a distance of around 450 mm, and is captured by the diagonal horn antenna.

As shown in Fig. 5.8(a), the measured maximum broadside realized gain, accounting for reflections and material losses, is 19.1 dBi at around 275 GHz, and a large 3-dB bandwidth of 29% can be observed between 228–308 GHz. Compared with the simulation, it is observed that the broadside gain at lower frequencies from 230 to 250 GHz exceeds the simulated values while at higher frequencies from 290 to 310 GHz, it slightly falls below the expected values. Considering the lens physical aperture size of R_{top} = 2.6 mm, the maximum antenna efficiency observed at 275 GHz is approximately 36%. This antenna efficiency accounts for the aperture field distribution, reflection loss, and material losses (IEEE Std 145-2013, 2014). The measured reflection coefficient is lower than −10 dB over the entire band, as indicated in Fig. 5.8(b). The measured reflection coefficient is slightly lower than the simulation, potentially because of the losses from the hollow waveguide (Alonso-delPino *et al.*, 2019). Additionally, simulations indicate that the COC anti-reflection layer enhances gain and reduces the reflection coefficient. Figures 5.8(c–e) present a comparison of the radiation patterns at 250 GHz, 275 GHz and 300 GHz, respectively. At the center frequency of 275 GHz, the 3-dB beamwidth

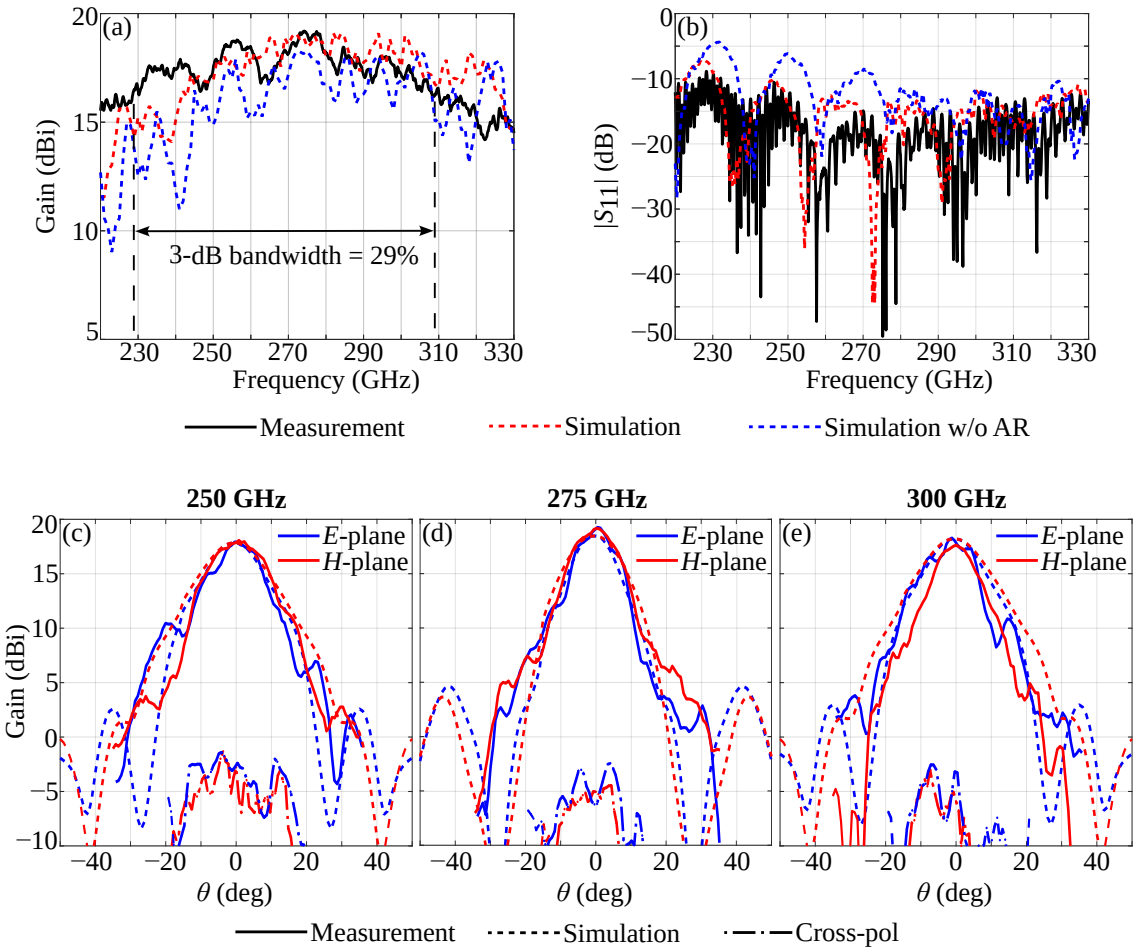

Figure 5.8. Radiation measurement and simulation results. The measured gain is calculated by comparing the transmission magnitude to a diagonal horn antenna. (a) Broadside gain. (b) Reflection coefficient. (c-e) Radiation patterns at 250 GHz, 275 GHz and 300 GHz, respectively.

for both *E*- and *H*-planes are around 14°. Measured sidelobes can be observed in the *E*-plane, potentially caused by the slight misalignment between the silicon lens and the waveguide feed. Due to symmetry, the cross-polarization patterns are expected to approach mathematical zero around broadside. The measured cross-polarization radiation patterns validate this characteristic, with levels approximately 20 dB lower than the maximum gain. It should be noted that the measured results are not expected to precisely match the simulation due to the imperfections in fabrication, such as the non-uniform tapered side walls and contaminants due to laser exposure. It is likely that these factors will cause asymmetrical radiation patterns and shifted broadside response. Nevertheless, the measured results indicate a high-gain, wideband performance and the differences with simulation results are within an acceptable range.

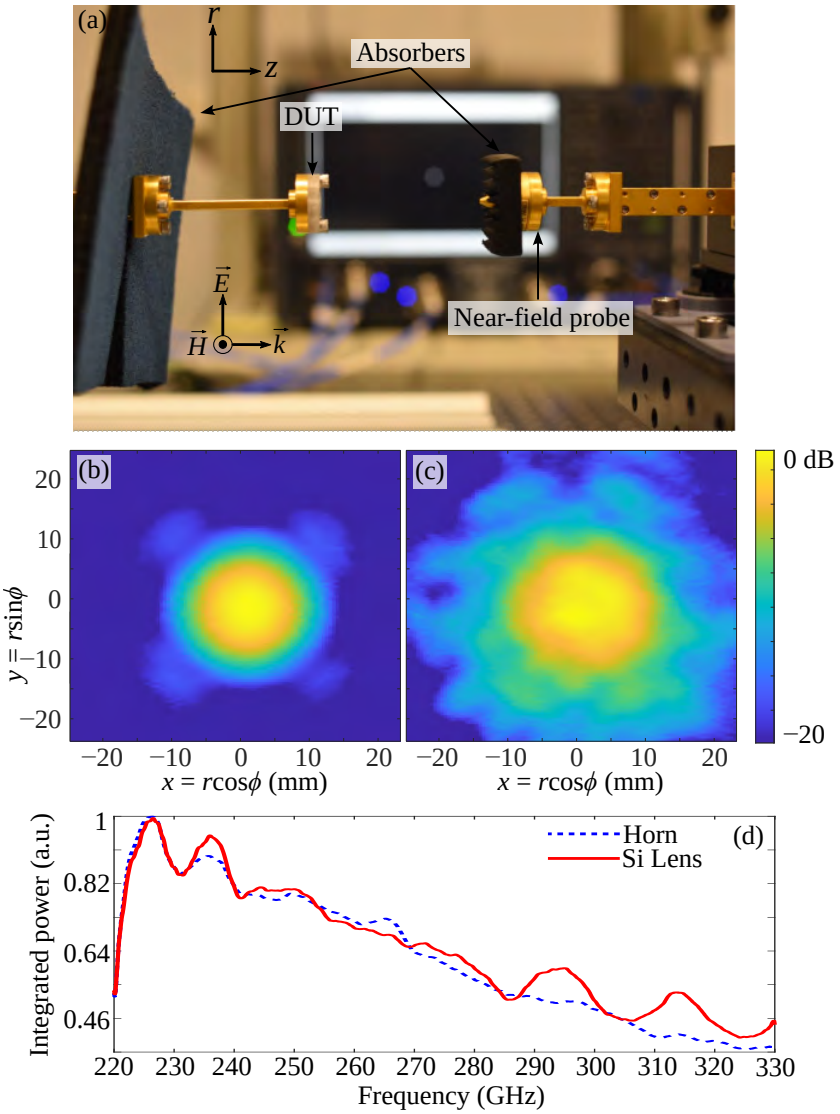

Figure 5.9. Near-field scanning measurement. (a) Measurement setup. The silicon cavity antenna is placed at the left as the source and the near-field probe is placed at the right for complex amplitude detection. (b, c) Measured intensity distribution at 275 GHz of the diagonal horn antenna and the silicon cavity antenna, respectively. The intensity distributions are normalized to their own maximum values in log scale. (d) Integrated measured power. The integrated power is calculated before the normalization in (b) and (c).

One general concern with the cavity antenna is the radiation loss in undesired directions resulting from multi-reflections inside the cavity. Additionally, the use of high-resistivity silicon for the antenna is aimed at minimizing material-related losses. However, as mentioned earlier, the roughness of the air holes and the resulting composites might introduce additional losses, which could affect the radiation efficiency. To examine the beam efficiency near broadside, a near-field scan is conducted to compare the integrated

measured power of the cavity antenna to that of the standard diagonal horn antenna. As shown in Fig. 5.9(a), the near-field probe connected with the receiving waveguide is placed at around 50 mm from the cavity antenna. The receiving unit is mounted on a two-axis motorized stage for scanning an area of 50×50 mm^2 with a spatial resolution of 0.5 mm. Figures 5.9(b) and (c) present the scanned profiles for the horn antenna and the cavity antenna at 275 GHz, demonstrating that the cavity antenna exhibits a nearly Gaussian beam profile with a Gaussicity (Filipovic *et al.*, 1993) of 94% compared to a Gaussian beamwidth w = 15.5 mm at the scanning location. The Gaussicity confirms that the aberration introduced by the lens is low and that the silicon lens antenna is applicable to various sensing and imaging applications. In comparison, the horn's Gaussicity is 97% with a Gaussian beamwidth w = 9.5 mm. The larger beamwidth of the cavity antenna is due to a more diverging beam. Noting that the horn is 30 times longer compared to the cavity antenna height. Slight asymmetry is also observed from Fig. 5.9(c), which is consistent with the corresponding asymmetrical radiation pattern of Fig. 5.8(d). Importantly, as can be seen from Fig. 5.9(d), the integrated power from the diagonal horn antenna and the proposed cavity antenna are nearly identical, suggesting negligible absorption losses and insignificant undesirable leakage in this antenna.

Table 5.1 compares the state-of-the-art integrable lens antennas. The hemispherical lens made of Rexolite (ϵ_r = 2.53) (Konstantinidis *et al.*, 2017) achieves a high gain but has relatively large size and high profile. Since the lens is directly fitted to the waveguide, the effective aperture is limited, resulting in relatively low aperture efficiency. In contrast, the hemispherical lens made of silicon (Alonso-delPino *et al.*, 2021) significantly reduces the device size and height. It achieves similar peak gain and bandwidth compared to

Table 5.1. Comparison on the state-or-art integrable lens antennas. HPBD: half power bandwidth.

Reference	Structure	Freq. (GHz)	Size (λ^2)	Height (λ)	Peak-Gain (dBi)	HPBD	Dielectric loss (dB)	Antenna Efficiency
Konstantinidis *et al.* (2017)	Rexolite hemispherical lens	293	302	20.6	30	30%	2	26%
Alonso-delPino *et al.* (2021)	Silicon hemispherical lens	550	69	13	28.2	35%	~ 0	78%
Wu *et al.* (2019a)	3-D printed Fresnel lens	300	314	9.7	27.4	15%	2.8	15%
Medrar *et al.* (2021)	Metasurface lens	330	53	5	20.6	26%	1.8	18%
This work	Silicon cavity lens	275	18	2.6	19.1	29%	~ 0	36%

Konstantinidis *et al.* (2017), while the aperture efficiency is significantly improved owing to the resonant cavity design. To further reduce the device profile, discrete Fresnel lenses can be realized through 3-D printing (Wu *et al.*, 2019a) or using metasurfaces (Medrar *et al.*, 2021). However, these methods lead to a degraded performance in terms of bandwidth and peak gain, respectively. Moreover, the non-negligible dielectric loss has a noticeable effect, resulting in reduced antenna efficiency. In the present work, the proposed silicon cavity antenna provides the smallest device profile among the references, with a height of only $2.6\lambda_0$. Although the peak gain is lower, it is mainly constrained by the feasible aperture size due to the limited etching depth and tapered side walls. However, a broadband performance is achieved as a trade-off. The negligible absorption losses contribute to an appreciable antenna efficiency for the proposed cavity antenna. Furthermore, the need for an expensive vapor deposition coating process is eliminated by using a simple COC film for anti-reflection purposes.

5.4 Wireless communications demonstrations

To illustrate the real-world capabilities of the cavity antenna in terahertz communications, a comprehensive bit-error-rate (BER) testing experiment is conducted. Furthermore, the transmission of uncompressed 4K-resolution video data is demonstrated.

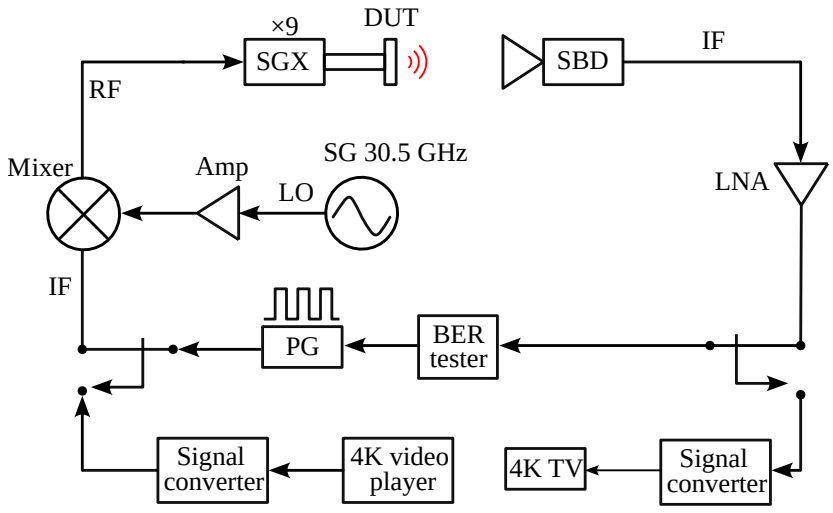

Figure 5.10. Communications measurement schematic. PG: pattern generator. IF: intermediate frequency. SG: signal generator. LO: local oscillator. RF: radio frequency. Amp: amplifier. SGX: signal generator extension module. SBD: Schottky barrier diode. LNA: low noise amplifier. BER tester: bit-error-rate tester.

These practical experiments solidly validate the antenna's performance in relation to dispersion and highlight its potential applications in high-speed terahertz communications systems. The schematic diagram of the communications measurement is shown in Fig. 5.10. On the transmitter side, a baseband signal is generated from the BER tester pattern generator or a 4K-resolution video player. This signal modulates an amplified local oscillating signal of 30.5 GHz from the signal generator with on-off keying (OOK). The modulated signal is then up-converted to the terahertz frequency of around 275 GHz by a VDI signal generator extension (SGX) module. On the receiver side, a diagonal horn antenna with a Schottky barrier diode (SBD) is employed to capture and retrieve the modulating data from the received terahertz signal. The de-modulated data signal is then amplified by a low-noise amplifier (LNA). Finally, the data quality is measured by the BER tester, while for video demonstration, the signal can be displayed on a 4K television after a signal converter.

The performance of the proposed cavity antenna is investigated at different transceiver separation distances for transmitting 6 Gb/s pseudorandom binary sequence (PRBS) data with a data length of 2^{13}. The data rate is primarily limited by the BER tester, Agilent J-BERT N4903B. As shown in Fig. 5.11(a), error-free transmission with a BER of less than 10^{-11} has been attained when the transceiver separation is less than 40 mm. This distance is typical for contemporary laboratory-based communications setups where terahertz amplifiers are not available (Samoska, 2011). The inset in Fig. 5.11(a) shows the eye diagram corresponding to a 40-mm separation, which is clearly open for the 6-Gbit/s data. It can be observed from Fig. 5.11(a) that the BER increases more rapidly compared to the horn antenna due to the lower gain of the cavity antenna. The communication performance is generally consistent with the previous gain measurements. Considering that the cavity antenna has 5 dB lower gain than the horn antenna and the hollow waveguide incurs approximately 1 dB loss, at the same BER level, i.e., 10^{-7}, the separation distance of the cavity antenna should be half that of the horn antenna, according to Friis transmission equation. As shown in Fig. 5.11(b), the video demonstration of uncompressed 4K video signal transmission under a 30-mm transceiver separation at a bit rate of 6 Gb/s is performed.

5.5 Conclusion

In this chapter, a planar high-gain cavity antenna based on double-sided effective medium lenses has been presented. The fabrication process involves direct laser etching

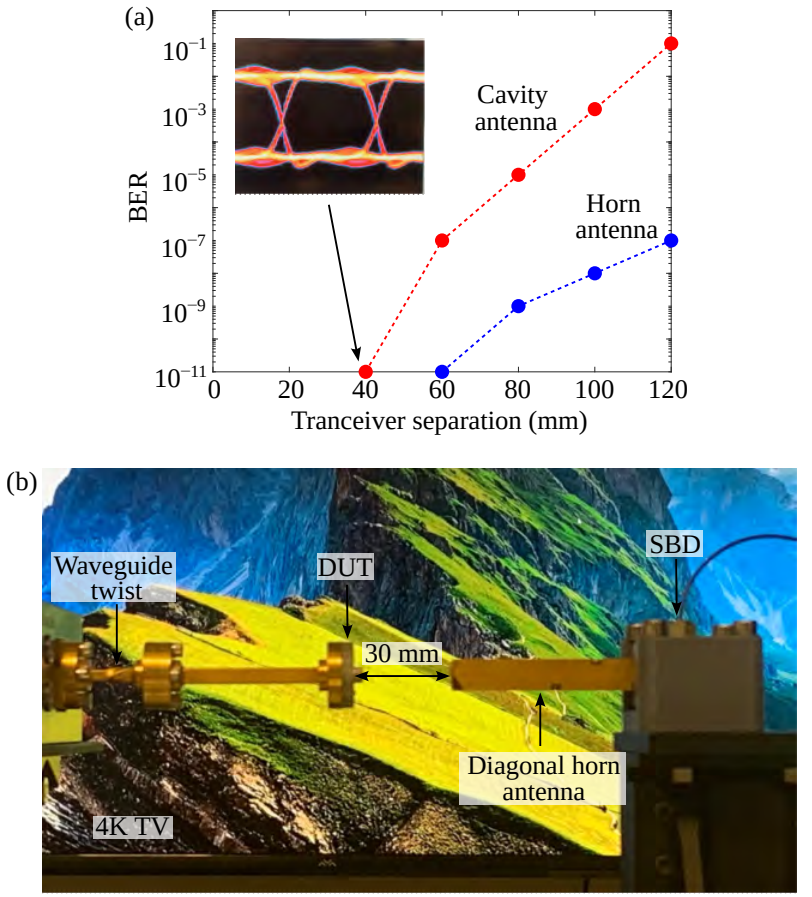

Figure 5.11. Communications measurement results. (a) Measured BER as a function of transceiver separation distances. The inset shows the eye diagram at the distance of 40 mm. (b) 4K-resolution video transmission demonstration. The cavity antenna with a waveguide twist is placed at the left as the transmitter and the SBD with a diagonal horn is placed at the right for envelope detection. The waveguide twist helps aligning the E-field with the SBD. The background depicts a static image of a successful video transmission.

to create blind air holes on a high-resistivity silicon wafer. By controlling the density of air holes, the effective relative permittivity can be spatially adjusted. The achieved hole depth is limited by a tapered angle of around 3.6°. To accommodate the resultant insufficient phase coverage, an effective medium is created on both sides of the wafer for collective phase correction and an air gap is added between the cavity antenna and the waveguide to expand the aperture. Although there are slight discrepancies between the measured and simulation results due to fabrication imperfections, the measured performance confirms high-gain and wideband characteristics. A maximum gain of 19.1 dBi has been measured at around 275 GHz with a 3-dB bandwidth of around 29%. The proposed silicon cavity antenna has the height of only $2.6\lambda_0$ and eliminates the

need of complex anti-reflection coating. The cavity antenna has been further tested for terahertz wireless communications, demonstrating an error-free transmission. Future investigations will focus on improving etched air-hole quality and exploring possibilities at higher frequencies, where one effective medium may be sufficient for phase correction while the other effective medium may serve a different purpose. This planar cavity antenna is particularly suitable for array-level applications and mass production, given that the fabrication process remains unchanged across a large aperture and the planar profile is compatible with a flat anti-reflection film.

Chapter 6

Terahertz frequency-diverse antenna for direction of arrival estimation

THE IEEE 802.15.3d standard for point-to-point wireless terahertz communications is defined to support high-capacity channels. By nature, terahertz signal transmission requires line-of-sight propagation and terahertz communications operates within a challenging power budget limitation. Therefore, accurate and efficient direction of arrival (DoA) estimation for maximizing received power becomes paramount to achieve reliable terahertz communications. In this chapter, a frequency-diverse antenna with a machine learning-based approach utilizing convolutional neural networks (CNNs) is proposed to estimate DoA in the terahertz communications band. The antenna is deliberately designed to break symmetry, generating quasi-random radiation patterns, while the CNN captures the relationship between the radiation patterns and their respective angles of arrival. Based on experiments, the DoA estimation results converge to a minimum validation mean squared error (MSE) of 3.9° and root mean squared error (RMSE) of 1.9°. The estimation efficacy is further substantiated by a consistent performance demonstrated across diverse scenarios, encompassing various obstacles and absorbers around the propagation path.

6.1 Introduction

To meet the stringent link budget requirements for terahertz communications, highly directional and efficient antennas are essential. For instance, to achieve real-time 10 Gb/s transmission with a sub-terahertz frequency of 120 GHz, a pair of standard horn antennas with a gain of 23.3 dBi, which corresponds to a half-power beamwidth (HPBW) of approximately 12°, was employed to support an error-free transmission over a distance of 4.2 m (Takahashi *et al.*, 2013). Practical long-distance communications, such as over 1 km, requires ultra-high antenna gains, reaching almost 50 dBi (Hirata *et al.*, 2012). The substantially higher gain requirement further narrows the HPBW. In such cases, the accurate estimation of the direction of arrival (DoA) of signals emerges as a critical aspect for optimizing the performance of terahertz communications links, as even minor deviations in alignment can lead to pronounced performance degradation.

The basic positioning and localization framework in the fourth-generation (4G) long term evolution (LTE) positioning architecture is based on the receiver's measurements of reference signal time difference from neighboring base stations (Yeh *et al.*, 2023). The major limitation with this architecture, however, is its inherent time sensitivity, requiring precise synchronization. Classical millimeter-wave DoA relies on array-based architectures on the receiver side. These architectures employ either mechanical (Alonso-delPino *et al.*, 2021) or electronic (Abielmona *et al.*, 2011; Paaso *et al.*, 2017) beam steering to scan the composite aperture for channel information collection. However, mechanical-scanning antennas are not suitable for real-time estimation, and electronic-scanning phased arrays are not viable in the terahertz frequency range due to increasing ohmic loss and poor performance of phase shifters (Headland *et al.*, 2018a). Recent advancements in hybrid scanning technology (Bosma *et al.*, 2022b) have allowed for a reduction in the number of required lossy components. Nonetheless, array-based structures inherently tend to be bulky and complex. As an alternative, a recently proposed frequency-diverse antenna operating from 27–29 GHz has garnered significant attention (Abbasi *et al.*, 2020). The DoA estimation was based solely on a single antenna, which generated quasi-random radiation patterns within the operating frequency range. Further research suggests that the frequency-diverse antenna can also support multi-source detection and reconfigurable dynamic aperture (Hoang *et al.*, 2021). These antennas also find applications in imaging systems, where the distinct radiated fields illuminate the scene sequentially to reconstruct the image (Fromenteze *et al.*, 2015). However, the effectiveness of this algorithm is restricted to a relatively narrow bandwidth due to the

assumption of unchanged phase profile on the projection plane (Yurduseven *et al.*, 2019). Additionally, mathematical DoA models are limited by any mismatch between assumed and real environment scenarios highlighting the need for an intelligent and adaptive method of DoA estimation.

As such, intelligent DoA estimation algorithms have been studied and developed. They typically involved machine learning (ML) algorithms for accurate and quick DoA estimations. The DoA estimation also has a variety of applications outside of wireless communications, such as for signal source number estimation and signal processing (Ge *et al.*, 2021). ML-based DoA for signal processing has been studied for applications of radar and sonar where Xiang *et al.* analyzed amplitude-phase distortions of multi-path signals in low altitude target scenarios (Xiang *et al.*, 2019). Xiang *et al.* also proposed a supervised deep neural network (DNN) model to mitigate the effects of phase distortion thereby consequently improving DoA estimations (Xiang *et al.*, 2019). Additionally, ML-based DoA approaches have been proposed for RF sources received by an array of antennas. Goodman *et al.* formulated the DoA estimation problem as an array calibration learning process where a deep learning model was used to learn a parameterized model of the receiver antenna array for accurate DoA estimations (Goodman *et al.*, 2019). Moreover, direct DoA angle estimations were proposed where an artificial neural network was trained to learn the direct azimuth and elevation arrival angles of a signal source (Agatonovic *et al.*, 2013). Unlike previous studies which approached the enhancement of DoA estimation through intermediate steps, this work focused on the direct prediction of DoA angles, which prevented the failure owing to mismatch between assumed and real environments, making such works vital for accurate DoA estimation in real communications scenarios. Furthermore, that work trained and analyzed the DoA data at the microwave frequency range, with 17 frequency points from 2.41 GHz to 2.47 GHz. Nonetheless, no work has addressed DoA challenges with ML in the context of terahertz communications with such a broad bandwidth until now.

In this chapter, a frequency-diverse antenna with ML-based analysis is proposed to estimate the DoA of signals in the terahertz communications band. To the best of the author's knowledge, this is the first work which presents an application of ML-based DoA estimation for terahertz communications. The antenna is composed of an oversized cavity box, metallic scatterers, and a three-dimensional (3-D) printed dielectric lens to break the structural symmetry. A convolutional neural network (CNN) is utilized to

analyze the amplitude of radiation patterns of the IEEE 802.15.3d communications band spanning from 252 to 325 GHz (IEEE Std 802.15.3d-2017, 2014) and learn the non-linear mapping function between the radiation patterns and their respective angles of arrival. During measurement, uncorrelated spectra have been observed across various receiving angles, and the DoA estimation with ML demonstrated high accuracy for distinct scenarios. [1]Detailed analysis of the frequency-diverse antenna and the ML algorithm are provided in Section 6.2. The fabrication and measurement results is included in Section 6.3. Section 6.4 presents the ML-based DoA prediction and Section 6.5 concludes the article.

6.2 Operation principle

6.2.1 Antenna design

In order to achieve accurate DoA estimation of terahertz communications waves, it is essential for the frequency-diverse antenna to exhibit distinct radiation patterns across the desired frequency range. It should be clarified that the designed antenna operates as a receiver, while it is simulated as a transmitter due to reciprocity. Due to the angular (radiation pattern) diversity, the received signal spectra will be unique at different angles of arrival, allowing for the estimation of DoA. To align with the IEEE 802.15.3d channel plan (IEEE Std 802.15.3d-2017, 2014) for communications, the frequency range of interest spans from 252 GHz to 325 GHz. Simplifying the design process, a comparison of 37 radiation patterns is undertaken, covering the frequency range of 252–325 GHz with a resolution of 2 GHz. The correlation between radiation patterns quantifies the performance of the frequency-diverse antenna. High correlation coefficients suggest that the received signal spectra might share similarity with different angles of arrival and therefore make it challenging to distinguish the DoA. To minimize the correlation between radiation patterns at different frequencies, the design of the DoA antenna should intentionally break symmetry.

As depicted in Fig. 6.1, the DoA estimation antenna comprises an open oversized metallic cavity box with a size of $45 \times 45 \times 15$ mm^3, integrated with a WR-3 waveguide that operates between 220–330 GHz. The positioning of the waveguide is intentionally

[1]Sections related to machine learning, including Section 6.2.2 and Section 6.4, are mainly contributed by Mariam Abdullah.

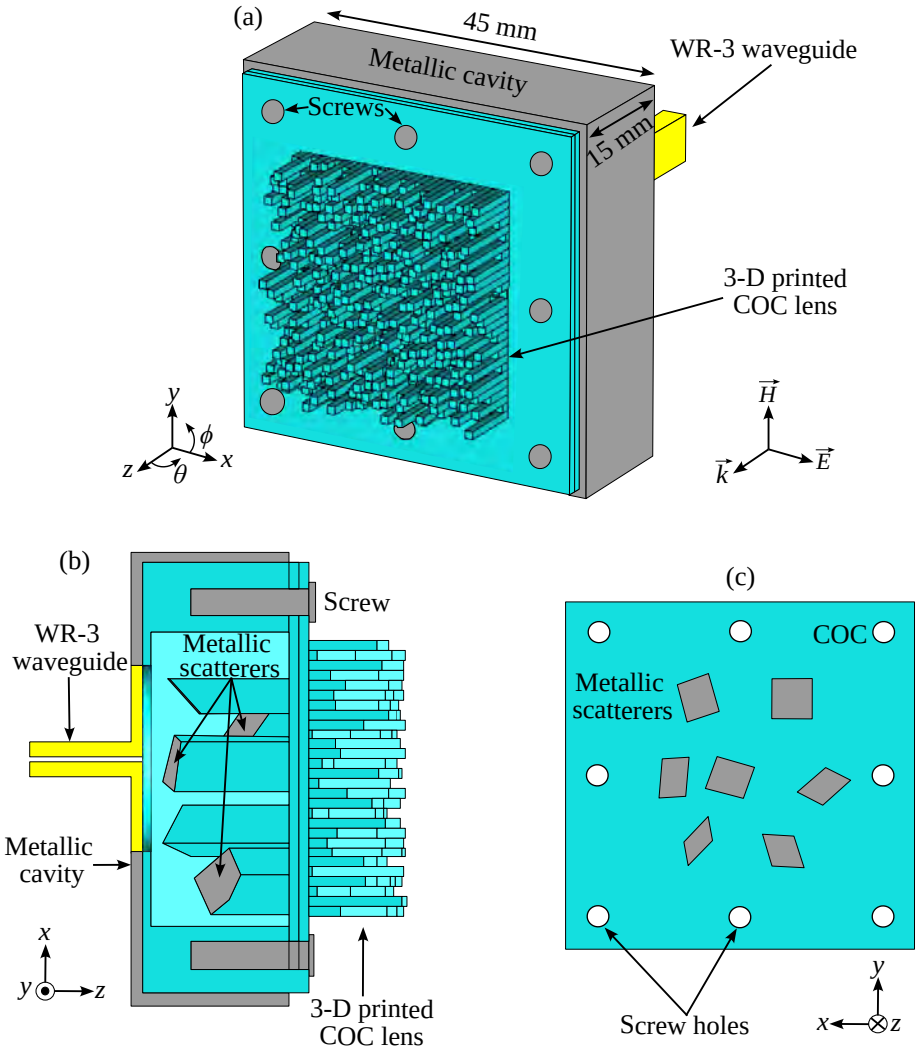

Figure 6.1. Frequency-diverse antenna structure. (a) Antenna Schematic. The oversized aluminium cavity has a size of $45 \times 45 \times 15$ mm^3, with an integrated WR-3 waveguide feed. The cyclic olefin copolymer (COC) lens is composed of 3-D printed pillars each of 1×1 mm^2, with random heights from 0–10 mm. (b) Cross-sectional view. Metallic scatterers with arbitrary orientations are placed inside the metallic cavity. (c) Metallic scatterers position from the bottom view.

shifted from the aperture center, structurally breaking the symmetry of the antenna setup. Given the requirement for distinct radiation patterns across a substantial fractional bandwidth of over 25%, which is much larger than typically encountered in the millimeter-wave range, multiple metallic scatterers of arbitrary orientations are suspended inside the cavity box to further increase complexity of the cavity boundaries. Terahertz waves from the waveguide experience multiple reflections from these metallic scatterers and the side walls, effectively further breaking the symmetry. It is worth noting that the middle scatterer should be properly placed at a sufficient distance from

the waveguide to keep the reflection coefficient lower than −10 dB. Furthermore, a 3-D printed lens, comprising 1×1 mm^2 square pillars with random heights ranging from 0–10 mm, is added to the cavity box to further disrupt symmetry. The height is commensurate with the wavelength of around 1 mm in this frequency range. As such, the lens introduces fuzzy constructive or destructive interference patterns, resulting in gain enhancement or reduction at random directions. To avoid dielectric losses that occur with conventional 3-D printed terahertz antennas (Yi *et al.*, 2016; Wu *et al.*, 2019b), cyclic olefin copolymer (COC) with a relative permittivity of $\epsilon_r = 2.33$ and a loss tangent of $\tan\delta = 0.0005$ over the desired frequency band is chosen as a low-loss material for 3-D printing.

The frequency-diverse antenna is simulated in CST Microwave Studio. The 3-D radiation patterns at 300 GHz and the adjacent 302 GHz are depicted in Figs. 6.2(a) and (b), respectively. These patterns exhibit maximum gains of approximately 13 dBi, with no clear main lobe discernible. The 3-dB beamwidth for gain maxima exceeding 10 dBi typically falls below 2°. Notably, the radiation patterns exhibit a distinct lack of symmetry, and there is no significant correlation observed between adjacent frequency bins.

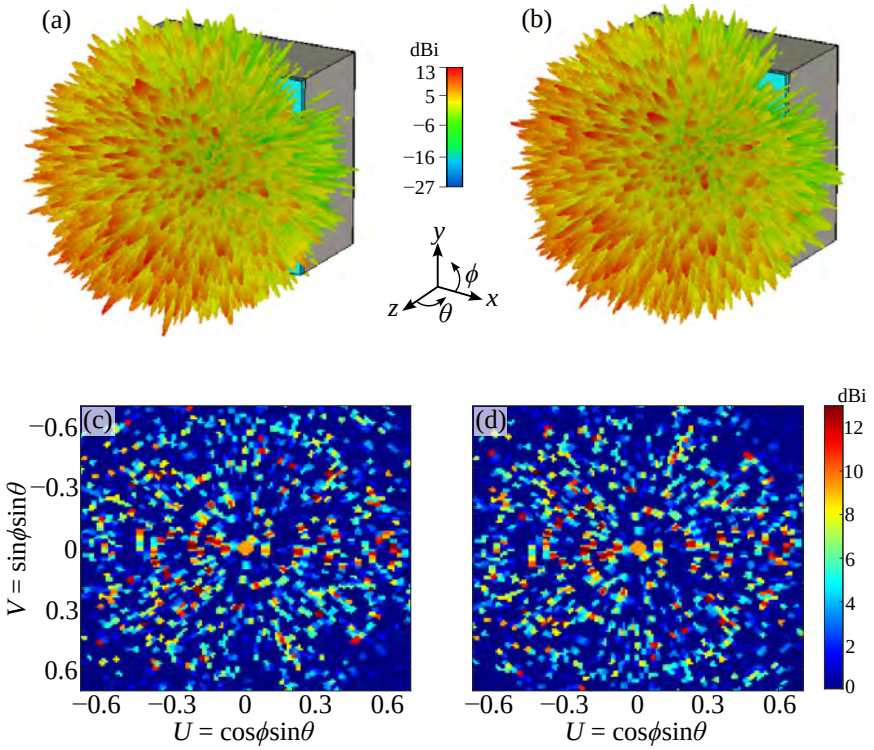

Figure 6.2. Simulated radiation patterns. (a, b) 3-D radiation patterns at 300 GHz and 302 GHz, respectively. (c, d) Orthographically projected two-dimensional (2-D) radiation patterns at 300 GHz and 302 GHz, respectively.

6.2.1 Antenna design

The radiation patterns are orthographically projected to create two-dimensional (2-D) representations, at 300 GHz and 302 GHz as shown in Figs. 6.2(c) and (d). The statistical uniformity of these random patterns can be estimated by averaging the *E*-field patterns

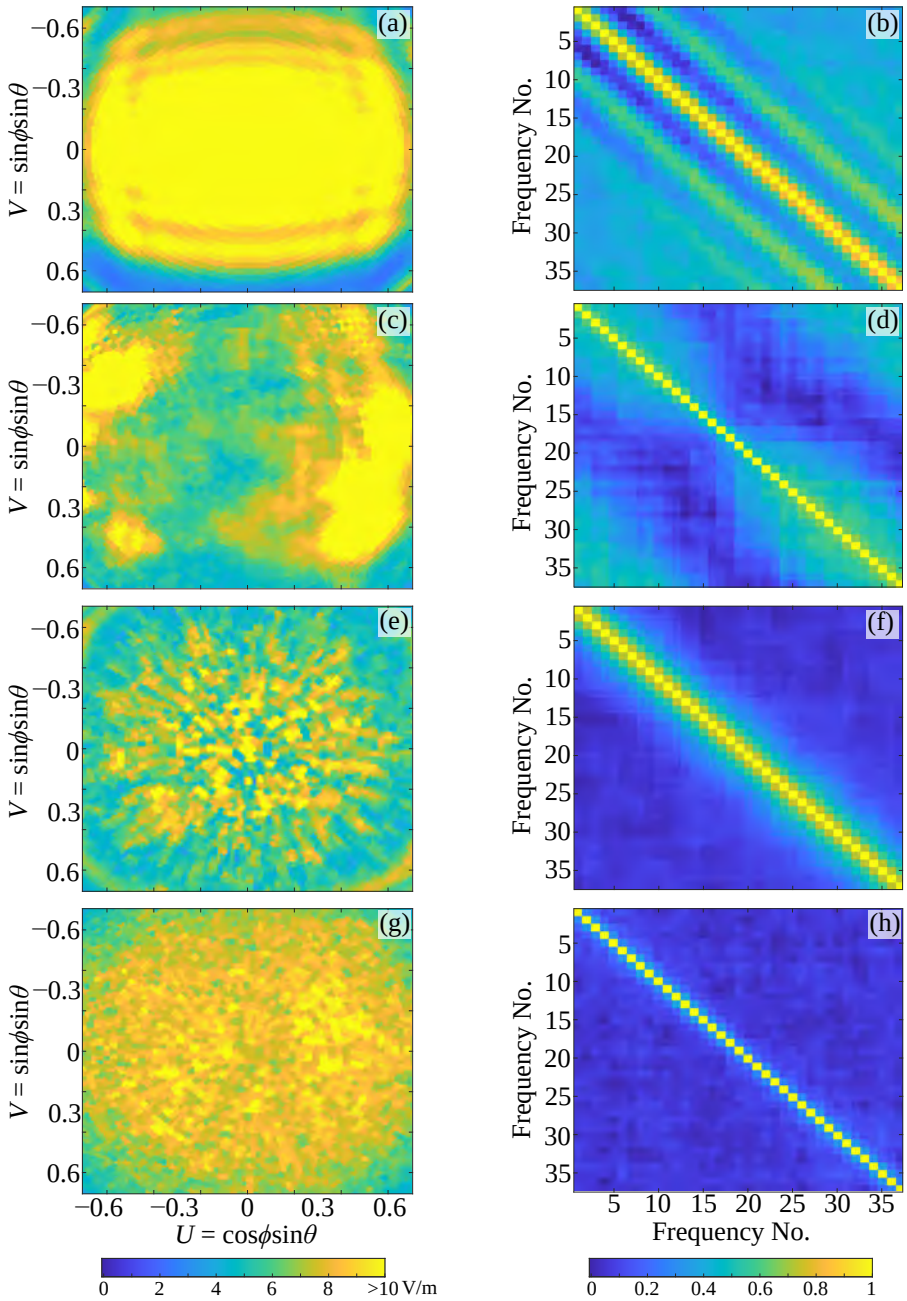

Figure 6.3. Uniformity and correlation of radiation patterns. Orthographically projected 2-D *E*-field patterns averaged from 252–325 GHz (left column), and correlation coefficients of 37 radiation patterns (right column). (a, b) With cavity (c, d) With cavity and scatterers. (e, f) With 3-D printed COC lens. (g, h) With cavity, scatterers and 3-D printed COC lens.

over the frequency axis, which can be expressed by:

$$\mathbf{E}_{\text{avg}} = \frac{1}{N}(\mathbf{E}_{f_1} + \mathbf{E}_{f_2} + \cdots + \mathbf{E}_{f_N}) \,. \tag{6.1}$$

Figure 6.3(a) displays the averaged *E*-field pattern with only the cavity. Since the cavity is oversized, the pattern is mainly determined by the radiation from the small waveguide aperture, which has a large symmetric beamwidth. The resultant averaged *E*-field pattern therefore confirms the expected uniformity. However, the correlation coefficients between the patterns at different frequencies are consistently high due to the absence of symmetry breaking, as shown in Fig. 6.3(b). Figures 6.3(c) and (e) illustrate the averaged *E*-field with only the cavity and scatterers, and with only the 3-D printed COC lens, respectively. It is evident that the combination of the cavity and the scatterers disrupts the propagation path, and that the 3-D printed lens enhances the randomness of radiation in various directions. Nonetheless, hot-spot areas are still apparent, and the resultant patterns lack uniformity. Due to the structural asymmetry, the correlation coefficients across the communications band, as shown in Figs. 6.3(d) and (f), are significantly lower than in the cavity-only case discussed previously. The proposed design, which combines all aforementioned components, results in a considerably more uniform pattern, as shown in Fig. 6.3(g). The calculated correlation coefficients, as shown in Fig. 6.3(h), indicate low correlation between adjacent frequency bins, typically around 0.3. Correlation with other frequencies is almost negligible. The evolutionary progress of the proposed antenna design firmly validates its uniformity across different angles of arrival, with radiation patterns that distinctly differ from each other across a broad fractional bandwidth of over 28%. In practical measurement, the diagonal horn antenna used as a transmitter has a 3-dB beamwidth of around 10° at 325 GHz. With the ML-based analysis to be discussed in Section II-B, such low correlation coefficients are expected to support DoA prediction with an angular precision better than half of the minimum 3-dB beamwidth, i.e., approximately 5°.

To further elaborate on the operational principle, Figs. 6.4(a, b) show the averaged *E*-field pattern and the correlation coefficients for a conventional WR-3 diagonal horn antenna. Due to the frequency-independent and symmetric radiation pattern, a clear hot-spot area can be found at the center, and the correlation between radiation patterns is consistently high, mostly over 0.95. The lack of randomness results in similar directivity profiles at different angles, as shown in Fig. 6.4(c). Consequently, the DoA estimation becomes impossible for a horn antenna, and typically requires additional mechanical scanning. In contrast, Fig. 6.4(d) shows the directivity profiles at different azimuthal

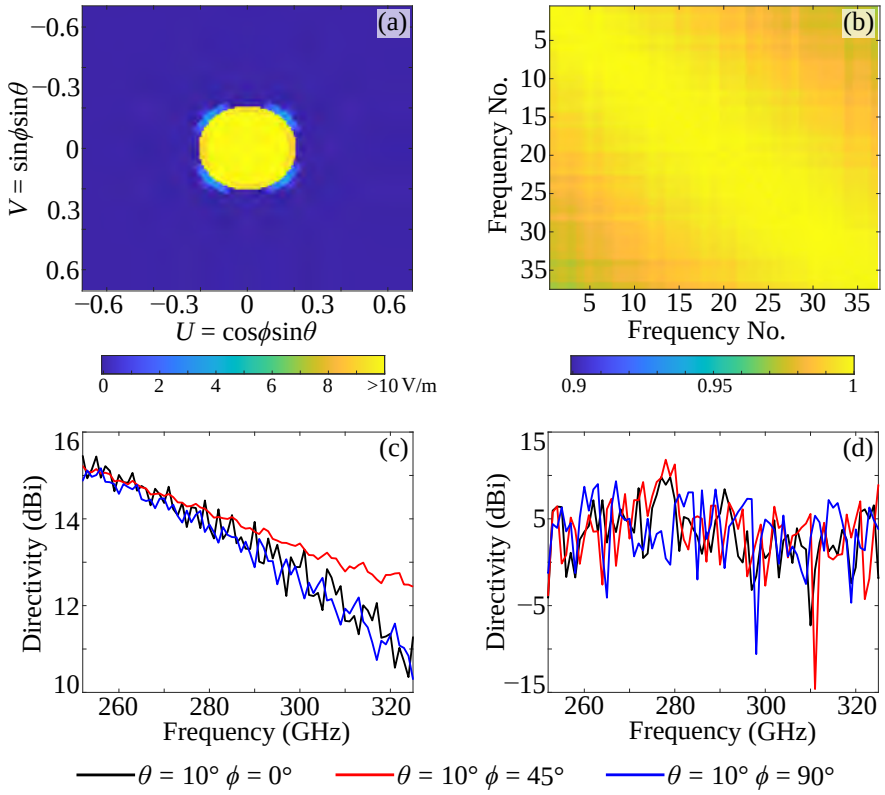

Figure 6.4. WR-3 diagonal horn antenna performance comparison. (a) Orthographically projected 2-D *E*-field patterns averaged from 252–325 GHz. (b) Correlation coefficients of 37 radiation patterns. Note that the scale of the colormap is different from Fig. 6.3 due to higher correlation. (c, d) Directivity at different azimuthal angles for the horn antenna and the proposed frequency-diverse antenna, respectively. The elevation angles remain same at 10° for both cases.

angles for the proposed frequency diverse antenna. The received signal spectra are well-distinct from each other, and therefore, the DoA can be estimated with a single antenna.

6.2.2 ML-based analysis

Given that the antenna design exhibits distinct radiation patterns across the desired frequency range, the principle of reciprocity suggests that when the antenna operates as a receiver, the received spectral distributions will be distinct for different angles of arrival. However, manually estimating the angle of arrival from the spectrum can be challenging, as the spectral distribution might vary due to multiple factors such as multi-path interference, low signal-to-noise ratio (SNR), and measurement accuracy.

Therefore, ML-based analysis is a suitable solution to overcome these uncertainties, and an accurate DoA estimation can be achieved through proper dataset training.

Based on the radiation patterns over the defined IEEE 802.15.3d communications band spectrum, we can formulate the problem of predicting DoA as the non-linear mapping of the frequency spectrum to the corresponding angle of arrival. In such a situation, a convolutional neural network (CNNs) works best in extracting spatial and complex features as presented by (Ge *et al.*, 2021; Alteneiji *et al.*, 2021). Alteneiji *et al.* similarly used a CNN-based angle of arrival estimation in an indoor radio environment, examining multipath signals from a uniform array of linear antennas (Alteneiji *et al.*, 2021). The radiation patterns examined in our work are directionally dependant in a similar manner, making the spatial correlation highly relevant and vital to accurate prediction of the angle of arrival. As such, we employ a CNN model which extracts the spatial non-linear features from the received spectra of the antenna, followed by a fully connected network for the non-linear mapping of the extracted features to the angle of arrival.

Here, the antenna is considered as a receiver with a transfer function of $|S_{21}(f,\theta,\phi)|$. For a given received signal y_r, the frequency-dependent output of the antenna can be formulated as:

$$x(f) = |S_{21}(f,\theta,\phi)|y_r(f) + n(f)\ , \tag{6.2}$$

where $|S_{21}(f,\theta,\phi)|$ is the amplitude of the angle- and frequency-dependent transfer function that corresponds to the radiation pattern of the designed antenna, and $n(f)$ represents uncorrelated noise. Considering that the radiation parameter of the designed antenna is angle-dependent, we utilize the transfer function and formulate the DoA prediction problem as:

$$[\hat{\theta},\hat{\phi}] = \mathcal{F}(\theta,\phi,|S_{21}(f)|)\ , \tag{6.3}$$

where $\hat{\theta}$ and $\hat{\phi}$ are the predicted angles of arrival, and $\mathcal{F}(.)$ is the learnt non-linear mapping function between the frequency and angle-dependent transfer function and the angles of arrival θ and ϕ.

We build a model to learn this non-linear mapping function, which maps the input θ and ϕ to the output $\hat{\theta}$ and $\hat{\phi}$. The model is trained using the mean squared error loss function:

$$[\hat{\theta},\hat{\phi}] = \arg\min \frac{1}{N}\Sigma_i^N(|\hat{\theta}_i - \theta_i| + |\hat{\phi}_i - \phi_i|)\ , \tag{6.4}$$

where N is the total number of data samples used in training, $\hat{\theta}$ and $\hat{\phi}$ are the model's angle predictions while θ and ϕ are the angles of arrival. The model is thus trained with the objective of minimizing Eq. 6.4. Next, we detail the architecture of the model.

The proposed CNN model is designed to extract spatial non-linear features from the input data, which in this case is the frequency-dependent transfer function of the antenna, $|S_{21}(f,\theta,\phi)|$. The model aims to learn patterns and the non-linear relationships within the data and the desired angles of arrival. Figure 6.5 shows a detailed parameter analysis conducted in order to find the optimal architectural parameters of the proposed model. The numbers of convolutional and fully connected layers are tested as well as the numbers of convolutional filters and fully connected nodes. Figures 6.5(a–d) show that with an increased number of layers the minimum achievable root mean squared error (RMSE) and mean squared error (MSE) increase, indicating a degradation of model performance. This can be attributed to an over-fitting problem. Additionally, Figs. 6.5(e–f) show that as convolutional filters are added, the model performance is enhanced up to a certain point. This eventual degradation is also attributed to model over-fitting as the model grows more complex with additional filters. Similarly, Figs. 6.5(g-h) show that as fully connected nodes are added, the model performance is enhanced.

Following the conducted parameter analysis, Fig. 6.6 represents the complete architecture of the model. The model consists of 3 convolutional layers each containing 128 convolutional filters of size 3×3 followed by a flattening layer to help the convolutional output converge to the following fully connected layer. The model is then followed by three fully connected dense layers, each containing 256 nodes. The convolutional layers in the model extract complex hierarchical features from the input and pass them through the fully connected layers which map the non-linear relationship of the extracted features to the corresponding angles of arrival. The number of convolutional filters and dense nodes are chosen through optimization experiments, testing with 64, 128, 256 convolutional filters and dense nodes. The model performance is found to be optimal with 128 filters and 256 nodes indicating a lower complexity of the hierarchical features extracted from the radiation pattern input, and a higher complexity of the non-linear mapping between the extracted features and the desired angles of arrival output.

The output of each intermediate layer and the final prediction layer of the model can be respectively defined as:

$$\mathbf{Y}_l = \mathbf{A}(\mathbf{W}_l \mathbf{Y}_{l-1} + \mathbf{B}_l) \tag{6.5}$$

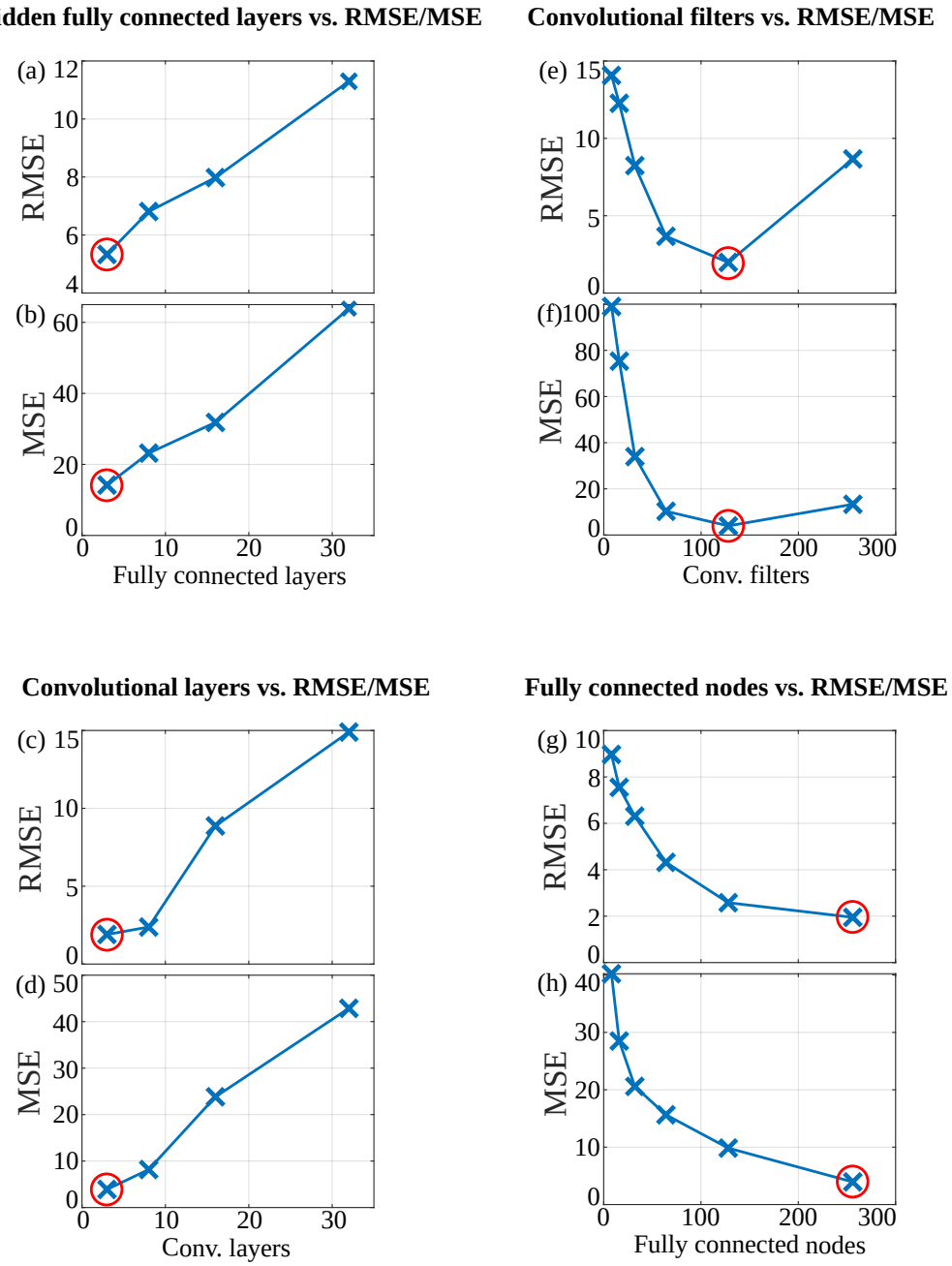

Figure 6.5. Parameter analysis showing model performance with varying model parameters. Model is tested with 3, 8, 16, and 34 fully connected/convolutional layers as well as 8, 16, 32, 64, 128, and 256 convolutional filters and fully connected nodes. (a, b) Minimum achievable RMSE and MSE with varying fully connected layers; the minimum achieved is with 3 layers. (c, d) Minimum achievable RMSE and MSE with varying convolutional layers; the minimum achieved is with 3 layers. (e, f) Minimum achievable RMSE and MSE with varying convolutional filters; the minimum achieved is with 128 filters. (g, h) Minimum achievable RMSE and MSE with varying fully connected nodes; the minimum achieved is with 256 nodes.

$$[\hat{\theta}, \hat{\phi}] = \mathbf{A}(\mathbf{W}|S_{21}(f, \theta, \phi)| + \mathbf{B}) \,, \tag{6.6}$$

where $\mathbf{Y}_l$ is the output to the l^{th} layer in the model, $\mathbf{A}$ is the rectified linear unit (Maas *et al.*, 2013) activation function, and $\mathbf{W}_l$ and $\mathbf{B}_l$ are the learnable weights and biases of the l^{th} layer respectively. When combining the output of each layer represented in Eq. 6.5, we obtain the complete model output with respect to the transfer function of the antenna, shown in Eq. 6.6. $\mathbf{W}$ and $\mathbf{B}$ are the overall learnt weights and bias matrices of the model respectively.

6.3 Antenna fabrication and measurement setup

The fabricated frequency-diverse antenna is shown in Fig. 6.7. Integration of the oversized metallic cavity with the WR-3 hollow waveguide is through secure screws, as depicted in Fig. 6.7(a). Seven aluminum shims, each of around 5×5 mm^2 and a thickness of 0.13 mm, are adhered on the 3-D printed pillars with arbitrary orientations. The metallic scatterers and the COC lens with arbitrary pillar heights are shown in Fig. 6.7(b). The bottom cavity, middle metallic scatterers, and top lens are stacked and aligned using screws. The final device under test (DUT) is illustrated in Figs. 6.7(c) and (d).

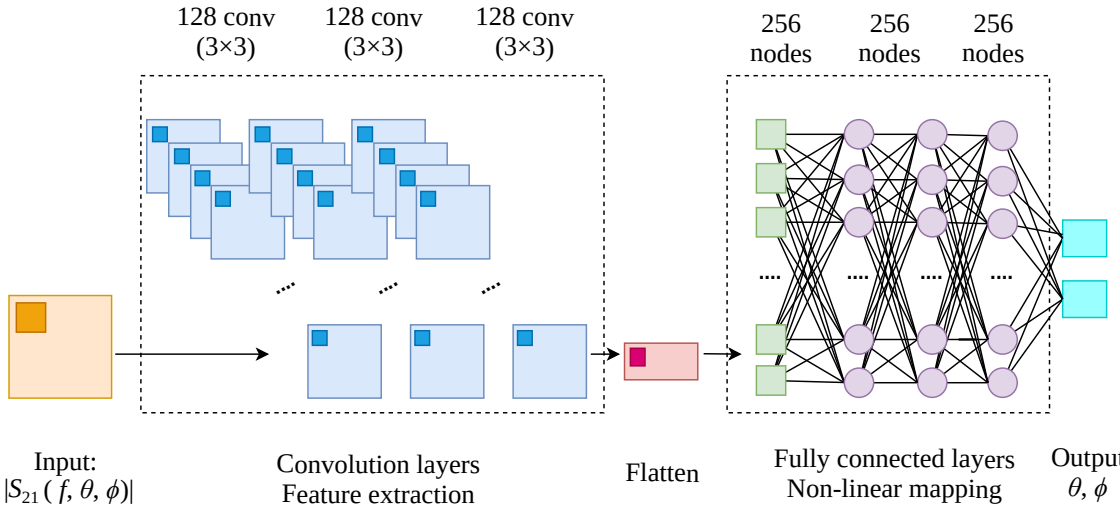

Figure 6.6. Model architecture for the proposed CNN model. Model input is the transfer function associated with θ and ϕ angles of arrival. The model consists of 3 convolutional layers with 128 convolutional filters of size (3×3) each. The model is followed by a flattening convolutional layer and three fully connected layers, each with 256 nodes. The final model output is the predicted angles $\hat{\theta}$ and $\hat{\phi}$.

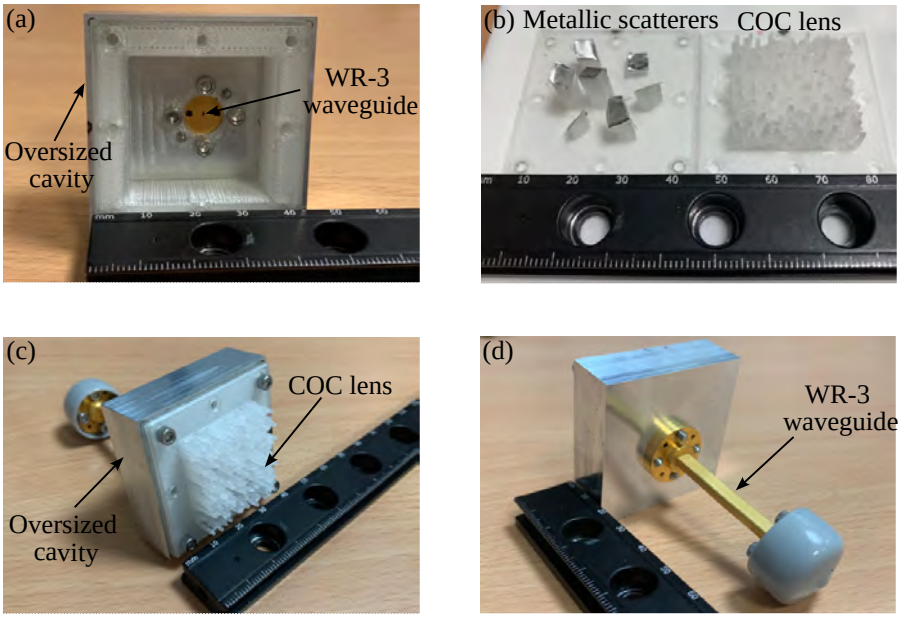

Figure 6.7. Fabricated antenna. (a) Oversized open metallic cavity with WR-3 waveguide feed. (b) Metallic scatterers and 3-D printed COC lens. (c, d) Front and back views of the final device under test (DUT).

The DoA measurement setup is shown in Fig. 6.8(a). A vector network analyzer Keysight N5222B with VDI extension modules operating from 220–330 GHz is used to conduct the experiment. A VDI WR-3.4 diagonal horn antenna functions as the transmitter, and the frequency-diverse antenna operates as the receiving antenna placed at the pivot point of a rotator. Various distances d between the transmitter horn antenna and the receiving DUT are explored, ensuring that the DoA estimation accommodates different received signal power levels. The chosen distances for exploration are 220 mm, 280 mm, 295 mm, 335 mm, and 390 mm. These distances satisfy the far-field condition, approximately occurring beyond a distance of 120 mm. The maximum distance is limited by the cable length. Given the limitations in the laboratory setting, 3-D DoA estimation is unavailable, and hence the measurement focuses on the radiation patterns in the E- and H-planes. The rotating stage is set to an angular resolution of 0.5° for a rotation range of $\pm 35°$ to measure the H-plane pattern. Additionally, two waveguide twists are introduced on both the transmitter and receiver ends for E-plane pattern measurements. For a more comprehensive evaluation of the estimation robustness, two additional scenarios are considered. As shown in Fig. 6.8(b), one scenario incorporates absorbers to mitigate multi-reflections along the path, potentially resulting in lowered

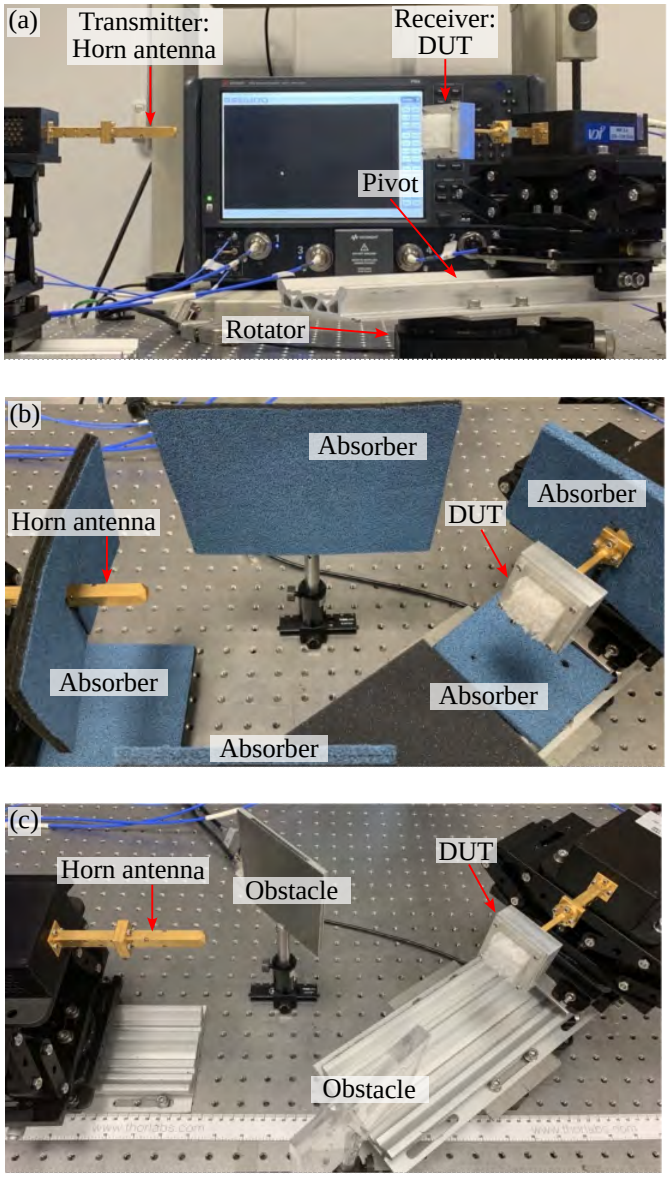

Figure 6.8. Measurement setup. The DUT is placed on the rotator with an angular resolution of 0.5°. The emitted radiation from the horn antenna propagates through free-space over a distance and is captured by the DUT. (a) Normal case. (b) With absorbers. (c) With obstacles.

interference. The other scenario omits the absorbers, while introducing two obstacles near the line of sight, as shown in Fig. 6.8(c). These obstacles introduce a higher level of multipath interference. While the output power from the transmitter can be a good case to investigate, the measurement setup might involve costly waveguide-based attenuators. Overall, these setups at various distances produces a wide and diverse dataset to allow the CNN model to effectively learn and generalize the DoA estimation process across different real-world scenarios.

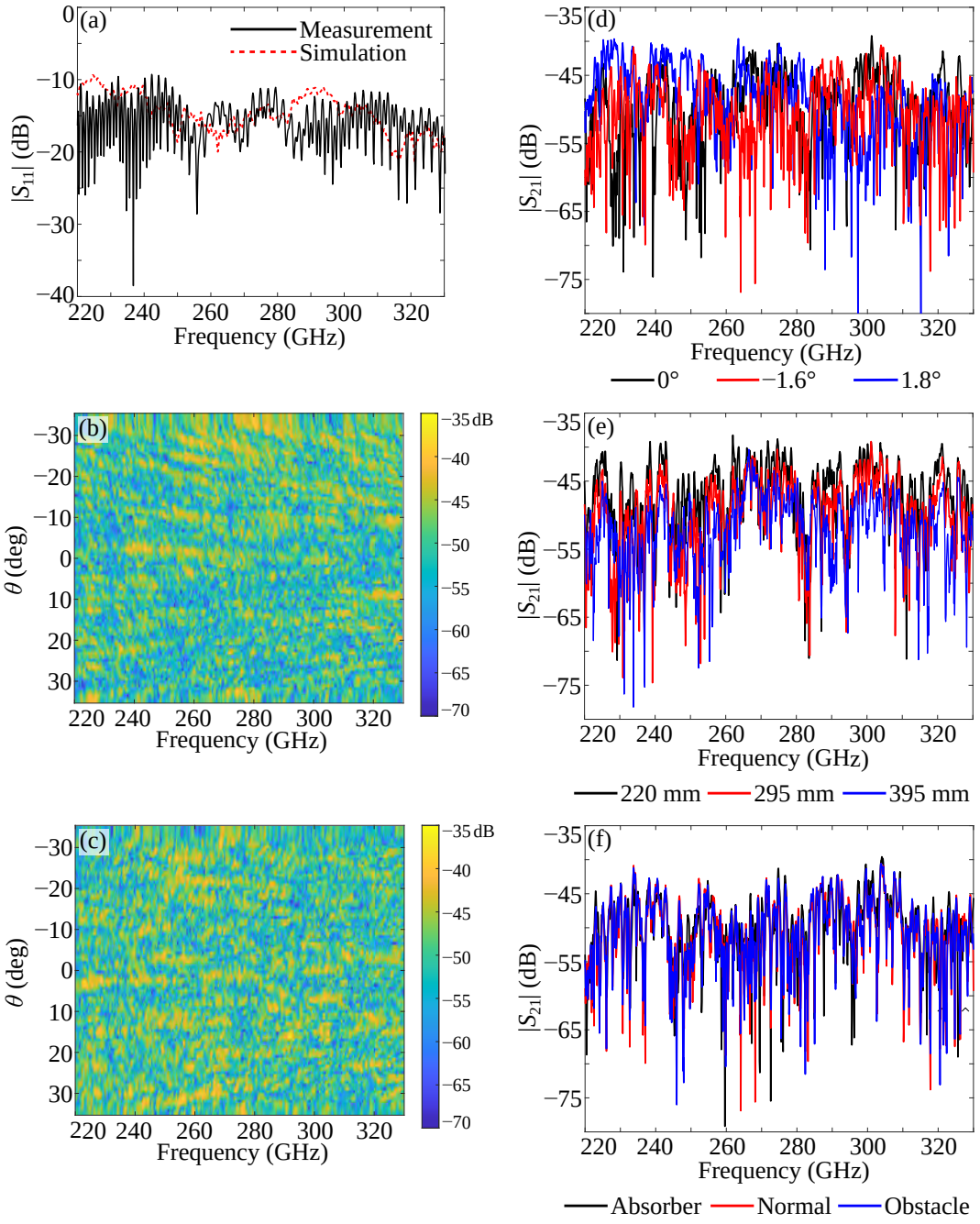

Figure 6.9. Measurement results. (a) Simulated and measured reflection coefficients when the frequency-diverse antenna is a transmitter. (b, c) Received signal against the frequency and the angular displacement on the E- and H-planes, under normal condition and transceiver separation of 295 mm. (d) Received signal on the H-plane at different angles, under normal condition and transceiver separation of 295 mm. (e) Received signal on the H-plane at different separation distances, under normal condition and at the same rotation angle. (f) Received signal on the H-plane under different conditions, at the same transceiver separation of 295 mm and same rotation angle. Note that the analysis is limited to the IEEE terahertz communications band from 252 to 325 GHz.

As shown in Fig. 6.9(a), when the antenna is utilized as a transmitter, the reflection coefficient remains consistently below -10 dB over the entire band. This suggests satisfactory matching for maximum power transfer. The measured reflection coefficient is slightly shifted from the simulation, potentially because the screws and alignment pins with the waveguide flange are not considered in simulation, and the cavity backing has a thickness of around 1 mm that introduces additional propagation path. The obtained radiation pattern results for the nominal case at a distance of 295 mm are represented in Figs. 6.9(b, c). These patterns clearly illustrate the unpredictable spectral distributions in both the *E*- and *H*-planes. Further investigation on the *H*-plane pattern, as shown in Fig. 6.9(d), highlights the irregular transmission level fluctuations for three nearby angles. More specifically, the correlation coefficient between angles with a 1° difference is typically around 0.4, while it drops below 0.15 for angles differing by more than 2°. When the angular displacement is held constant, i.e., at broadside, the received signal level reduces as the distance increases, as anticipated and validated through Fig. 6.9(e). Furthermore, Fig. 6.9(f) shows the transmission levels for three scenarios when the distance and angular displacement are unchanged. A slight enhancement is observed in the case with absorbers, whereas a minor change is evident in the obstacle scenario. In total, a comprehensive dataset comprising 30 sets of measurements has been recorded. This dataset includes a combination of 5 different distances, 3 distinct scenarios, and measurements conducted in both *E*- and *H*-planes. The collected data has been subsequently analyzed by the CNN model for further DoA estimation. In the CNN analysis, only the amplitude spectra within the communications band from 252 to 325 GHz are used.

6.4 DoA prediction with ML

The measurement of the frequency-diverse antenna demonstrates that the received signal spectra at different angles of arrival are distinguishable. Consequently, through ML-based training and analysis, it becomes feasible to estimate the DoA based on the received signal spectra. In this section, part of the collected measurement dataset is utilized for training, and DoA is then estimated by the developed model and compared with the ground truth for validation.

Given the high variation in the data collection conditions in terms of various multipath interferences, *k*-fold cross validation is used to train the data for improved model

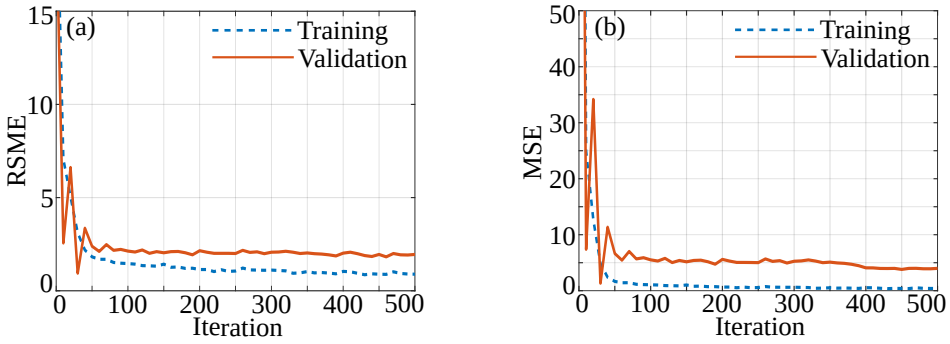

Figure 6.10. Training results for the final k-fold validation. (a) RSME converging to a minimum of 0.89° for training and 1.90° for validation. (b) MSE converging to a minimum of 0.41° for training and 3.90° for validation.

generalization. The training data is split into k folds and training is repeated for k iterations, where each iteration takes $k-1$ folds for training and the remaining fold is used for validation. In this manner, the model is able to learn the complex features introduced by different multipath interference presenting in the dataset. Overall, 80% of the total dataset is used for training while 20% is used for validation and testing. Training is conducted over 500 epochs with the Adam optimizer, learning rate of 0.1 and $k = 5$.

Figure 6.10 shows the MSE and RSME obtained by the model during its training iterations. The model quickly converges to a minimum validation MSE of 3.9° and RSME of 1.9°. This indicates that the model is able to predict θ and ϕ values that are on average 3.9° away from the ground truth value. These values provide insights into the practical usability of the proposed DoA estimation method, offering an indication of the predictable beamwidth of the source antenna. One notable challenge of the DoA estimation is that, for ultra-high gain antenna sources, the current DoA antenna beamwidth may not be sufficient to support such high resolution. This limitation can potentially be addressed by employing a larger DoA antenna aperture with finer resolution in the pillars, resulting in a smaller MSE.

Figure 6.11 shows the prediction results of the model for the three scenarios: normal case, with absorbers, and with obstacles. The predictions for both E- and H-planes are included, and each sub-plot includes the estimation under the measurement for five different distances. The prediction results closely align with the ground truth values, and these results demonstrate the proposed CNN model's robustness across diverse scenarios. While slightly higher errors can be observed near 0°, this may be attributed to

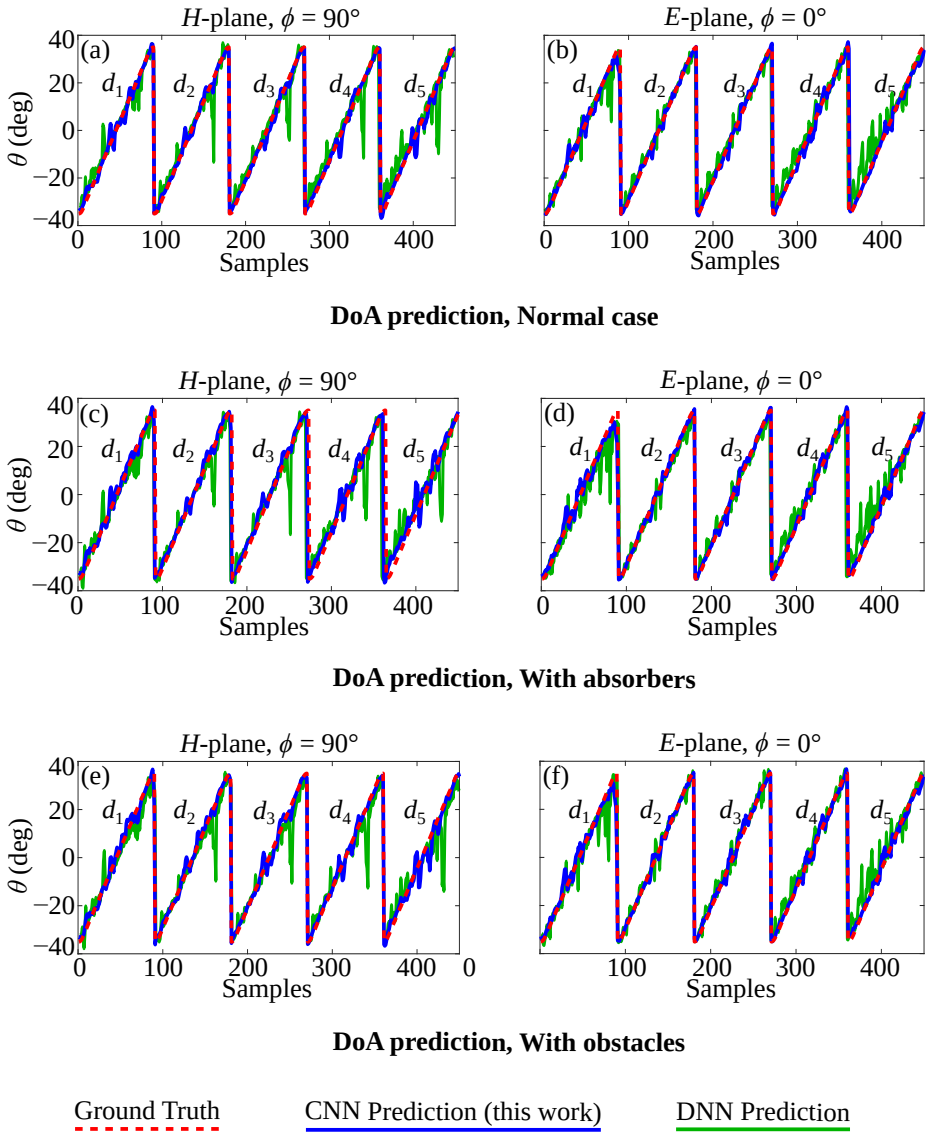

Figure 6.11. DoA predictions of various models. Transceiver distances d_1–d_5 correspond to 220 mm, 280 mm, 295 mm, 335 mm, and 390 mm, respectively. Angular estimation with (a, b) direct line of sight between the transmitter and receiver, (c, d) absorbers placed near the path of the transmitter and receiver, and (e, f) obstacles placed near the path of the transmitter and receiver.

a few discrete pixels exhibiting slightly higher correlation coefficients between adjacent rotation angles near this region. Nevertheless, the consistent performance across these scenarios highlights the adaptability of this model and suggests its potential to enhance DoA estimation in real-world communications setups marked by varying environmental conditions and signal interference. Figure 6.11 also compares the prediction with a baseline deep neural network (DNN) model consisting of three fully connected dense layers. The comparison with the DNN further emphasizes the importance of the spatial feature extraction done through convolutional layers. The minimum validation RMSE

and MSE values obtained for the DNN model are 5.3° and 14.2°, respectively. The degradation in the DNN results highlights the significance of considering the spatial and non-linear features present in the antenna data.

6.5 Conclusion

In this chapter, a frequency-diverse antenna accompanied by CNNs for terahertz DoA estimation is proposed. The antenna is composed of an oversized metallic cavity, seven metallic scatters inside the cavity, and a 3-D printed lens. These components are designed to disrupt symmetry and generate quasi-random radiation patterns across the IEEE 802.15.3d communications band. The CNN model consists of 3 convolutional layers with 3×3 128 filters each. The convolutional layers extract complex hierarchical features from the experimental data, which are then passed on to three fully connected dense layers for non-linear mapping. During experimental validation, three measurement environments have been considered: the normal case, a case with absorbers, and a case with obstacles. Uncorrelated received spectra have been observed across different receiving angles. The DoA estimation of a far-field source demonstrated high accuracy for all three scenarios, regardless of the transceiver separation distances. The proposed frequency-diverse antenna, complemented by ML-assisted analysis, offers considerable advantages as a compact, integrable, and cost-effective solution for practical terahertz DoA estimation in the future.

Looking ahead, several promising directions for future work can be anticipated. Firstly, the validation of the estimation performance in three-dimensional space remains to be done. Secondly, the extension of the proposed approach to scenarios involving multiple transmitters could provide valuable insights into the scalability and adaptability of the model. In cases where two or more signals with similar strengths arrive from different directions simultaneously, estimating the mixed signal becomes challenging and may require analytical approaches to determine the number of incoming signals to alleviate ambiguity. Finally, outdoor validation with portable transmitters and receivers will verify the performance and capability of the model in a real-world environment. As for practical transmission distances, ultra-high gain transceivers are necessary, and therefore the correlation between radiation patterns should be lowered to further improve the estimation accuracy. Potential solutions include increasing the antenna aperture and implementing silicon lenses with randomly etched air holes that can provide stronger reflections to further break the structure symmetry.

Chapter 7

Summary and Outlook

THIS Chapter concludes the doctoral thesis and summarizes its outcomes. Chapter 1 has provided the background knowledge and relevant literature pertaining to this thesis. Chapters 2 to 6 have presented the original contributions in relation to planar antennas and lenses with terahertz source integration. An outlook is presented in this Chapter.

7.1 Thesis conclusion

This doctoral thesis has focused on the development of terahertz planar antennas and lenses with an ultimate aim for source integration. One non-planar frequency-diverse antenna is also included. The proposed designs can be implemented in various applications and aim to be cost-effective, capable of significantly reducing the device profile, and minimizing material losses. This section provides a summary on the original contributions of this thesis.

Antennas integrated with resonant-tunneling diode (RTD) This part includes Chapter 2 and Chapter 3. It presents two planar metallic antennas integrated with RTD with extended bias lines. Planar metallic antennas are employed to manipulate the propagating surface waves along the bias lines, enabling different radiation characteristics. In Chapter 2, a series-fed patch array antenna is introduced to enhance radiation performance. In Chapter 3, a log-spiral antenna is designed for efficient circularly polarized radiation. The antennas are judiciously designed so not to interfere with the oscillation condition of the RTDs.

Metasurface lenses This part includes Chapter 4. It presents a tri-layer metasurface lens designed for efficiently converting a Gaussian beam emitted from a diagonal horn antenna into a flat-top beam within the near-field.

Effective medium lens antenna This part includes Chapter 5. It presents an effective-medium-based high-gain cavity antenna integrated with a waveguide feed. Blind air-holes are laser-etched from both sides of a silicon wafer to create gradient-index lenses for beam collimation.

3-D printed frequency-diverse antenna This part includes Chapter 6. It presents a frequency-diverse antenna with distinct, uncorrelated radiation patterns across the communications band. With a machine learning-assisted analysis, the antenna is applied as a receiver to predict the direction of arrival of terahertz signal.

7.2 Outlook

The planar antennas and lenses proposed in this thesis are beneficial to the development of practical terahertz applications. This Section discusses further research investigations and challenges.

Planar antennas with source integration In the pursuit of higher output power and higher operating frequency for terahertz sources, the current emphasis is primarily on physical aspects such as employing thinner substrates, optimizing substrate choices, and refining fabrication processes. It is important to recognize that as the size of integrated terahertz sources significantly decreases, antennas become an inevitable component for coupling and radiating terahertz energy. A notable gap exists where general antenna design approaches might not be directly suitable to terahertz sources, due to their unconventional feeds and stringent oscillation conditions. It is of great importance to bridge this gap by considering both sources and antennas as integral components of the system. As an example, the proposed antennas for RTDs are currently designed separately from the RTD excitations, aiming to have a negligible effect on the oscillation characteristics of those RTDs in broadband. As a result, parasitic oscillation at lower frequencies can be avoided. Future research endeavors should involve optimizing the coupling between sources and antennas, as well as mitigating the effects of loss components.

Planar lenses with source integration The fundamental principle of planar lenses lies is their ability to control the phase response of local units, enabling the formation of specific phase distributions for various applications. Despite the existence of different phase control techniques, they often share a common trade-off in bandwidth. The sacrificed large bandwidth occurs as the desired phase distribution might not be sustained across a wide frequency range, especially for flat optics involving phase wrapping. This limitation becomes critical in the pursuit of higher data rates for terahertz communications, where the narrow operation bandwidth of the lens could be unacceptable. Future research investigation should involve planar lenses with larger bandwidths, potentially by employing lens combinations.

Another constraint in planar lenses is the inability to support rapid phase variations, as mutual coupling can considerably degrade the performance. When designing planar lenses, caution should be paid to avoid excessively rapid phase wrapping, which can limit design flexibility. Addressing this limitation is a key aspect for practical imaging applications such as 3-D holography in the future.

One notable advantage of planar lenses is their adaptability to extend as a lens array. Investigating and demonstrating the feasibility of such source-integrated lens arrays is crucial as they can support long-distance point-to-multipoint terahertz communications outdoor or terahertz networks with dense cellular environments indoor.

Frequency-diverse antenna for direction-of-arrival estimation To create a compact, planar structure, the non-planar 3-D printed pillars can be substituted by a flat printed block featuring randomly distributed fill factors in its volume. An alternative is developing silicon lenses with randomly etched air holes to further enhance reflections. To expand the proposed direction-of-arrival estimation method to scenarios with multiple sources, a hybrid approach combining analytical calculation and ML-based evaluation may be employed. For example, an analytical method can determine the number of sources initially, then a similar ML-based approach can be utilized to estimate the directions of incoming signals.

Bibliography

ABBASI-M. A. B., FUSCO-V. F., YURDUSEVEN-O., AND FROMENTEZE-T. (2020). Frequency-diverse multimode millimetre-wave constant-ε_r lens-loaded cavity, *Scientific Reports*, **10**(1), art. no. 22145.

ABBASZADEH-A., AHMADI-BOROUJENI-M., AND TEHRANIAN-A. (2019). Generating uniform irradiance in the Fresnel region by quasi-optical beam shaping of a millimeter-wave source, *Optics Express*, **27**(22), pp. 32135–32146.

ABBASZADEH-A., AHMADI-BOROUJENI-M., AND TEHRANIAN-A. (2020). A compact polarization insensitive all-dielectric metasurface lens for Gaussian to tophat beam shaping in sub-terahertz regime, *Optics Communications*, **462**, art. no. 125313.

ABDO-I., DA GOMEZ-C., WANG-C., HATANO-K., LI-Q., LIU-C., YANAGISAWA-K., FADILA-A. A., FUJIMURA-T., MIURA-T., TOKGOZ-K. K., PANG-J., HAMADA-H., NOSAKA-H., SHIRANE-A., AND OKADA-K. (2022). A bi-directional 300-GHz-band phased-array transceiver in 65-nm CMOS with outphasing transmitting mode and LO emission cancellation, *IEEE Journal of Solid-State Circuits*, **57**(8), pp. 2292–2308.

ABDO-I., JYO-T., PANDER-A., WAKITA-H., SHIRATORI-Y., MUTO-M., HAMADA-H., NAGATANI-M., GOMEZ-C. D., WANG-C., HATANO-K., LIU-C., FADILA-A. A., PANG-J., SHIRANE-A., OKADA-K., AND TAKAHASHI-H. (2023). 300-GHz-band four-element CMOS-InP hybrid phased-array transmitter with 36° steering range, *IEEE Microwave and Wireless Technology Letters*, **33**(6), pp. 887–890.

ABIELMONA-S., NGUYEN-H. V., AND CALOZ-C. (2011). Analog direction of arrival estimation using an electronically-scanned CRLH leaky-wave antenna, *IEEE Transactions on Antennas and Propagation*, **59**(4), pp. 1408–1412.

ACHARYYA-A., AND BANERJEE-J. (2014). Prospects of IMPATT devices based on wide bandgap semiconductors as potential terahertz sources, *Applied Nanoscience*, **4**(1), pp. 1–14.

AFSAH-HEJRI-L., HAJEB-P., ARA-P., AND EHSANI-R. J. (2019). A comprehensive review on food applications of terahertz spectroscopy and imaging, *Comprehensive Reviews in Food Science and Food Safety*, **18**(5), pp. 1563–1621.

AFZAL-M. U., ESSELLE-K. P., AND ZEB-B. A. (2015). Dielectric phase-correcting structures for electromagnetic band gap resonator antennas, *IEEE Transactions on Antennas and Propagation*, **63**(8), pp. 3390–3399.

AGATONOVIC-M., STANKOVIC-Z., MILOVANOVIC-I., DONCOV-N., SIT-L., ZWICK-T., AND MILOVANOVIC-B. (2013). Efficient neural network approach for 2D DoA estimation based on antenna array measurements, *Progress In Electromagnetics Research*, **137**(1), pp. 741–758.

AGHASI-H., CATHELIN-A., AND AFSHARI-E. (2017). A 0.92-THz SiGe power radiator based on a nonlinear theory for harmonic generation, *IEEE Journal of Solid-State Circuits*, **52**(2), pp. 406–422.

AKO-R. T., LEE-W. S. L., ATAKARAMIANS-S., BHASKARAN-M., SRIRAM-S., AND WITHAYACHUMNANKUL-W. (2020). Ultra-wideband tri-layer transmissive linear polarization converter for terahertz waves, *APL Photonics*, **5**(4), art. no. 046101.

AKYILDIZ-I. F., HAN-C., HU-Z., NIE-S., AND JORNET-J. M. (2022). Terahertz band communication: An old problem revisited and research directions for the next decade, *IEEE Transactions on Communications*, **70**(6), pp. 4250–4285.

ALONSO-DELPINO-M., BOSMA-S., JUNG-KUBIAK-C., CHATTOPADHYAY-G., AND LLOMBART-N. (2021). Wideband multimode leaky-wave feed for scanning lens-phased array at submillimeter wavelengths, *IEEE Transactions on Terahertz Science and Technology*, **11**(2), pp. 205–217.

ALONSO-DELPINO-M., JUNG-KUBIAK-C., RECK-T., LLOMBART-N., AND CHATTOPADHYAY-G. (2019). Beam scanning of silicon lens antennas using integrated piezomotors at submillimeter wavelengths, *IEEE Transactions on Terahertz Science and Technology*, **9**(1), pp. 47–54.

ALTENEIJI-A., AHMAD-U., POON-K., ALI-N., AND ALMOOSA-N. (2021). Angle of arrival estimation in indoor environment using machine learning, *2021 IEEE Canadian Conference on Electrical and Computer Engineering (CCECE)*, pp. 1–6.

ARABHAVI-A. M., CIABATTINI-F., HAMZELOUI-S., FLÜCKIGER-R., SARANOVAC-T., HAN-D., MARTI-D., BONOMO-G., CHAUDHARY-R., OSTINELLI-O., AND BOLOGNESI-C. R. (2022). InP/GaAsSb double heterojunction bipolar transistor emitter-fin technology with f_{MAX} = 1.2 THz, *IEEE Transactions on Electron Devices*, **69**(4), pp. 2122–2129.

ARZI-K., CLOCHIATTI-S., MUTLU-E., KOWALJOW-A., SIEVERT-B., ERNI-D., WEIMANN-N., AND PROST-W. (2019). Broadband detection capability of a triple barrier resonant tunneling diode, *2019 Second International Workshop on Mobile Terahertz Systems (IWMTS)*, pp. 1–4.

ARZI-K., RENNINGS-A., ERNI-D., WEIMANN-N., PROST-W., SUZUKI-S., AND ASADA-M. (2018). Millimeter-wave signal generation and detection via the same triple barrier RTD and on-chip antenna, *2018 First International Workshop on Mobile Terahertz Systems (IWMTS)*, pp. 1–4.

ASADA-M., AND SUZUKI-S. (2015). Resonant tunneling diodes for terahertz sources, *Handbook of Terahertz Technologies: Devices and Applications*, Singapore: Pan Stanford, pp. 151–178.

ASADA-M., AND SUZUKI-S. (2016). Room-temperature oscillation of resonant tunneling diodes close to 2 THz and their functions for various applications, *Journal of Infrared, Millimeter, and Terahertz Waves*, **37**(12), pp. 1185–1198.

ASADA-M., AND SUZUKI-S. (2021). Terahertz emitter using resonant-tunneling diode and applications, *Sensors*, **21**(4), art. no. 1384.

AYYAGARI-S. R., INDRIŠIŪNAS-S., AND KAŠALYNAS-I. (2023). Hybrid multiphase Fresnel lenses on silicon wafers for terahertz frequencies, *IEEE Transactions on Terahertz Science and Technology*, **13**(3), pp. 231–236.

BABA-A. A., HASHMI-R. M., ESSELLE-K. P., MARIN-J. G., AND HESSELBARTH-J. (2019). Broadband partially reflecting superstrate-based antenna for 60 GHz applications, *IEEE Transactions on Antennas and Propagation*, **67**(7), pp. 4854–4859.

BALAKRISHNAN-J., FISCHER-B. M., AND ABBOTT-D. (2009). Sensing the hygroscopicity of polymer and copolymer materials using terahertz time-domain spectroscopy, *Applied Optics*, **48**(12), pp. 2262–2266.

BASELMANS-J., FACCHIN-F., PASCUAL LAGUNA-A., BUENO-J., THOEN-D. J., MURUGESAN-V., LLOMBART-N., AND DE VISSER-P. (2022). Ultra-sensitive THz microwave kinetic inductance detectors for future space telescopes, *Astronomy & Astrophysics*, **665**, art. no. A17.

BOSMA-S., NETO-A., AND LLOMBART-N. (2022a). On the near-field spherical wave formation in resonant leaky-wave antennas: Application to small lens design, *IEEE Transactions on Antennas and Propagation*, **70**(2), pp. 801–812.

BOSMA-S., VAN ROOIJEN-N., ALONSO-DELPINO-M., SPIRITO-M., AND LLOMBART-N. (2022b). First demonstration of dynamic high-gain beam steering with a scanning lens phased array, *IEEE Journal of Microwaves*, **2**(3), pp. 419–428.

BOWERS-S. M., ABIRI-B., AFLATOUNI-F., AND HAJIMIRI-A. (2014). A compact optically driven travelling-wave radiating source, *2014 Optical Fiber Communication (OFC) Conference*, pp. 1–3.

BOŽANIĆ-M., AND SINHA-S. (2019). Emerging transistor technologies capable of terahertz amplification: A way to re-engineer terahertz radar sensors, *Sensors*, **19**(11), art. no. 2454.

BREWITT TAYLOR-C., GUNTON-D., AND REES-H. (1981). Planar antennas on dielectric surface, *Electronics Letters*, **17**(20), pp. 729–731.

BRINCKER-M., KARLSEN-P., SKOVSEN-E., AND SØNDERGAARD-T. (2016). Microstructured gradient-index lenses for THz photoconductive antennas, *AIP Advances*, **6**(2), art. no. 025015.

BRYNGDAHL-O. (1974). Geometrical transformations in optics, *Journal of the Optical Society of America*, **64**(8), pp. 1092–1099.

BUENO-J., BOSMA-S., BUSSKAMP-ALDA-T., ALONSO-DELPINO-M., AND LLOMBART-N. (2022). Lossless matching layer for silicon lens arrays at 500 GHz using laser ablated structures, *IEEE Transactions on Terahertz Science and Technology*, **12**(6), pp. 667–672.

BURFORD-N. M., AND EL-SHENAWEE-M. O. (2017). Review of terahertz photoconductive antenna technology, *Optical Engineering*, **56**(1), art. no. 010901.

CAMPO-M. A., BLANCO-D., BRUNI-S., NETO-A., AND LLOMBART-N. (2020). On the use of fly's eye lenses with leaky-wave feeds for wideband communications, *IEEE Transactions on Antennas and Propagation*, **68**(4), pp. 2480–2493.

CAMPO-M. A., CARLUCCIO-G., BLANCO-D., LITSCHKE-O., BRUNI-S., AND LLOMBART-N. (2021a). Wideband circularly polarized antenna with in-lens polarizer

for high-speed communications, *IEEE Transactions on Antennas and Propagation*, **69**(1), pp. 43–54.

CAMPO-M. A., CARLUCCIO-G., BRUNI-S., AND LLOMBART-N. (2021b). Dielectric gratings enhancing the field of view in low dielectric permittivity elliptical lenses, *IEEE Transactions on Antennas and Propagation*, **69**(11), pp. 7308–7322.

CHANG-C.-C., HEADLAND-D., ABBOTT-D., WITHAYACHUMNANKUL-W., AND CHEN-H.-T. (2017). Demonstration of a highly efficient terahertz flat lens employing tri-layer metasurfaces, *Optics Letters*, **42**(9), pp. 1867–1870.

CHEBEN-P., HALIR-R., SCHMID-J. H., ATWATER-H. A., AND SMITH-D. R. (2018). Subwavelength integrated photonics, *Nature*, **560**, pp. 565–572.

CHUNG-B., LEES-H., HEADLAND-D., AND WITHAYACHUMNAKUL-W. (2022). Broadband and efficient terahertz beam scanning using a 3D-printed Risley prism, *2022 47th International Conference on Infrared, Millimeter and Terahertz Waves (IRMMW-THz)*, pp. 1–2.

CIMBRI-D., MORARIU-R., OFIARE-A., AND WASIGE-E. (2022a). $In_{0.53}Ga_{0.47}As/AlAs$ double-barrier resonant tunnelling diodes with high-power performance in the low-terahertz band, *2022 Fifth International Workshop on Mobile Terahertz Systems (IWMTS)*, pp. 1–5.

CIMBRI-D., WANG-J., AL-KHALIDI-A., AND WASIGE-E. (2022b). Resonant tunneling diodes high-speed terahertz wireless communications - a review, *IEEE Transactions on Terahertz Science and Technology*, **12**(3), pp. 226–244.

CLOCHIATTI-S., MUTLU-E., PREUSS-C., KRESS-R., PROST-W., AND WEIMANN-N. (2021). Broadband THz detection using InP triple-barrier resonant tunneling diode with integrated antenna, *2021 Fourth International Workshop on Mobile Terahertz Systems (IWMTS)*, pp. 1–5.

CONG-L., CAO-W., ZHANG-X., TIAN-Z., GU-J., SINGH-R., HAN-J., AND ZHANG-W. (2013). A perfect metamaterial polarization rotator, *Applied Physics Letters*, **103**(17), art. no. 171107.

CONG-L., XU-N., GU-J., SINGH-R., HAN-J., AND ZHANG-W. (2014). Highly flexible broadband terahertz metamaterial quarter-wave plate, *Laser & Photonics Reviews*, **8**(4), pp. 626–632.

DAI-J., ZHANG-J., ZHANG-W., AND GRISCHKOWSKY-D. (2004). Terahertz time-domain spectroscopy characterization of the far-infrared absorption and index of refraction of high-resistivity, float-zone silicon, *Journal of the Optical Society of America B*, **21**(7), pp. 1379–1386.

DAN-I., DUCOURNAU-G., HISATAKE-S., SZRIFTGISER-P., BRAUN-R.-P., AND KALLFASS-I. (2020). A terahertz wireless communication link using a superheterodyne approach, *IEEE Transactions on Terahertz Science and Technology*, **10**(1), pp. 32–43.

DECHWECHPRASIT-P., LEES-H., HEADLAND-D., FUMEAUX-C., AND WITHAYACHUMNANKUL-W. (2023). 1-to-*N* terahertz integrated switches enabling multi-beam antennas, *Optica*, **10**(11), pp. 1551–1558.

DIEBOLD-S., NAKAI-S., NISHIO-K., KIM-J., TSURUDA-K., MUKAI-T., FUJITA-M., AND NAGATSUMA-T. (2016). Modeling and simulation of terahertz resonant tunneling diode-based circuits, *IEEE Transactions on Terahertz Science and Technology*, **6**(5), pp. 716–723.

DOBROIU-A., ASAMA-K., SUZUKI-S., ASADA-M., AND ITO-H. (2022). Terahertz-wave three-dimensional imaging using a resonant-tunneling-diode oscillator, *Journal of Infrared, Millimeter, and Terahertz Waves*, **43**(5–6), pp. 464–478.

DOBROIU-A., SHIRAKAWA-Y., SUZUKI-S., ASADA-M., AND ITO-H. (2020). Subcarrier frequency-modulated continuous-wave radar in the terahertz range based on a resonant-tunneling-diode oscillator, *Sensors*, **20**(23), art. no. 6848.

DURGUN-A. C., BALANIS-C. A., BIRTCHER-C. R., AND ALLEE-D. R. (2011). Design, simulation, fabrication and testing of flexible bow-tie antennas, *IEEE Transactions on Antennas and Propagation*, **59**(12), pp. 4425–4435.

ERICSSON. (2022). *6G – Connecting a Cyber-Physical World*, Ericsson.

FERNANDEZ-DOMINGUEZ-A. I., MARTIN-MORENO-L., GARCIA-VIDAL-F. J., ANDREWS-S. R., AND MAIER-S. A. (2008). Spoof surface plasmon polariton modes propagating along periodically corrugated wires, *IEEE Journal of Selected Topics in Quantum Electronics*, **14**(6), pp. 1515–1521.

FILIPOVIC-D., GEARHART-S., AND REBEIZ-G. (1993). Double-slot antennas on extended hemispherical and elliptical silicon dielectric lenses, *IEEE Transactions on Microwave Theory and Techniques*, **41**(10), pp. 1738–1749.

FRIIS-H. (1946). A note on a simple transmission formula, *Proceedings of the IRE*, **34**(5), pp. 254–256.

FROMENTEZE-T., YURDUSEVEN-O., IMANI-M. F., GOLLUB-J., DECROZE-C., CARSENAT-D., AND SMITH-D. R. (2015). Computational imaging using a mode-mixing cavity at microwave frequencies, *Applied Physics Letters*, **106**(19), art. no. 194104.

FUJIKATA-H., HAN-F., KOBAYASHI-K., TANAKA-H., SUZUKI-S., AND ASADA-M. (2021). Oscillations at 300-400 GHz in structure-simplified resonant-tunneling-diode oscillators with rectangular-cavity resonators, *2021 46th International Conference on Infrared, Millimeter and Terahertz Waves (IRMMW-THz)*, pp. 1–2.

FUJIKATA-H., TANAKA-H., HAN-F., ISHIKAWA-A., SUZUKI-S., AND ASADA-M. (2022). Terahertz oscillator using rectangular-cavity resonator and large-area RTD with heat dissipation structure, *2022 47th International Conference on Infrared, Millimeter and Terahertz Waves (IRMMW-THz)*, pp. 1–2.

FUJITA-K., JUNG-S., JIANG-Y., KIM-J. H., NAKANISHI-A., ITO-A., HITAKA-M., EDAMURA-T., AND BELKIN-M. A. (2018). Recent progress in terahertz difference-frequency quantum cascade laser sources, *Nanophotonics*, **7**(11), pp. 1795–1817.

FUKUNAGA-K., OGAWA-Y., HAYASHI-S., AND HOSAKO-I. (2007). Terahertz spectroscopy for art conservation, *IEICE Electronics Express*, **4**(8), pp. 258–263.

GAO-L., AND CHAN-C. H. (2022a). A 0.45-THz 2-D scalable radiator array with 28.2-dBm EIRP using an elliptical teflon lens, *IEEE Journal of Solid-State Circuits*, **57**(2), pp. 400–412.

GAO-L., AND CHAN-C. H. (2022b). A 0.68–0.72-THz 2-D scalable radiator array with –3-dBm radiated power and 27.3-dBm EIRP in 65-nm CMOS, *IEEE Journal of Solid-State Circuits*, **57**(10), pp. 3114–3124.

GAO-L., AND CHAN-C. H. (2023). A 0.64-to-0.69 THz beam-steerable coherent source with 9.1dBm radiated power and 30.8dBm lensless EIRP in 65nm CMOS, *2023 IEEE International Solid-State Circuits Conference (ISSCC)*, pp. 362–364.

GAO-L., AND CHAN-C. H. (2024a). A 0.6-THz area-efficient source based on parallel coupled oscillators and a bandwidth expanded differentially-fed shared aperture patch antenna, *IEEE Transactions on Microwave Theory and Techniques*, **72**(1), pp. 173–182.

GAO-L., AND CHAN-C. H. (2024b). A 144-element beam-steerable source array with 9.1-dBm radiated power and 30.8-dBm lensless EIPR at 675 GHz, *IEEE Journal of Solid-State Circuits*, **59**(2), pp. 375–387.

GAO-W., LEE-W. S. L., YU-X., FUJITA-M., NAGATSUMA-T., FUMEAUX-C., AND WITHAYACHUMNANKUL-W. (2021). Characteristics of effective-medium-clad dielectric waveguides, *IEEE Transactions on Terahertz Science and Technology*, **11**(1), pp. 28–41.

GAO-W., WITHAYACHUMNANKUL-W., FUJITA-M., AND NAGATSUMA-T. (2023). 3D printed terahertz lens antenna fed by effective-medium-clad dielectric waveguide, *2023 XXXVth General Assembly and Scientific Symposium of the International Union of Radio Science (URSI GASS)*, pp. 1–4.

GARCÍA-RIAL-F., MONTESANO-D., GÓMEZ-I., CALLEJERO-C., BAZUS-F., AND GRAJAL-J. (2019). Combining commercially available active and passive sensors into a millimeter-wave imager for concealed weapon detection, *IEEE Transactions on Microwave Theory and Techniques*, **67**(67), pp. 1167–1183.

GERCHBERG-R. W., AND SAXTON-W. O. (1972). A practical algorithm for the determination of the phase from image and diffraction plane pictures, *Optik*, **35**(2), pp. 237–246.

GE-S., LI-K., AND RUM-S. N. B. M. (2021). Deep learning approach in DoA estimation: A systematic literature review, *Mobile Information Systems*, **2021**(1), pp. 1–14.

GOMEZ-TORRENT-A., GARCÍA-VIGUERAS-M., LE COQ-L., MAHMOUD-A., ETTORRE-M., SAULEAU-R., AND OBERHAMMER-J. (2020a). A low-profile and high-gain frequency beam steering subterahertz antenna enabled by silicon micromachining, *IEEE Transactions on Antennas and Propagation*, **68**(2), pp. 672–682.

GOMEZ-TORRENT-A., TOMURA-T., KURAMOTO-W., HIROKAWA-J., WATANABE-I., KASAMATSU-A., AND OBERHAMMER-J. (2020b). A 38 dB gain, low-loss, flat array antenna for 320–400 GHz enabled by silicon-on-insulator micromachining, *IEEE Transactions on Antennas and Propagation*, **68**(6), pp. 4450–4458.

GONZALEZ-A., KANEKO-K., KOJIMA-T., ASAYAMA-S., AND UZAWA-Y. (2017). Terahertz corrugated horns (1.25–1.57 THz): Design, gaussian modeling, and measurements, *IEEE Transactions on Terahertz Science and Technology*, **7**(1), pp. 42–52.

GOODMAN-J., SALMOND-D., DAVIS-C., AND ACOSTA-C. (2019). Ambiguity resolution in direction of arrival estimation using mixed integer optimization and deep learning, *2019 IEEE National Aerospace and Electronics Conference (NAECON)*, pp. 317–322.

GOUDARZI-A., HONARI-M. M., AND MIRZAVAND-R. (2022). A millimeter-wave Fabry–Perot cavity antenna with unidirectional beam scanning capability for 5G applications, *IEEE Transactions on Antennas and Propagation*, **70**(3), pp. 1787–1796.

GRADY-N. K., HEYES-J. E., CHOWDHURY-D. R., ZENG-Y., REITEN-M. T., AZAD-A. K., TAYLOR-A. J., DALVIT-D. A. R., AND CHEN-H.-T. (2013). Terahertz metamaterials for linear polarization conversion and anomalous refraction, *Science*, **340**(6138), pp. 1304–1307.

GROSSMAN-E. N., SAUVAGEAU-J. E., AND MCDONALD-D. G. (1991). Lithographic spiral antennas at short wavelengths, *Applied Physics Letters*, **59**(25), pp. 3225–3227.

GRZESLO-M., DÜLME-S., CLOCHIATTI-S., NEERFELD-T., HADDAD-T., LU-P., TEBART-J., MAKHLOUF-S., BIURRUN-QUEL-C., ESTÉVEZ-J. L. F., LACKMANN-J., WEIMANN-N., AND STÖHR-A. (2023). High saturation photocurrent THz waveguide-type MUTC-photodiodes reaching mW output power within the WR3.4 band, *Optics Express*, **31**(4), pp. 6484–6498.

GU-C., GAO-S., FUSCO-V., GIBBONS-G., SANZ-IZQUIERDO-B., STANDAERT-A., REYNAERT-P., BÖSCH-W., GADRINGER-M., XU-R., AND YANG-X. (2020). A D-band 3D-printed antenna, *IEEE Transactions on Terahertz Science and Technology*, **10**(5), pp. 433–442.

GUERBOUKHA-H., SHRESTHA-R., NERONHA-J., FANG-Z., AND MITTLEMAN-D. M. (2023). Conformal leaky-wave antennas for wireless terahertz communications, *Communications Engineering*, **2**(1), art. no. 17.

GUO-Q.-Y., LIN-Q. W., AND WONG-H. (2021). A high gain millimeter-wave circularly polarized Fabry–Pérot antenna using PRS-integrated polarizer, *IEEE Transactions on Antennas and Propagation*, **69**(2), pp. 1179–1183.

HAFEZI-E., AND SARABANDI-K. (2023). Design and microfabrication of a 230-GHz planar reflectionless lens based on miniaturized-element frequency-selective surfaces, *IEEE Transactions on Terahertz Science and Technology*, **13**(6), pp. 718–728.

HAN-F., FUJIKATA-H., TANAKA-H., SUZUKI-S., AND ASADA-M. (2022). High-power cavity-type RTD THz oscillators integrated with impedance-matched slot antenna, *2022 47th International Conference on Infrared, Millimeter and Terahertz Waves (IRMMW-THz)*, pp. 1–2.

HAN-F., KOBAYASHI-K., SUZUKI-S., TANAKA-H., FUJIKATA-H., AND ASADA-M. (2021). Impedance matching in high-power resonant-tunneling-diode terahertz oscillators integrated with rectangular-cavity resonator, *IEICE Transactions on Electronics*, **E104.C**(8), pp. 398–402.

HAN-F., SHIMURA-T., TANAKA-H., AND SUZUKI-S. (2023). Two coupled resonant-tunneling-diode oscillators with an air-bridged transmission line for high-power coherent terahertz radiation, *Applied Physics Express*, **16**(6), art. no. 064003.

HAYAT-T., AFZAL-M. U., AHMED-F., ZHANG-S., ESSELLE-K. P., AND VARDAXOGLOU-Y. (2020). Low-cost ultrawideband high-gain compact resonant cavity antenna, *IEEE Antennas and Wireless Propagation Letters*, **19**(7), pp. 1271–1275.

HEADLAND-D., AND WITHAYACHUMNANKUL-W. (2022). Continuous leakage from slow-wave structure for integrated all-dielectric uniform leaky wave antenna, *2022 16th European Conference on Antennas and Propagation (EuCAP)*, pp. 1–5.

HEADLAND-D. J., NISHIDA-Y., YU-X., FUJITA-M., AND NAGATSUMA-T. (2023). Terahertz oscillator chips backside-coupled to unclad microphotonics, *IEEE Journal of Selected Topics in Quantum Electronics*, **29**(3), pp. 1–10.

HEADLAND-D., MONNAI-Y., ABBOTT-D., FUMEAUX-C., AND WITHAYACHUMNANKUL-W. (2018a). Tutorial: Terahertz beamforming, from concepts to realizations, *APL Photonics*, **3**(5), art. no. 051101.

HEADLAND-D., WITHAYACHUMNANKUL-W., YAMADA-R., FUJITA-M., AND NAGATSUMA-T. (2018b). Terahertz multi-beam antenna using photonic crystal waveguide and Luneburg lens, *APL Photonics*, **3**(12), art. no. 126105.

HE-Y., CHEN-Y., ZHANG-L., WONG-S.-W., AND CHEN-Z. N. (2020). An overview of terahertz antennas, *China Communications*, **17**(7), pp. 124–165.

HIRATA-A., KOSUGI-T., TAKAHASHI-H., TAKEUCHI-J., TOGO-H., YAITA-M., KUKUTSU-N., AIHARA-K., MURATA-K., SATO-Y., NAGATSUMA-T., AND KADO-Y. (2012). 120-GHz-band wireless link technologies for outdoor 10-Gbit/s data transmission, *IEEE Transactions on Microwave Theory and Techniques*, **60**(3), pp. 881–895.

HOANG-T., FUSCO-V., AND ABBASI-M. (2021). Single pixel polarimetric direction of arrival estimation using programmable coding metasurface aperture, *Scientific Reports*, **11**(1), art. no. 23830.

HORESTANI-A. K., WITHAYACHUMNANKUL-W., CHAHADIH-A., GHADDAR-A., ZEHAR-M., ABBOTT-D., FUMEAUX-C., AND AKALIN-T. (2013). Metamaterial-inspired bandpass filters for terahertz surface waves on Goubau lines, *IEEE Transactions on Terahertz Science and Technology*, **3**(6), pp. 851–858.

HORIKAWA-D., CHEN-Y., KOIKE-T., SUZUKI-S., AND ASADA-M. (2018). Resonant-tunneling-diode terahertz oscillator integrated with a radial line slot antenna for circularly polarized wave radiation, *Semiconductor Science and Technology*, **33**(11), art. no. 114005.

HRISTOV-H. (2016). Fresnel zone plate antenna, *Handbook of Antenna Technologies*, Singapore: Springer, pp. 1187–1248.

IEEE STD 145-2013. (2014). *IEEE Standard for Definitions of Terms for Antennas*, IEEE.

IEEE STD 802.15.3D-2017. (2014). *IEEE Standard for High Data Rate Wireless Multi-Media Networks–Amendment 2: 100 Gb/s Wireless Switched Point-to-Point Physical Layer*, IEEE.

INO. (2022). *INO MICROXCAM-384i-THz Terahertz Camera*, INO.

ISHIBASHI-T., AND ITO-H. (2022). Uni-traveling carrier photodiodes: Development and prospects, *IEEE Journal of Selected Topics in Quantum Electronics*, **28**(2), pp. 1–6.

ISHIBASHI-T., SHIMIZU-N., KODAMA-S., ITO-H., NAGATSUMA-T., AND FURUTA-T. (1997). Uni-traveling-carrier photodiodes, *Ultrafast Electronics and Optoelectronics*, Optica Publishing Group, art. no. UC3.

IWAMATSU-S., NISHIDA-Y., FUJITA-M., AND NAGATSUMA-T. (2021). Terahertz coherent oscillator integrated with slot-ring antenna using two resonant tunneling diodes, *Applied Physics Express*, **14**(3), art. no. 034001.

IZUMI-R., SUZUKI-S., AND ASADA-M. (2017). 1.98 THz resonant-tunneling-diode oscillator with reduced conduction loss by thick antenna electrode, *2017 42nd International Conference on Infrared, Millimeter, and Terahertz Waves (IRMMW-THz)*, pp. 1–2.

JACKSON-D. R., CALOZ-C., AND ITOH-T. (2012). Leaky-wave antennas, *Proceedings of the IEEE*, **100**(7), pp. 2194–2206.

JALILI-H., AND MOMENI-O. (2019). A 0.34-THz wideband wide-angle 2-D steering phased array in 0.13-μm SiGe BiCMOS, *IEEE Journal of Solid-State Circuits*, **54**(9), pp. 2449–2461.

JEPSEN-P., COOKE-D., AND KOCH-M. (2011). Terahertz spectroscopy and imaging – modern techniques and applications, *Laser & Photonics Reviews*, **5**(1), pp. 124–166.

JIA-W., LOU-M., GAO-W., AND SENSALE-RODRIGUEZ-B. (2022). Design and fabrication of a terahertz dual-plane hologram and extended-depth-of-focus diffractive lens, *Optics Continuum*, **1**(8), pp. 1722–1729.

JIN-Y., RENO-J. L., AND KUMAR-S. (2020). Phase-locked terahertz plasmonic laser array with 2 W output power in a single spectral mode, *Optica*, **7**(6), pp. 708–715.

KASAGI-K., SUZUKI-S., AND ASADA-M. (2019). Large-scale array of resonant-tunneling-diode terahertz oscillators for high output power at 1 THz, *Journal of Applied Physics*, **125**(15), art. no. 151601.

KHALID-A., DUNN-G. M., MACPHERSON-R. F., THOMS-S., MACINTYRE-D., LI-C., STEER-M. J., PAPAGEORGIOU-V., THAYNE-I. G., KUBALL-M., OXLEY-C. H., MONTES BAJO-M., STEPHEN-A., GLOVER-J., AND CUMMING-D. R. S. (2014). Terahertz oscillations in an $In_{0.53}Ga_{0.47}As$ submicron planar Gunn diode, *Journal of Applied Physics*, **115**(11), art. no. 114502.

KHALILY-M., TAFAZOLLI-R., RAHMAN-T. A., AND KAMARUDIN-M. R. (2016). Design of phased arrays of series-fed patch antennas with reduced number of the controllers for 28-GHz mm-wave applications, *IEEE Antennas and Wireless Propagation Letters*, **15**, pp. 1305–1308.

KITAGAWA-S., MIZUNO-M., SAITO-S., OGINO-K., SUZUKI-S., AND ASADA-M. (2017). Frequency-tunable resonant-tunneling-diode terahertz oscillators applied to absorbance measurement, *Japanese Journal of Applied Physics*, **56**(5), art. no. 058002.

KLEINDIENST-R., MOELLER-L., AND SINZINGER-S. (2010). Highly efficient refractive Gaussian-to-tophat beam shaper for compact terahertz imager, *Applied Optics*, **49**(10), pp. 1757–1763.

KOBAYASHI-K., SUZUKI-S., HAN-F., TANAKA-H., FUJIKATA-H., AND ASADA-M. (2020). Analysis of a high-power resonant-tunneling-diode terahertz oscillator integrated with a rectangular cavity resonator, *Japanese Journal of Applied Physics*, **59**(5), art. no. 050907.

KONG-S., SHUM-K. M., YANG-C., GAO-L., AND CHAN-C. H. (2021). Wide impedance-bandwidth and gain-bandwidth terahertz on-chip antenna with chip-integrated dielectric resonator, *IEEE Transactions on Antennas and Propagation*, **69**(8), pp. 4269–4278.

KONNO-H., DOBROIU-A., SUZUKI-S., ASADA-M., AND ITO-H. (2021). Discrete fourier transform radar in the terahertz-wave range based on a resonant-tunneling-diode oscillator, *Sensors*, **21**(13), art. no. 4367.

KONSTANTINIDIS-K., FERESIDIS-A. P., CONSTANTINOU-C. C., HOARE-E., GASHINOVA-M., LANCASTER-M. J., AND GARDNER-P. (2017). Low-THz dielectric lens antenna with integrated waveguide feed, *IEEE Transactions on Terahertz Science and Technology*, **7**(5), pp. 572–581.

KOYAMA-Y., KITAZAWA-Y., YUKIMASA-K., UCHIDA-T., YOSHIOKA-T., FUJIMOTO-K., SATO-T., IBA-J., SAKURAI-K., AND ICHIKAWA-T. (2022). A high-power terahertz source over 10 mW at 0.45 THz using an active antenna array with integrated patch antennas and resonant-tunneling diodes, *IEEE Transactions on Terahertz Science and Technology*, **12**(5), pp. 510–519.

KRESS-R., MUTLU-E., KUBICZEK-T., KOSSMANN-J., PREUSS-C., SCHULTZE-T., BALZER-J. C., PROST-W., AND WEIMANN-N. (2022). Transfer-substrate process for InP RTD-oscillator characterization, *2022 Fifth International Workshop on Mobile Terahertz Systems (IWMTS)*, pp. 1–5.

KROEMER-H. (1964). Theory of the Gunn effect, *Proceedings of the IEEE*, **52**(12), pp. 1736–1736.

KÖHLER-R., TREDICUCCI-A., BELTRAM-F., BEERE-H. E., LINFIELD-E. H., DAVIES-A. G., RITCHIE-D. A., IOTTI-R. C., AND ROSSI-F. (2002). Terahertz semiconductor-heterostructure laser, *Nature*, **417**(6885), pp. 156–159.

LAMMINEN-A., TAMMINEN-A., SAARILAHTI-J., ERMOLOV-V., AND PURSULA-P. (2022). The effect of surface passivation for sub-THz silicon gradient refractive index lens, *2021 51st European Microwave Conference (EuMC)*, pp. 873–876.

LATZEL-P., PAVANELLO-F., BILLET-M., BRETIN-S., BECK-A., VANWOLLEGHEM-M., COINON-C., WALLART-X., PEYTAVIT-E., DUCOURNAU-G., ZAKNOUNE-M., AND LAMPIN-J.-F. (2017). Generation of mW level in the 300-GHz band using resonant-cavity-enhanced unitraveling carrier photodiodes, *IEEE Transactions on Terahertz Science and Technology*, **7**(6), pp. 800–807.

LEES-H., HEADLAND-D., MURAKAMI-S., FUJITA-M., AND WITHAYACHUMNANKUL-W. (2024). Terahertz radar with all-dielectric leaky-wave antenna, *APL Photonics*, **9**(3), art. no. 036107.

LEE-S. H., LEE-Y. K., LEE-S.-H., KWAK-J., SONG-H. S., AND SEO-M. (2022). Detection and discrimination of SARS-CoV-2 spike protein-derived peptides using THz metamaterials, *Biosensors and Bioelectronics*, **202**, art. no. 113981.

LEE-W. S. L., AKO-R. T., LOW-M. X., BHASKARAN-M., SRIRAM-S., FUMEAUX-C., AND WITHAYACHUMNANKUL-W. (2018). Dielectric-resonator metasurfaces for broadband terahertz quarter- and half-wave mirrors, *Optics Express*, **26**(11), pp. 14392–14406.

LEE-W. S. L., FERRANTE-A., WITHAYACHUMNANKUL-W., AND ABLE-J. A. (2020). Assessing frost damage in barley using terahertz imaging, *Optics Express*, **28**(21), pp. 30644–30655.

LEUCHS-S., KREBS-C., GÜTGEMANN-S., WICKMANN-S., PERSKE-J., CETINKAYA-H., POHL-N., FISCHER-B., TOLIN-E., CAMPO-M. A., BRUNI-S., ROMSTADT-J., PAPURCU-H., HASCHKE-T., AND HUGE-T. (2022). Highly integrated real-time imaging MIMO D-band radar for industrial applications, *2022 52nd European Microwave Conference (EuMC)*, pp. 768–771.

LIANG-J., GAO-W., LEES-H., AND WITHAYACHUMNANKUL-W. (2021). All-silicon terahertz planar horn antenna, *IEEE Antennas and Wireless Propagation Letters*, **20**(11), pp. 2181–2185.

LIAO-D., CHAN-K. F., CHAN-C. H., ZHANG-Q., AND WANG-H. (2020). All-optical diffractive neural networked terahertz hologram, *Optics Letters*, **45**(10), pp. 2906–2909.

LI-H., WANG-G., ZHU-L., GAO-X., AND HOU-H. (2020). Wideband beam-forming metasurface with simultaneous phase and amplitude modulation, *Optics Communications*, **466**, art. no. 124601.

LI-M. S., ABDULLAH-M., HE-J., WANG-K., FUMEAUX-C., AND WITHAYACHUMNANKUL-W. (2024a). Frequency-diverse antenna with convolutional neural networks for direction of arrival estimation in terahertz communications, *IEEE Transactions on Terahertz Science and Technology*. Early access, doi: 10.1109/TTHZ.2024.3358735.

LI-M. S., AKO-R. T., SRIRAM-S., FUMEAUX-C., AND WITHAYACHUMNANKUL-W. (2023a). High-gain, low-profile, integrable planar lens antenna at 275 GHz, *2023 IEEE 11th Asia-Pacific Conference on Antennas and Propagation (APCAP)*. (**Invited**).

LI-M. S., AKO-R. T., SRIRAM-S., FUMEAUX-C., AND WITHAYACHUMNANKUL-W. (2023b). Terahertz metasurface for near-field beam conversion, *Optics Letters*, **48**(8), pp. 2202–2205.

LI-M. S., AKO-R. T., SRIRAM-S., FUMEAUX-C., AND WITHAYACHUMNANKUL-W. (2024b). Terahertz planar cavity antenna based on effective medium for wireless communications, *IEEE Transactions on Terahertz Science and Technology*, **14**(2), pp. 248–257.

LI-M. S., FUMEAUX-C., AND WITHAYACHUMNANKUL-W. (2022a). 275-GHz planar high-gain resonant cavity antenna with effective medium, *2022 International Symposium on Antennas and Propagation (ISAP)*, pp. 121–122.

LI-M. S., FUMEAUX-C., AND WITHAYACHUMNANKUL-W. (2022b). Terahertz beam shaping: Gaussian to flat-top beam conversion through tri-layer metasurface, *2022 47th International Conference on Infrared, Millimeter, and Terahertz Waves (IRMMW-THz)*, pp. 1–2.

LI-M. S., MAI-T. V., FUMEAUX-C., SUZUKI-S., AND WITHAYACHUMNANKUL-W. (2023c). Terahertz resonant-tunneling diode with series-fed patch array antenna, *IEEE Transactions on Terahertz Science and Technology*, **13**(2), pp. 178–187.

LI-M. S., SUZUKI-S., FUMEAUX-C., AND WITHAYACHUMNANKUL-W. (2021). Improving the radiation performance of resonant-tunneling diode by using planar metallic arrays, *2021 46th International Conference on Infrared, Millimeter, and Terahertz Waves (IRMMW-THz)*, pp. 1–2.

LI-M. S., SUZUKI-S., FUMEAUX-C., AND WITHAYACHUMNANKUL-W. (2023d). Resonant-tunneling diode with spiral bias connections for circularly polarized radiation, *2023 48th International Conference on Infrared, Millimeter, and Terahertz Waves (IRMMW-THz)*, pp. 1–2.

LLOMBART-N., CHATTOPADHYAY-G., SKALARE-A., AND MEHDI-I. (2011). Novel terahertz antenna based on a silicon lens fed by a leaky wave enhanced waveguide, *IEEE Transactions on Antennas and Propagation*, **59**(6), pp. 2160–2168.

LUCYSZYN-S. (2007). Evaluating surface impedance models for terahertz frequencies at room temperature, *PIERS Online*, **3**(4), pp. 554–559.

LUK-K., ZHOU-S., LI-Y., WU-F., NG-K., CHAN-C., AND PANG-S. (2017). A microfabricated low-profile wideband antenna array for terahertz communications, *Scientific Reports*, **7**(1), art. no. 1268.

LU-P., HADDAD-T., SIEVERT-B., KHANI-B., MAKHLOUF-S., DÜLME-S., ESTÉVEZ-J. F., RENNINGS-A., ERNI-D., PFEIFFER-U., AND STÖHR-A. (2021). InP-based THz beam steering leaky-wave antenna, *IEEE Transactions on Terahertz Science and Technology*, **11**(2), pp. 218–230.

MAAS-A. L., HANNUN-A. Y., AND NG-A. Y. (2013). Rectifier nonlinearities improve neural network acoustic models, *ICML Workshop Deep Learning Audio Speech Language Processing*, **30**(1), art. no. 3.

MAI-T. V., ASADA-M., NAMBA-T., SUZUKI-Y., AND SUZUKI-S. (2023). Coherent power combination in a resonant-tunneling-diode arrayed oscillator with simplified structure, *IEEE Transactions on Terahertz Science and Technology*, **13**(4), pp. 405–414.

MAI-T. V., SUZUKI-Y., YU-X., SUZUKI-S., AND ASADA-M. (2020). Structure-simplified resonant-tunneling-diode terahertz oscillator without metal-insulator-metal capacitors, *Journal of Infrared, Millimeter, and Terahertz Waves*, **41**(12), pp. 1498–1507.

MAI-T. V., SUZUKI-Y., YU-X., SUZUKI-S., AND ASADA-M. (2022). Structure dependence of oscillation characteristics of structure-simplified resonant-tunneling-diode terahertz oscillator, *Applied Physics Express*, **15**(4), art. no. 042003.

MAKHLOUF-S., COJOCARI-O., HOFMANN-M., NAGATSUMA-T., PREU-S., WEIMANN-N., HÜBERS-H.-W., AND STÖHR-A. (2023). Terahertz sources and receivers: From the past to the future, *IEEE Journal of Microwaves*, **3**(3), pp. 894–912.

MAKHLOUF-S., DÜLME-S., GRZESLO-M., ESTÉVEZ-J. L. F., RYMANOV-V., LACKMANN-J., AND STÖHR-A. (2021). Monolithically integrated thz photodiodes with CPW-to-WR3 E-plane transitions for photodiodes packages with WR3-outputs, *Journal of Lightwave Technology*, **39**(24), pp. 7804–7812.

MATSUMOTO-H., WATANABE-I., KASAMATSU-A., AND MONNAI-Y. (2020). Integrated terahertz radar based on leaky-wave coherence tomography, *Nature Electronics*, **3**(2), pp. 122–129.

MEDRAR-K., MARNAT-L., DUSSOPT-L., BELEM-GONCALVES-C., DUCOURNAU-G., LUXEY-C., AND GIANESELLO-F. (2021). H-band substrate-integrated discrete-lens antenna for high data rate communication systems, *IEEE Transactions on Antennas and Propagation*, **69**(7), pp. 3677–3688.

MEI-X., YOSHIDA-W., LANGE-M., LEE-J., ZHOU-J., LIU-P.-H., LEONG-K., ZAMORA-A., PADILLA-J., SARKOZY-S., LAI-R., AND DEAL-W. R. (2015). First demonstration of amplification at 1 THz using 25-nm InP high electron mobility transistor process, *IEEE Electron Device Letters*, **36**(4), pp. 327–329.

MELENDRO-JIMENEZ-J., SANCHEZ-OLIVARES-P., TAMAYO-DOMINGUEZ-A., SUN-X., AND FERNANDEZ-GONZALEZ-J. M. (2023). 3D printed directive beam-steering antenna based on gradient index flat lens with an integrated polarizer for dual circular polarization at W-band, *IEEE Transactions on Antennas and Propagation*, **71**(1), pp. 1059–1064.

MENG-F., TANG-Z., HAZARIKA-J., SUZUKI-S., AND ROSKOS-H. G. (2023). Coherent emission from a linear array of RTDs, *2023 48th International Conference on Infrared, Millimeter, and Terahertz Waves (IRMMW-THz)*, pp. 1–2.

MITTLEMAN-D. M. (2018). Twenty years of terahertz imaging [Invited], *Optics Express*, **26**(8), pp. 9417–9431.

MONNAI-Y., LU-X., AND SENGUPTA-K. (2023). Terahertz beam steering: from fundamentals to applications, *Journal of Infrared, Millimeter, and Terahertz Waves*, **44**(3), pp. 169–211.

MORADIKOUCHI-A., SPARÉN-A., FOLESTAD-S., STAKE-J., AND RODILLA-H. (2022). Terahertz frequency domain sensing for fast porosity measurement of pharmaceutical tablets, *International Journal of Pharmaceutics*, **618**, art. no. 121579.

MRNKA-M., HENDRY-E., LÁČÍK-J., LENNON-R. A., BARR-L. E., HOOPER-I., AND PHILLIPS-D. B. (2022). Space squeezing optics: Performance limits and implementation at microwave frequencies, *APL Photonics*, **7**(7), art. no. 076105.

MURANO-K., WATANABE-I., KASAMATSU-A., SUZUKI-S., ASADA-M., WITHAYACHUMNANKUL-W., TANAKA-T., AND MONNAI-Y. (2017). Low-profile terahertz radar based on broadband leaky-wave beam steering, *IEEE Transactions on Terahertz Science and Technology*, **7**(1), pp. 60–69.

NAFTALY-M., AND MILES-R. E. (2007). Terahertz time-domain spectroscopy for material characterization, *Proceedings of the IEEE*, **95**(8), pp. 1658–1665.

NAGATSUMA-T., DUCOURNAU-G., AND RENAUD-C. C. (2016). Advances in terahertz communications accelerated by photonics, *Nature Photonics*, **10**(6), pp. 371–379.

NELLEN-S., ISHIBASHI-T., DENINGER-A., KOHLHAAS-R. B., LIEBERMEISTER-L., SCHELL-M., AND GLOBISCH-B. (2020). Experimental comparison of UTC- and PIN-photodiodes for continuous-wave terahertz generation, *Journal of Infrared, Millimeter, and Terahertz Waves*, **41**(4), pp. 343–354.

NGUYEN-TRONG-N., CHEN-S. J., AND FUMEAUX-C. (2022). High-gain dual-band dual-sense circularly polarized spiral series-fed patch antenna, *IEEE Open Journal of Antennas and Propagation*, **3**, pp. 343–352.

NGUYEN-T. T., AND KIM, DONG HO ABD JUNG-C. W. (2023). Conical horn antenna with high gain and circular polarization for sub-mm-wave/terahertz, *Journal of Infrared, Millimeter, and Terahertz Waves*, **44**(3), pp. 320–331.

NIAZ-M. W., YIN-Y., BHATTI-R. A., CAI-Y.-M., AND CHEN-J. (2021). Wideband Fabry–Perot resonator antenna employing multilayer partially reflective surface, *IEEE Transactions on Antennas and Propagation*, **69**(4), pp. 2404–2409.

NIELSEN-K., RASMUSSEN-H. K., ADAM-A. J. L., PLANKEN-P. C. M., BANG-O., AND JEPSEN-P. U. (2009). Bendable, low-loss Topas fibers for the terahertz frequency range, *Optics Express*, **17**(10), pp. 8592–8601.

NIST. (2021). James Clerk Maxwell Telescope: SCUBA-2 sensor array, `https://www.nist.gov/measuring-cosmos/james-clerk-maxwell-telescope`.

OKADA-K., KASAGI-K., OSHIMA-N., SUZUKI-S., AND ASADA-M. (2015). Resonant-tunneling-diode terahertz oscillator using patch antenna integrated on slot resonator for power radiation, *IEEE Transactions on Terahertz Science and Technology*, **5**(4), pp. 613–618.

ORIHASHI-N., HATTORI-S., SUZUKI-S., AND ASADA-M. (2005). Experimental and theoretical characteristics of sub-terahertz and terahertz oscillations of resonant tunneling diodes integrated with slot antennas, *Japanese Journal of Applied Physics*, **44**(11R), art. no. 7809.

OSHIRO-A., NISHIGAMI-N., YAMAMOTO-T., NISHIDA-Y., WEBBER-J., FUJITA-M., AND NAGATSUMA-T. (2022). PAM4 48-Gbit/s wireless communication using a resonant tunneling diode in the 300-GHz band, *IEICE Electronics Express*, **19**(2), art. no. 20210494.

PAASO-H., GULATI-N., PATRON-D., HAKKARAINEN-A., WERNER-J., DANDEKAR-K. R., VALKAMA-M., AND MÄMMELÄ-A. (2017). DoA estimation using compact CRLH leaky-wave antennas: Novel algorithms and measured performance, *IEEE Transactions on Antennas and Propagation*, **65**(9), pp. 4836–4849.

PICKWELL-E., AND WALLACE-V. P. (2006). Biomedical applications of terahertz technology, *Journal of Physics D: Applied Physics*, **39**(17), art. no. R301.

PISANO-G., AUSTERMANN-J., BEALL-J., HALVERSON-N., HUBMAYR-J., JAEHNIG-G., MCKENNEY-C. M., RAYMOND-B., AND SUZUKI-A. (2020). Development of flat silicon-based mesh lens arrays for millimeter and sub-millimeter wave astronomy, *Journal of Low Temperature Physics*, **199**(3), pp. 923–934.

PRICE-B. D., LOWRY-S. N., HARTLEY-I. D., AND REID-M. (2020). Subterahertz refractive flat-top beam shaping via 3D printed aspheric lens combination, *Applied Optics*, **59**(18), pp. 5429–5436.

PUERTA-R., YU-J., LI-X., XU-Y., OLMOS-J. J. V., AND MONROY-I. T. (2017). Demonstration of 352 Gbit/s photonically-enabled D-band wireless delivery in one 2×2 MIMO system, *2017 Optical Fiber Communications Conference and Exhibition (OFC)*, pp. 1–3.

PURSULA-P., LAMMINEN-A., MANNILA-R., TAPPURA-K., AND SAARILAHTI-J. (2019). Silicon gradient refractive index lens for millimeter wave radiometers, *2019 44th*

International Conference on Infrared, Millimeter, and Terahertz Waves (IRMMW-THz), pp. 1–3.

QUEMERAIS-T., GLORIA-D., GOLANSKI-D., AND BOUVOT-S. (2015). High-Q MOS varactors for millimeter-wave applications in CMOS 28-nm FDSOI, *IEEE Electron Device Letters*, **36**(2), pp. 87–89.

SAMOSKA-L. A. (2011). An overview of solid-state integrated circuit amplifiers in the submillimeter-wave and THz regime, *IEEE Transactions on Terahertz Science and Technology*, **1**(1), pp. 9–24.

SATO-K., AND MONNAI-Y. (2021). Two-dimensional terahertz beam steering based on trajectory deflection of leaky-mode, *IEEE Transactions on Terahertz Science and Technology*, **11**(6), pp. 676–683.

SEDDON-J. P., NATRELLA-M., LIN-X., GRAHAM-C., RENAUD-C. C., AND SEEDS-A. J. (2022). Photodiodes for terahertz applications, *IEEE Journal of Selected Topics in Quantum Electronics*, **28**(2: Optical Detectors), pp. 1–12.

SENGUPTA-K., AND HAJIMIRI-A. (2012). A 0.28 THz power-generation and beam-steering array in CMOS based on distributed active radiators, *IEEE Journal of Solid-State Circuits*, **47**(12), pp. 3013–3031.

SHANNON-C. E. (1948). A mathematical theory of communication, *The Bell System Technical Journal*, **27**(3), pp. 379–423.

SHARMA-A., AND SINGH-G. (2009). Rectangular microstirp patch antenna design at THz frequency for short distance wireless communication systems, *Journal of Infrared, Millimeter, and Terahertz Waves*, **30**(1), pp. 1–7.

SINGH-A. K., ABEGAONKAR-M. P., AND KOUL-S. K. (2019). Wide angle beam steerable high gain flat top beam antenna using graded index metasurface lens, *IEEE Transactions on Antennas and Propagation*, **67**(10), pp. 6334–6343.

SMITH-M. W. L., EALES-S. A., WILLIAMS-T. G., LEE-B., LI-Z., BARMBY-P., BUREAU-M., CHAPMAN-S., CHO-B. S., CHUNG-A., CHUNG-E. J., CHUNG-H.-H., CLARK-C. J. R., CLEMENTS-D. L., DAVIS-T. A., LOOZE-I. D., EDEN-D. J., ATHIKKAT-EKNATH-G., FORD-G. P., GAO-Y., GEAR-W., GOMEZ-H. L., DE GRIJS-R., HE-J., HO-L. C., HUGHES-T. M., JIAO-S., LI-Z., KEMPER-F., KIRCHSCHLAGER-F., KOCH-E. W.,

KONG-A. K. H., LEE-C.-H., LIN-E.-T., MAIRS-S., MICHAŁOWSKI-M. J., PATTLE-K., PENG-Y., RAGAN-S. E., RAWLINGS-M. G., RIGOPOULOU-D., SAINTONGE-A., SCHRUBA-A., TANG-X., WANG-J., WHITWORTH-A. P., WILSON-C. D., YIM-K., AND ZHU-M. (2021). The HASHTAG project: The first submillimeter images of the Andromeda galaxy from the ground, *The Astrophysical Journal Supplement Series*, **257**(2), art. no. 52.

SONG-H.-J., AND LEE-N. (2022). Terahertz communications: challenges in the next decade, *IEEE Transactions on Terahertz Science and Technology*, **12**(2), pp. 105–117.

SONG-L.-Z., ZHANG-T., QIN-P.-Y., DU-J., AND GUO-Y. J. (2024). Sub-THz broadband transmitting metasurfaces with enhanced frequency scanning capability, *IEEE Transactions on Terahertz Science and Technology*, **14**(1), pp. 82–90.

STEHR-F., STEIN-J., SCHUEDER-F., SCHWILLE-P., AND JUNGMANN-R. (2019). Flat-top TIRF illumination boosts DNA-PAINT imaging and quantification, *Nature Communications*, **10**(1), art. no. 1268.

SUBASHIEV-A. V., AND LURYI-S. (2006). Modal control in semiconductor optical waveguides with uniaxially patterned layers, *Journal of Lightwave Technology*, **24**(3), pp. 1513–1522.

SUZUKI-S. (2022). Resonant tunneling diode technology for future terahertz applications, *2022 International Electron Devices Meeting (IEDM)*, pp. 4.4.1–4.4.4.

TAJIMA-T., SONG-H.-J., AJITO-K., YAITA-M., AND KUKUTSU-N. (2014). 300-GHz step-profiled corrugated horn antennas integrated in LTCC, *IEEE Transactions on Antennas and Propagation*, **62**(11), pp. 5437–5444.

TAKAHASHI-H., KOSUGI-T., HIRATA-A., TAKEUCHI-J., MURATA-K., AND KUKUTSU-N. (2013). 120-GHz-band fully integrated wireless link using QSPK for realtime 10-Gbit/s transmission, *IEEE Transactions on Microwave Theory and Techniques*, **61**(12), pp. 4745–4753.

TANAKA-H., FUJIKATA-H., HAN-F., AND SUZUKI-S. (2023). Investigation of heat-dissipation structures in resonant tunneling diodes and their characteristics on terahertz oscillators, *Japanese Journal of Applied Physics*. Early access, doi: 0.35848/1347-4065/ad169a.

THIGALE-S., WANG-Q., MISHRA-D., GOLDYS-E. M., AND ATAKARAMIANS-S. (2023). Terahertz imaging: a diagnostic technology for prevention of grass seed infestation, *Optics Express*, **31**(22), pp. 37030–37039.

TOUSI-Y., AND AFSHARI-E. (2015). A high-power and scalable 2-D phased array for terahertz CMOS integrated systems, *IEEE Journal of Solid-State Circuits*, **50**(2), pp. 597–609.

URTEAGA-M., GRIFFITH-Z., SEO-M., HACKER-J., AND RODWELL-M. J. W. (2017). InP HBT technologies for THz integrated circuits, *Proceedings of the IEEE*, **105**(6), pp. 1051–1067.

VALUŠIS-G., LISAUSKAS-A., YUAN-H., KNAP-W., AND ROSKOS-H. G. (2021). Roadmap of terahertz imaging 2021, *Sensors*, **21**(12), art. no. 4092.

WEBBER-J., OSHIRO-A., IWAMATSU-S., NISHIDA-Y., FUJITA-M., AND NAGATSUMA-T. (2021). 48-Gbit/s 8K video-transmission using resonant tunnelling diodes in 300-GHz band, *Electronics Letters*, **57**(17), pp. 668–669.

WEN-B., AND BAN-D. (2021). High-temperature terahertz quantum cascade lasers, *Progress in Quantum Electronics*, **80**, art. no. 100363.

WI-S.-H., LEE-Y.-S., AND YOOK-J.-G. (2007). Wideband microstrip patch antenna with U-shaped parasitic elements, *IEEE Transactions on Antennas and Propagation*, **55**(4), pp. 1196–1199.

WITHAYACHUMNANKUL-W., YAMADA-R., FUJITA-M., AND NAGATSUMA-T. (2018). All-dielectric rod antenna array for terahertz communications, *APL Photonics*, **3**(5), art. no. 051707.

WU-F., AND LUK-K. M. (2017). Wideband high-gain open resonator antenna using a spherically modified, second-order cavity, *IEEE Transactions on Antennas and Propagation*, **65**(4), pp. 2112–2116.

WU-G.-B., ZENG-Y.-S., CHAN-K. F., QU-S.-W., AND CHAN-C. H. (2019a). 3-D printed circularly polarized modified fresnel lens operating at terahertz frequencies, *IEEE Transactions on Antennas and Propagation*, **67**(7), pp. 4429–4437.

WU-G. B., ZENG-Y.-S., CHAN-K. F., QU-S.-W., AND CHAN-C. H. (2019b). High-gain circularly polarized lens antenna for terahertz applications, *IEEE Antennas and Wireless Propagation Letters*, **18**(5), pp. 921–925.

WU-G.-B., ZENG-Y.-S., CHAN-K. F., QU-S.-W., SHAW-J., AND CHAN-C. H. (2022a). 3-D printed 3-D near-field focus-scanning lens for terahertz applications, *IEEE Transactions on Antennas and Propagation*, **70**(11), pp. 10007–10016.

WU-G.-B., ZHU-S.-Y., PANG-S. W., AND CHAN-C. H. (2022b). Superheterodyne-inspired waveguide-integrated metasurfaces for flexible free-space light manipulation, *Nanophotonics*, **11**(20), pp. 4499–4514.

XIANG-H., CHEN-B., YANG-M., YANG-T., AND LIU-D. (2019). A novel phase enhancement method for low-angle estimation based on supervised DNN learning, *IEEE Access*, **7**, pp. 82329–82336.

YANG-G., DONG-B., GU-B., ZHUANG-J., AND ERSOY-O. K. (1994). Gerchberg–Saxton and Yang–Gu algorithms for phase retrieval in a nonunitary transform system: a comparison, *Applied Optics*, **33**(2), pp. 209–218.

YANG-Q., GU-J., WANG-D., ZHANG-X., TIAN-Z., OUYANG-C., SINGH-R., HAN-J., AND ZHANG-W. (2014). Efficient flat metasurface lens for terahertz imaging, *Optics Express*, **22**(21), pp. 25931–25939.

YANG-X., ZHAO-X., YANG-K., LIU-Y., LIU-Y., FU-W., AND LUO-Y. (2016). Biomedical applications of terahertz spectroscopy and imaging, *Trends in Biotechnology*, **34**(10), pp. 810–824.

YEH-C., JO-G. D., KO-Y.-J., AND CHUNG-H. K. (2023). Perspectives on 6G wireless communications, *ICT Express*, **9**(1), pp. 82–91.

YE-X., XIANG-F., YOU-C., WANG-K., YANG-Z., LIU-J., AND WANG-S. (2018). Generation of a terahertz collimated top-hat beam by using two thin diffractive phase plates, *OSA Continuum*, **1**(4), pp. 1341–1348.

YI-H., QU-S.-W., NG-K.-B., CHAN-C. H., AND BAI-X. (2016). 3-D printed millimeter-wave and terahertz lenses with fixed and frequency scanned beam, *IEEE Transactions on Antennas and Propagation*, **64**(2), pp. 442–449.

YOU-X., AKO-R. T., LEE-W. S. L., BHASKARAN-M., SRIRAM-S., FUMEAUX-C., AND WITHAYACHUMNANKUL-W. (2020a). Broadband terahertz transmissive quarter-wave metasurface, *APL Photonics*, **5**(9), art. no. 096108.

YOU-X., AKO-R. T., LEE-W. S. L., BHASKARAN-M., SRIRAM-S., FUMEAUX-C., AND WITHAYACHUMNANKUL-W. (2021). Terahertz transmissive half-wave metasurface with enhanced bandwidth, *Optics Letters*, **46**(17), pp. 4164–4167.

YOU-X., FUMEAUX-C., AND WITHAYACHUMNANKUL-W. (2022). Tutorial on broadband transmissive metasurfaces for wavefront and polarization control of terahertz waves, *Journal of Applied Physics*, **131**(6), art. no. 061101.

YOU-X., UPADHYAY-A., CHENG-Y., BHASKARAN-M., SRIRAM-S., FUMEAUX-C., AND WITHAYACHUMNANKUL-W. (2020b). Ultra-wideband far-infrared absorber based on anisotropically etched doped silicon, *Optics Letters*, **45**(5), pp. 1196–1199.

YURDUSEVEN-O., ABBASI-M., AND FROMENTEZE-T. (2019). Frequency-diverse computational direction of arrival estimation technique, *Scientific Reports*, **9**(1), art. no. 16704.

YU-X., HEADLAND-D., NISHIDA-Y., KOALA-R. A. S. D., KIM-J., FUJITA-M., AND NAGATSUMA-T. (2022). Hybrid integration between resonant tunneling diodes and unclad microphotonic diplexer for dual-channel coherent terahertz receiver, *IEEE Journal of Selected Topics in Quantum Electronics*, **28**(3s), pp. 1–10.

YU-X., SUGETA-M., YAMAGAMI-Y., FUJITA-M., AND NAGATSUMA-T. (2019). Simultaneous low-loss and low-dispersion in a photonic-crystal waveguide for terahertz communications, *Applied Physics Express*, **12**(1), art. no. 012005.

YU-X., SUZUKI-Y., MAI-T. V., SUZUKI-S., AND ASADA-M. (2021). Highly efficient resonant tunneling diode terahertz oscillator with a split ring resonator, *IEEE Electron Device Letters*, **42**(7), pp. 982–985.

ZHAO-H., WANG-X., LIU-S., AND ZHANG-Y. (2023). Highly efficient vectorial field manipulation using a transmitted tri-layer metasurface in the terahertz band, *Opto-Electronic Advances*, **6**(1), art. no. 220012.

ZHU-J., YANG-Y., MCGLOIN-D., LIAO-S., AND XUE-Q. (2021). Sub-terahertz 3-D printed all-dielectric low-cost low-profile lens-integrated polarization beam splitter, *IEEE Transactions on Terahertz Science and Technology*, **11**(4), pp. 433–442.

ZHU-Q., NG-K.-B., AND CHAN-C. H. (2017). Printed circularly polarized spiral antenna array for millimeter-wave applications, *IEEE Transactions on Antennas and Propagation*, **65**(2), pp. 636–643.